

# University of Alberta

## Library Release Form

**Name of Author:** *Ross Grote Stirling*

**Title of Thesis:** *Development of a pedestrian navigation system using shoe mounted sensors*

**Degree:** *Master of Science*

**Year this Degree Granted:** *2004*

Permission is hereby granted to the University of Alberta Library to reproduce single copies of this thesis and to lend or sell such copies for private, scholarly or scientific research purposes only.

The author reserves all other publication and other rights in association with the copyright in the thesis, and except as herein before provided, neither the thesis nor any substantial portion thereof may be printed or otherwise reproduced in any material form whatever without the author's prior written permission.

---

*Signature*

7811 144 St  
Edmonton Alberta Canada T5R 0R1

University of Alberta

**Development of a  
Pedestrian Navigation System  
Using Shoe Mounted Sensors**

by

Ross Grote Stirling

A thesis submitted to the Faculty of Graduate Studies and Research  
in partial fulfillment of the requirements for the degree of  
Master of Science

Department of Mechanical Engineering

Edmonton, Alberta  
Spring 2004

## **Abstract**

Global navigation satellite systems are commonly used for personal positioning, providing high accuracy as long as a clear signal is available. In thick forest, urban areas with tall buildings, and indoor environments satellite positioning accuracy is degraded, and sensor based systems are a practical alternative. The purpose of this research is to explore and understand methods of applying shoe mounted sensors for pedestrian navigation. Using miniature, inexpensive sensors it is possible to create self-contained systems using sensor-only navigation techniques optimised for pedestrian motion. The systems developed extend existing foot based stride measurement technology by adding the capability to sense direction, making it possible to determine the path and displacement of the user. The proposed dead-reckoning navigation system applies an array of accelerometers and magneto-resistive sensors worn on the subject's shoe. Measurement of the foot's acceleration allows the precise identification of separate stride segments, thus providing improved stride length estimation. The system relies on identifying the stance phase to resolve the sensor attitude and determine the step heading. Proof of concept tests were performed in the laboratory using video motion capture equipment, and field trials were carried out in forested conditions. Performance metrics include accuracy of step detection, foot angle, foot velocity, stride length estimation and heading with respect to a high accuracy reference trajectory

## **Acknowledgements**

My work on this research project was made possible by the patience and generosity of some special people to whom I owe many thanks. I would like to express my gratitude to my co-supervisors Dr. Ken Fyfe of the Department of Mechanical Engineering at the University of Alberta and Dr. Gérard Lachapelle of the Department of Geomatics at the University of Calgary, who mentored and challenged me through this rewarding experience. I was fortunate to collaborate with and learn from fellow grad students Thomas Williams and Isaac Ikram, at the U of A, and Jussi Collin, Glenn MacGougan and Oleg Mezentsev at the U of C. Always, and especially lately, my parents, Ian and Stella, have supported and encouraged me and I am very grateful to them. Last, I would like to give a special thanks to a man whose dedication, perspective and creativity had a profound effect on me. Mick Saruwatari, I am grateful for your friendship and hope that you would be proud of the person you have helped me become.

# Contents

<b>1</b>	<b>Introduction and Review</b>	<b>1</b>
1.1	Pedestrian Navigation & Dead Reckoning . . . . .	2
1.2	Pedestrian Mechanization . . . . .	2
1.3	Biomechanics of Walking . . . . .	3
1.4	Development of Biomechanical Sensors . . . . .	4
1.4.1	Gait Event Determination . . . . .	5
1.4.2	Joint Angle Measurement . . . . .	6
1.4.3	Stride Length and Stride Velocity Modelling . . . . .	7
1.4.4	Stride Length Determination by Stride-wise Integration . . . . .	8
1.5	Pedestrian Navigation Systems . . . . .	9
1.6	Summary and Overview . . . . .	10
<b>2</b>	<b>Sensors And Equipment</b>	<b>12</b>
2.1	Accelerometers . . . . .	12
2.1.1	Mode of Operation: . . . . .	13
2.1.2	Application . . . . .	14
2.2	Anisotropic Magneto-resistive Sensors . . . . .	14
2.2.1	Mode of Operation: . . . . .	15
2.2.2	Application: . . . . .	15
2.3	Sensor Board . . . . .	15
2.4	Data Acquisition . . . . .	17
2.5	Positional Reference Equipment . . . . .	19
2.5.1	Laboratory Tests . . . . .	19
2.5.2	Field Tests . . . . .	20
2.6	Critique of Experimental Design. . . . .	21
<b>3</b>	<b>Gait Event Identification By Accelerometry</b>	<b>24</b>
3.1	Introduction . . . . .	24
3.2	Stride Events and Accelerometer Signals . . . . .	25
3.3	Useful Signal Manipulations . . . . .	27
3.3.1	Acceleration Energy . . . . .	27
3.3.2	Acceleration Product . . . . .	28

## CONTENTS

---

3.3.3	Acceleration Sum . . . . .	28
3.4	Detecting Events . . . . .	29
3.4.1	Magnitude Thresholds . . . . .	29
3.4.2	Variance Thresholds . . . . .	29
3.4.3	Local Extrema . . . . .	31
3.5	Gait Event Sequence and Gait Frequency Windowing . . . . .	32
3.6	Gait Event Detection . . . . .	33
3.7	Summary . . . . .	34
<b>4</b>	<b>Stride Length Measurement by Accelerometry</b>	<b>35</b>
4.1	General Plane Motion . . . . .	35
4.2	Accelerometry . . . . .	37
4.3	Orientation Angle . . . . .	39
4.3.1	Inclinometry . . . . .	39
4.3.2	Angular Acceleration and Angular Velocity Measurement . . . . .	39
4.4	Stride Length Calculation . . . . .	41
4.5	Practical Considerations of Numerical Integration . . . . .	44
4.5.1	Fourier Series Representation and Integration . . . . .	44
4.5.2	Frequency Response of Numerical Integration . . . . .	47
4.5.3	Integration Drift . . . . .	48
4.6	Summary . . . . .	50
<b>5</b>	<b>Heading Determination</b>	<b>51</b>
5.1	Navigation: Relating Reference Frames . . . . .	51
5.1.1	Subscripts and Notation . . . . .	52
5.1.2	Gravity . . . . .	53
5.1.3	Magnetic Field . . . . .	54
5.2	Algorithm . . . . .	54
5.2.1	Direction Cosine Matrix Construction . . . . .	54
5.2.2	Sensor Frame Heading . . . . .	58
5.2.3	Declination and Misalignment Correction . . . . .	58
5.3	Magneto Resistive Sensor Calibration . . . . .	59
5.4	Ideal Sensor Output . . . . .	59
5.4.1	Example . . . . .	61
5.5	Spin Calibration . . . . .	62
5.6	Circle Walk Calibration . . . . .	64
5.7	Summary . . . . .	66
<b>6</b>	<b>Treadmill Testing</b>	<b>67</b>
6.1	Experimental Design . . . . .	67
6.2	Video Data . . . . .	68
6.2.1	Foot Position . . . . .	68

## CONTENTS

---

6.2.2	Foot Pod Angle . . . . .	69
6.3	Accelerometer Data . . . . .	71
6.4	Gait Event Detection . . . . .	71
6.5	Static Foot Angle Measurement . . . . .	74
6.6	Dynamic Foot Angle Measurement . . . . .	75
6.7	Foot Velocity Profiles . . . . .	78
6.7.1	Horizontal Velocity . . . . .	78
6.7.2	Vertical Velocity . . . . .	80
6.8	Distance Measurements . . . . .	82
6.9	Summary of Treadmill Testing . . . . .	83
<b>7</b>	<b>Field Testing</b>	<b>85</b>
7.1	Experimental Design . . . . .	85
7.2	Long Course Trajectories . . . . .	87
7.2.1	High Sensitivity GPS . . . . .	88
7.2.2	Ring Laser Gyro . . . . .	88
7.2.3	Foot Pod . . . . .	89
7.2.4	Position Error . . . . .	90
7.2.5	Stride Length Error . . . . .	91
7.2.6	Heading Error . . . . .	92
7.2.7	Calibration Error . . . . .	93
7.3	Performance with bias adjustments . . . . .	94
7.3.1	Long Course Performance . . . . .	94
7.3.2	Position Error . . . . .	95
7.3.3	Stride Length Error . . . . .	95
7.3.4	Heading Error . . . . .	96
7.4	Short Term Performance . . . . .	97
7.4.1	Moving Turn . . . . .	97
7.4.2	Stationary Turn . . . . .	98
7.5	Summary of Field Trials . . . . .	99
<b>8</b>	<b>Conclusion and Recommendations</b>	<b>100</b>
8.1	Improving performance . . . . .	101
8.2	Recommendations for Further Investigation . . . . .	101
<b>A</b>	<b>Sensitivity Analysis</b>	<b>107</b>
A.1	Accelerometer Sensitivity and Noise Density . . . . .	107
A.2	Sensor and Algorithm Resolutions . . . . .	108
A.2.1	Angular Acceleration Resolution . . . . .	109
A.2.2	Integrated Angular Velocity and Angular Resolution . . . . .	110
A.2.3	Integrated Linear Velocity and Position Resolution . . . . .	112

## CONTENTS

---

<b>B Accelerometer Calibration</b>	<b>114</b>
B.1 Block Calibration . . . . .	114
B.1.1 Error sources . . . . .	115
<b>C Geomagnetic Fields</b>	<b>117</b>
C.1 Introduction . . . . .	117
C.2 Magnetic Field Parameters . . . . .	117
C.3 Magnetic Field References . . . . .	118

# List of Figures

1.1	Typical Normal Walking Cycle. Adapted from [3]	4
2.1	ADXL Series accelerometer on prototype board	13
2.2	Simplified accelerometer mode of operation	13
2.3	Sensor boards mounted orthogonally	16
2.4	Prototype sensor array attached to shoe	17
2.5	Complete Data Acquisition System	18
2.6	Infrared tracking cameras	20
3.1	Typical Normal Walking Cycle. Adapted from [3]	25
3.2	Acceleration Signals and Events	26
3.3	Stride detection signals derived from acceleration	27
3.4	Detecting Gait Events With Variance	30
3.5	Detection of local maxima and minima in a signal	32
4.1	Rigid body with parallel offset planar accelerometers	36
4.2	Components of General Plane Motion	36
4.3	Equivalent Acceleration	37
4.4	Components of horizontal and vertical acceleration	38
4.5	Resolving acceleration into vertical and horizontal components using foot angle.	43
4.6	Angular acceleration and frequency spectrum	45
4.7	Frequency response of single and double integration	47
4.8	Comparison of analytical and numerical integrations:	49
4.9	Single stride angle profile	50
5.1	Relationship of global, user and sensor reference frames	52
5.2	Gravitational and magnetic field vectors in the global frame	55
5.3	Gravitational and magnetic field vectors in the sensor frame	55
5.4	Magnetic East $\vec{e}$ is perpendicular to both gravity $\vec{g}$ , and magnetic field $\vec{h}$ .	56
5.5	Magnetic North, $\vec{n}$ is perpendicular to $\vec{g}$ and $\vec{e}$	57
5.6	Ideal AMR output for $2\pi$ rotation about $\vec{g}$	61

## LIST OF FIGURES

---

5.7	AMR sensor signals for stationary spin . . . . .	62
5.8	Spin calibration: Sensor output matched to ideal signal . . . . .	63
5.9	Spin calibration: Horizontal alignment corrected . . . . .	63
5.10	Raw AMR output for circle walk calibration . . . . .	64
5.11	Stance phase component of AMR signal during circle walk . . . . .	65
5.12	Calibrated magneto-resistive sensor signals for circle walk . . . . .	65
6.1	Reflective markers on shoe and footpod . . . . .	68
6.2	Ankle trajectory at 1.3 m/s . . . . .	69
6.3	Foot pod angle profile at 1.3 m/s treadmill speed . . . . .	70
6.4	Ankle marker trajectory with foot pod angle . . . . .	70
6.5	Acceleration measured . . . . .	71
6.6	Gait Event Signals . . . . .	72
6.7	Detected gait events plotted on foot pod angle profile. . . . .	73
6.8	Spatial location of Gait Events . . . . .	73
6.9	Stance phase foot angle profile for three consecutive strides . . . . .	74
6.10	Error of static foot angle calculation . . . . .	75
6.11	Calculated foot angle of three consecutive strides at 1.1 m/s . . . . .	76
6.12	Averaged foot pod angle profiles . . . . .	77
6.13	Error in dynamic foot angle profile . . . . .	77
6.14	Horizontal foot velocity profiles of 3 consecutive strides - 1.1 m/s . . . . .	78
6.15	Average horizontal velocity at various treadmill speeds . . . . .	79
6.16	Error in horizontal velocity . . . . .	79
6.17	Vertical velocity profiles . . . . .	80
6.18	Average vertical velocity profiles for various treadmill speeds. . . . .	81
6.19	Error in vertical velocity . . . . .	81
6.20	Stride velocity and distance measurement comparison . . . . .	83
7.1	Field trial equipment: (left) Foot pod on left foot (right) refence equipment . . . . .	86
7.2	Field test course . . . . .	87
7.3	Trajectory measured by high sensitivity GPS . . . . .	88
7.4	Trajectory using torso mounted ring laser gyros and constant steplength . . . . .	89
7.5	Trajectory using shoe mounted sensors . . . . .	90
7.6	Comparison of error in position . . . . .	91
7.7	Comparison of distance measurements . . . . .	92
7.8	Comparison of ring laser gyro and foot pod heading . . . . .	93
7.9	Foot pod trajectory after bias level adjustment . . . . .	95
7.10	Error in position, after bias level adjustment . . . . .	95
7.11	Comparison of distance measurements after bias adjustment . . . . .	96
7.12	Comparison of ring laser gyro and foot pod heading after bias adjustment . . . . .	96
7.13	Short term performance of the foot pod . . . . .	97
7.14	Comparison of GPS and foot pod trajectories during short radius turn . . . . .	98

## LIST OF FIGURES

---

7.15	Comparison of GPS and foot pod trajectories during stationary period . . .	99
A.1	Quantization of accelerometer signal . . . . .	109
A.2	Error in static angle due to quantization . . . . .	110
A.3	Error in Horizontal Acceleration . . . . .	112
B.1	Block Calibration Positions . . . . .	114
B.2	Accelerometer Misalignment . . . . .	115
C.1	Magnetic field elements, adapted from [35] . . . . .	118
C.2	World map of Earth's main field - declination, adapted from [35] . . . . .	119
C.3	Magnetic field observations at Victoria, B.C. February 14, 2003 [36] . . .	120

# List of Tables

2.1	Specifications for ADXL310 Accelerometers with 5V Supply . . . . .	14
2.2	Specifications for HMC1022 with 5 V supply . . . . .	15
2.3	Specifications for sensor boards . . . . .	17
2.4	Specifications for NI DAQ 6024E - As Applied . . . . .	19
3.1	Gait Event Detection Sequence . . . . .	33
6.1	Point J Foot Angle Error (m/s ) . . . . .	75
6.2	Mean Horizontal Velocities (m/s ) . . . . .	80
6.3	Vertical Velocity Comparison . . . . .	82
6.4	Stride Length Comparison . . . . .	82
6.5	Stride Length Comparison . . . . .	83

# Chapter 1

## Introduction and Review

*Dead Reckoning - the seaman's calculation of courses and distance -  
had become the merry art of guesswork*

- Frank Worsley Captain, *HMS Endurance*

In December 1914, Ernest Shackleton led an expedition to attempt the first crossing of the Antarctic continent from sea to sea. Exceptionally heavy ice crushed their ship *Endurance*, leaving the men adrift on the pack ice without hope of rescue. They managed to sail three open lifeboats to Elephant Island, where Shackleton decided that six men would attempt the 700 nautical mile voyage back to South Georgia Island to get help. Considered one of the greatest feats of marine navigation, their fourteen day epic journey succeeded through the efforts of the ship's captain, Frank Worsely. Guiding the tiny *James Caird* using his best estimations of course and speed, and only occasional sun positions calculated by hand on sodden paper, Worsely's uncanny dead reckoning saved the lives of twenty-eight men.

Worsely understood his instruments and their shortcomings, so he could minimize his measurement error. Of equal importance though, he had a deep understanding of the vessel's behavior, so he could predict its motion. While seemingly far removed from Antarctic adventures, the same principles apply to sensor based pedestrian navigation.

In this thesis we will show how an understanding of miniature sensors and knowledge of human motion make it possible to calculate a person's position by dead reckoning. We begin by describing pedestrian navigation and the stride based pedestrian mechanization model. Reference frames and their relation to the navigation problem are then introduced. The foot based sensor method draws on research from both the biomechanics and

navigation communities, and relevant literature from both is reviewed.

## 1.1 Pedestrian Navigation & Dead Reckoning

Pedestrian navigation is the process of determining and maintaining positional information for a person travelling on foot. In situations of relative familiarity, it may consist simply of verbal instructions or directions on a map. Usually though, the term pedestrian navigation refers to the use of technological aids for positioning, such as satellite based global positioning systems (GPS) or sensors mounted on the body. In the outdoors, where there is a clear line of sight to the satellites, global navigation satellite systems provide location with accuracies ranging from tens of meters to tens of centimetres depending on the details of the receiver and methodology. The orientation of the receiver need not be known, and error in location does not increase in time, making satellite positioning the preferred method wherever it is practical. Recently developed high sensitivity receivers have made it possible to use GPS in dense forests and even wooden structure buildings ([1],[2]) though positioning in concrete buildings has not yet been possible.

In environments that are challenging for satellite positioning, standard inertial navigation systems (INS) used in aerospace and marine navigation calculate position by temporal integration of accelerometer and gyroscope data. Estimated positions are calculated at regular time intervals and the error growth is proportional to time cubed. Accuracy requirements in these applications justify the size and cost of high quality inertial sensors. Because the dynamics generated by a walking person are small with respect to the accuracy of these low cost sensors, temporal integration of sensor output will lead to rapidly propagating error, making traditional INS impractical. Instead an alternate navigation method is sought that better suits the manner in which people walk.

## 1.2 Pedestrian Mechanization

Recognizing that people move one step at a time, the *pedestrian mechanization* restricts error growth by propagating position estimates in a stride-wise fashion, rather than on a fixed time interval. Self contained inertial sensors in a Pedestrian Dead Reckoning (PDR) system are used to detect the occurrence of steps, and provide a means of estimating the distance and direction in which the step was taken. In this way error is proportional to the number of steps taken. The three important parameters of pedestrian dead reckoning are *step detection*, *stride length estimation*, and *heading determination*.

For a stride length  $d_i$  at a heading of  $\theta_i$  measured counterclockwise from North, the Eastward displacement  $\Delta x_i$  is

$$\Delta x_i = d_i \cos \theta_i$$

Similarly, the Northward displacement is

$$\Delta y_i = d_i \sin \theta_i$$

So for  $n$  recorded strides, the position with respect to a known reference  $[x_0, y_0]$  is

$$\begin{aligned} x_n &= x_0 + \sum_{i=1}^{i=n} d_i \cos \theta_i \\ y_n &= y_0 + \sum_{i=1}^{i=n} d_i \sin \theta_i \end{aligned}$$

These equations form the basis of pedestrian navigation by dead reckoning. In this method error in position is propagated linearly as a function of the number of strides taken, meaning that the error is proportional to the distance travelled and independent of time.

Having determined a method for calculating position, the challenge is now to find means of detecting stride events, estimating stride lengths ( $d$ ), and estimating stride direction ( $\theta$ ). In addition to these basic objectives, techniques must also be found to determine sensor orientation and minimize the errors inherent in the calculation processes. A variety of techniques for making these estimations and mitigating error have emerged from convergent research in pedestrian navigation and biomechanics and are discussed in the following sections. We begin by describing the biomechanics of walking, then discuss gait event detection and biomechanics sensors before reviewing pedestrian navigation research in more detail.

### 1.3 Biomechanics of Walking

Analysis of the human gait [3] shows that the basic pattern of human motion during a walk is cyclical, repeatable and remarkably consistent between individuals. Illustrated in Figure 1.1, the gait cycle consists of two main phases: The *stance* phase and the *swing* phase. The foot is in contact with the ground for the entire stance phase until *toe-off* occurs. Toe-off initiates the swing phase when the foot is lifted off the ground and carried

forward to begin the next stride. The swing phase ends when the foot is again placed on the ground, beginning the next stance phase, and completing the gait cycle. The opposite limb repeats the same sequence of events, but is 180° out of phase. The majority of the motion of the foot is in the *sagittal* plane, which is a vertical plane sectioning the body into right and left sides.

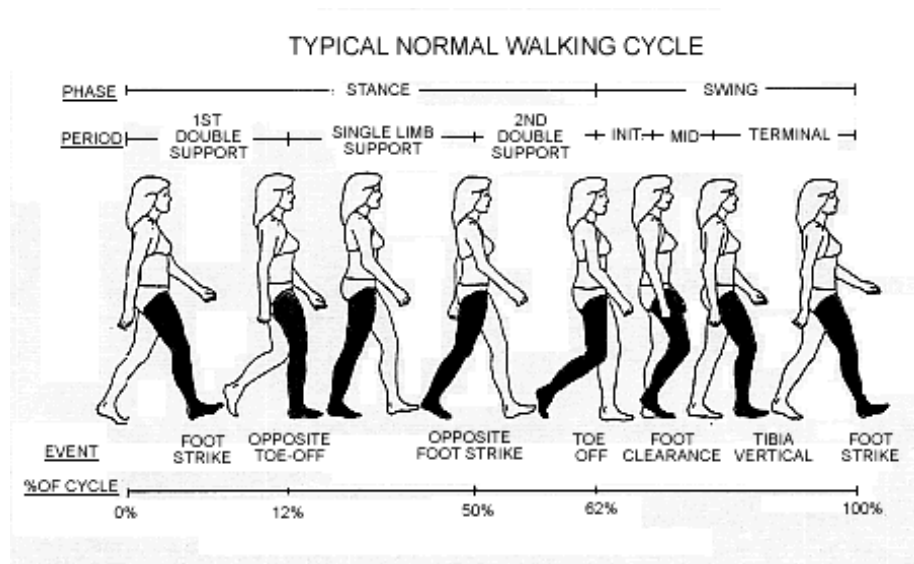


Figure 1.1: Typical Normal Walking Cycle. Adapted from [3]

At normal walking speeds, the centre of gravity of the body maintains an approximately constant horizontal velocity, with a smooth vertical oscillation of just a few centimetres. In contrast, the horizontal velocity of the foot varies each stride from stationary to over twice the velocity of the torso. This leads to a cyclical pattern of acceleration, and also foot impacts that can be measured a number of ways.

From a sensor perspective, the stance phase is of particular interest since it provides a brief period every step where the foot is stationary. This moment of zero velocity can be used advantageously to determine sensor orientations and reset measurements.

## 1.4 Development of Biomechanical Sensors

To further these understanding of human locomotion, biomechanics researchers require a means to measure properties of the human gait. High accuracy systems using cameras

and force plates are available in laboratory environments but there is a recognized need for biomechanics sensors capable of measuring human motion in an unrestricted, natural environment. This has led to substantial research effort in the area of biomechanical sensors and the application of miniature sensors, mainly accelerometers and gyroscopes. The advantage these sensor systems have over electrogoniometry or kinephotography in terms of their portability, is tempered by the added challenges which must be overcome to get useful information from them ([4],[5],[6]).

One challenge is simply determining the sensor orientation so that the correct components can be resolved from the signal. Another is overcoming the rapid error growth that accompanies the integration of gyroscope and accelerometers signals. As reviewed in the following sections, successful sensor applications for biomechanics research have employed techniques that minimize or circumvent these obstacles.

#### 1.4.1 Gait Event Determination

Before stride displacements and heading angles can be measured, the stride event itself must be determined. If particular phases of the gait cycle are to be used, they must be identified. Gait event detection is important in both biomechanics and pedestrian navigation research fields and the techniques developed range in complexity and performance.

A direct method of identifying foot strike and toe-off is to use a foot switch or pressure sensor attached on the sole of the user's foot. These devices are simple to apply, have rapid response times and gait events are clearly defined. While they provide satisfactory results for normal walking, Aminian [4] notes that problems with unusual gait, mechanical failure and uneven walking surfaces limit their applicability. Hansen [6] points out that these devices add another signal which must be recorded and synchronized with other measurements. It is more practical and efficient to detect gait events with the same sensors that are used for stride length or heading measurements.

In pedestrian navigation and biomechanics systems that apply accelerometers, it is common practice to detect foot strike from peaks in the acceleration measured ([7], [8] for example). If the only gait event of interest is foot strike, this method will work reliably, provided that the threshold detections are set appropriately for the walking conditions. Also, depending on sensor placement, accelerometers will measure the foot strikes from both feet.

Veltink et al [9] applied two uniaxial seismic accelerometers to detect periods of knee instability during walking. Peak differences in acceleration measured by two sensors

tangentially placed on the upper leg, were used to identify gait events such as knee-lock. This method was found to detect gait events earlier than is possible using a goniometer.

Using wavelet analysis, Aminian et al [4] found that toe-off and foot strike could be reliably detected from a shank mounted gyroscope signal, reporting a minimal systematic delay (10ms) with respect to a foot switch. While reliable, this detection method adds computational complexity relative to other methods.

Even in a laboratory environment, where sophisticated equipment such as force plates and kinephotographic systems are available, it is challenging to create stride event determination schemes robust enough to handle widely varying conditions. Hansen [6] presents a method for detecting heel strike and toe-off by the relative positioning of force plate centres of pressure with respect to an ankle marker. While only practical in a laboratory environment, Hansen's technique importantly avoids the use of thresholds for detection, removing the need for user specific tuning of parameters. Also of interest, Hansen found that the forward movement of the center of pressure slows dramatically when going from double limb support into single limb stance, indicating that some parts of the stance phase may be better than others for sensor orientation determination.

#### 1.4.2 Joint Angle Measurement

One of the first uses of accelerometers for biomechanics study was described by Morris [10] in 1973. This system measured the motion of the lower leg using six accelerometers. By recognizing that during the stance phase the shank rotates around a point within the talus of the foot, the angular position of the sensor frame with respect to the Earth frame could be determined, making it possible to remove gravitational acceleration from the signal. Morris argued that accelerations in the transverse plane are relatively small so the motion may be reasonably assumed to be entirely sagittal. Stride detection was done visually in postprocessing and, to reduce integration drift over a stride, the data was filtered to make the values equal at the beginning and end of each stride.

Willemson et al [11] presented a method for directly measuring the relative angle between the calf and thigh by accelerometry but without integration. Assuming strictly sagittal plane motion, pairs of biaxial accelerometers were placed above and below the knee joint. This technique worked well at very low frequencies but required substantial filtering to work while walking. Examining the sources of error in joint angle accelerometry, Willemsen [12] found that the accelerometers contributed less to the overall than the planar motion assumptions made to simplify calculations. Applying a gyroscope, and

using a static period to determine accelerometer orientation, Veltink et al [5] had less error while still avoiding integration. In both cases, the signals were heavily filtered to remove noise. Mayagoitia et al [13], further developed this technique, presenting a portable system capable of measuring the angular position, velocity and acceleration of the shank, knee and thigh with an error of about 7%.

Working with a triad of accelerometers and a triad of gyroscopes, Baten et al [14] found that the amount of integration drift observed was dependent on the type of movement being measured. During completely stationary periods they found the error to drift at one degree per minute, but when the foot was moved in a more complicated motion they observed an integration drift of six degrees per minute. They proposed a correction scheme where relatively stationary periods are used to correct sensor orientation and estimate drift. For tests of 30s duration, this reduced the error by a factor of four.

### 1.4.3 Stride Length and Stride Velocity Modelling

To avoid drift due to integration, numerous methods have been proposed that use empirical models to estimate stride length. Many of these methods are based on pendular models of locomotion.

Miyazaki [15] proposed an ambulatory monitoring system using a piezoelectric gyroscope strapped just above the knee. Angular displacement of the thigh was calculated each stride by integration of the angular velocity data, and the stride duration was determined. Assuming a symmetric gait, and modelling the leg as a single segment, the approximate stride length was estimated using simple trigonometry and the measured length of the user's leg. Calibration over a known distance was performed to determine the coefficients of linear regression to compensate the estimated stride length for changing values of stride duration. With multiple test subjects on a 40m level test surface, the maximum relative error was  $\pm 15\%$ . Proposing a double segment gait model involving both shank and thigh, Aminian et al [4] reported a reduced error of  $\pm 7\%$ , due mainly to gyroscope error. In this study gyroscopes were mounted on the shank.

Both of these systems are lightweight and portable, so can be applied outside the lab in unrestricted conditions, however neither has a means of detecting changes in walking conditions that would invalidate the model. As well, both systems require that the leg length be measured and a user specific calibration procedure be followed.

#### 1.4.4 Stride Length Determination by Stride-wise Integration

Stride length estimation by empirical modelling is effective when the user moves in anticipated conditions, but lacks the generality of application that accompanies a direct measurement method.

Direct stride length measurement by integration is possible with sensors mounted on the user's foot. During walking, the motion of the foot generates high accelerations in a repeatable pattern, and the relatively stationary period during the support phase of the stride allows the determination or assumption of initial conditions for stride-wise temporal integration of acceleration signals. The angle of the foot continually changes through the gait cycle, and must be defined so that the horizontal component of acceleration in the sagittal plane can be resolved.

The motion analysis system patented by Fyfe [16] in 1999 applies a biaxial sagittal plane accelerometer to measure foot acceleration. A third parallel offset accelerometer is used to allow measurement of angular acceleration which is integrated twice to yield the foot angle profile for the stride. The foot angle profile is then used to resolve the horizontal acceleration from the biaxial accelerometer measurements, and this horizontal acceleration is integrated twice to yield stride length. Drift is reduced by making use of the zero velocity reference during stance phase and removing the signal mean prior to integration. Accurate to within 3% over a wide population and without user calibration, this technique is valid for a complete range of gait velocities from slow walk to full run and has been applied in running related consumer products such as the Nike SDM.

Sagawa [17] demonstrated a similar system in 2000 that applies a triad of accelerometers and a sagittal plane gyro. While the gyro requires only a single integration to measure the foot angle profile, this technique is otherwise functionally identical to Fyfe. Over multiple 30 m trials, this method had a maximum error of 5%.

As with some of the stride modelling techniques, the work by Sagawa and Fyfe relies on the assumption that the foot motion is primarily in the sagittal plane. However, these methods have a possible advantage in that they measure step length directly and work without making further assumptions about the user's height, gait, or walking environment. From a practical perspective, Fyfe's entirely accelerometer based method may be preferred to Sagawa's as accelerometers are currently less expensive, smaller, draw less power and drift less than gyros.

## 1.5 Pedestrian Navigation Systems

Development of portable pedestrian navigation systems has been made possible by the relatively recent emergence of compact, inexpensive sensors. As in biomechanics research, miniature accelerometers and rate gyroscopes are commonly applied, but two other types of miniature sensors - magnetometers and barometers - improve direction sensing and allow the measurement of vertical displacement. The low dynamics and the relatively constant orientation of the torso with respect to the user's direction of travel make it the location of choice for sensor placement. Though all systems reported are capable of operating in a dead reckoning mode, most integrate GPS to some degree. The systems discussed here are united in applying the pedestrian mechanization, propagating a position solution based on detecting strides, and estimating their length and heading. The differing combinations of sensors, methods of calibration and step modelling, and relative complexity result in varying levels of success and accuracy.

Without a means to directly measure step length, torso based methods use accelerometers to detect the stride event and then a mathematical model is applied estimate the stride length. Levi and Judd [18] patented a system using a Fourier transform of accelerometers data to determine the fundamental gait frequency and adjust the base stride length.

Ladetto et al ([19], [20]) modelled step length as a function of step period, acceleration magnitude, and acceleration variance, using GPS to calibrate the model parameters. A basic assumption is made that step lengths are not constant but exhibit a continuous variation around a more stable value. Over a broad based study, this method had error of approximately 2% of the distance travelled. Ladetto [8] also addressed modelling human motion in multiple directions. Referring to established patterns, it is possible to use triaxial accelerometers to detect when the user is walking sideways or backwards. This insight adds a capability to pedestrian dead reckoning not found in most other research.

While the accuracy of the various methods of step length measurement have brought the accuracy to useful levels, maintaining long term heading accuracy remains challenging. Earth's magnetic field is relatively weak and nearby metal or electrical fields will distort the output from compassing sensors. Gyros on the other hand, have output that will drift in time. Ladetto [21] developed a system that relies mainly on digital compassing, but uses gyroscopes to compensate the heading calculation during rapid turns and when the magnetic field is detectably disturbed. In the same paper, Ladetto describes a user calibration process that establishes the system parameters while the user is walking along

known headings.

Using a small torso mounted inertial system integrated with a GPS, Käppi et al ([7],[22]) were able to maintain sufficient positional accuracy to save power by reducing the required frequency of GPS position updates. Again strides were detected from the magnitude of the acceleration measured at the torso, but instead of using stride frequency, step length was estimated by integrating the magnitude of the measured acceleration over the stride. The magnitude of the acceleration was also used to infer the user's motion state allowing the estimate to be modified for various walking conditions. Gyroscopes were the main sensor used for heading, but a magnetic compass (tilt compensated by accelerometers) was used to remove inherent time dependent drift. Importantly, this system included an atmospheric barometer so that vertical travel could be resolved.

Recognizing that determining accurate heading with low costs sensors remains an obstacle for indoor positioning, Collin et al [23] tested the performance of pedestrian dead reckoning system applying high accuracy ring laser gyros for heading. Ring laser gyros have drift of less than 1 degree per hour, and are insensitive to the substantial magnetic field disturbances common indoors. Initializing the system outside and assuming a fixed step length determined by GPS, the error in position calculated by this system over a 40 min test was just 5 m. Though high accuracy heading systems are prohibitively expensive for consumer applications, this method demonstrates that effective indoor positioning is possible.

## 1.6 Summary and Overview

Most of the biomechanics papers reviewed here proposed a sensor based method of measuring some aspect of the leg's motion during walking. These papers began by describing the advantage general sensor based motion analysis would bring to research because measurement would be possible outside of the confines of a laboratory. As very few of these papers report results of general motion recorded outside of the laboratory, this challenge remains largely unanswered. However, they do demonstrate that by making appropriate assumptions, relative joint angles, stride velocities and gait lengths can be measured or estimated with reasonable accuracy.

Generally, pedestrian navigation research has focused on torso mounted sensors since the low dynamics are suitable for heading measurement. Though stride length is not measured directly, reasonable accuracy is achieved through empirical modelling and GPS integration.

In this thesis, a pedestrian dead reckoning system is proposed that applies sensors mounted on the shoe. The technique of stride length measurement using shoe mounted accelerometers invented by Fyfe will be applied and analyzed. This leaves the problem of heading determination, which is attempted with magneto-resistive sensors. Gait event detection will be used to find a stationary point in the stance phase where the orientation of the shoe mounted sensors can be calculated. As this approach is novel, the research objective is to establish the basic feasibility of a shoe mounted sensor system for pedestrian navigation. The scope of the research is narrowed to a tractable and practical level. The following are some of the considerations and limitations we have established for ourselves and an overview of how they are treated in this thesis.

First, keeping in mind that this research is focused toward practical applications, we limit ourselves to working with readily available, low cost, compact sensors. This will limit the accuracy of the system, but will show the minimum level of performance that can be expected. The sensors, data acquisition and reference equipment used is described in Chapter 2.

Unrestricted human movement is complex and varied. To reduce the amount of analysis and special case consideration, the pedestrian motion in this study is limited to horizontal forward walking. Assuming regular walking simplifies the process of gait event identification by accelerometry which is described in Chapter 3. Again assuming normal forward walking, we describe how the stride length can be measured with accelerometers in Chapter 4. Chapter 5 discusses the use of anisotropic magneto-resistive sensors for heading calculation, and describes the necessary field calibration.

Since research discussed in this review has shown that integration of GPS and PDR will inevitably improve the quality of positioning, we evaluate the performance of the system in strictly dead reckoning mode to establish minimum accuracy. Chapter 6 describes the treadmill tests used to evaluate the gait identification and stride length measurement. The results of field tests are presented in Chapter 7, where the position calculated using shoe mounted sensors is compared to GPS and high accuracy heading sensors. Finally in Chapter 8, we present conclusions and discuss topics that merit further investigation.

## Chapter 2

# Sensors And Equipment

*The quality of an experiment's design is inversely proportional to the length of electrical tape required for its execution - Ross Stirling*

In this chapter the specifications, mode of operation, and application details are described for the sensors, and data acquisition system used in this shoe mounted pedestrian navigation investigation. Positional reference equipment such as the GPS receivers and infrared cameras used in the laboratory tests and field trials are also described. Finally, since the evaluation of this method of pedestrian navigation depends on the quality of the data recorded, the experimental design is reviewed and critiqued.

### 2.1 Accelerometers

Analog Devices' ADXL series of MEMs accelerometers were chosen for acceleration measurement because of their compact size, robust design and interchangeability. Shown on a prototype breadboard in Figure 2.1, they use relatively little power, and require just a few passive components to operate.

These sensors are available with  $2g$  or  $10g$  input ranges but have identical circuitry so a variety of acceleration conditions can be measured by changing just one component. In low acceleration applications,  $2g$  ADXL202's can be used to maximize the sensitivity. The extended  $10g$  input range of the ADXL210's was desirable for shoe mounted applications.

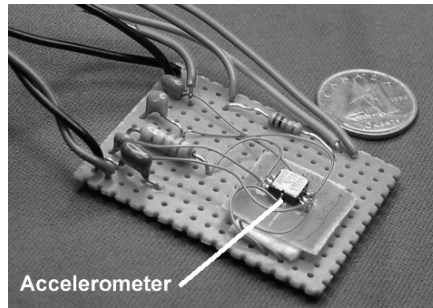


Figure 2.1: ADXL Series accelerometer on prototype board

### 2.1.1 Mode of Operation:

The ADXL accelerometers are biaxial acceleration sensors micromachined on a single integrated circuit. Table 2.1 lists the manufacturer's nominal specifications [24] of the ADXL210 accelerometers used. Figure 2.2 shows a simplified schematic of the mode of operation. A moving mass, (labelled **A** in the figure) is suspended from a fixed support (**B**) by polysilicon springs that provide a resistance to accelerative forces. Plates on the fixed support and moving mass are interleaved, creating a capacitor sensitive to relative motion between **A** and **B**. As shown in the middle illustration of the figure, acceleration of the sensors in one direction will cause deflection of the polysilicon springs in the opposite direction due to the inertia of the moving mass **A**. This deflection changes the capacitance between the plates in proportion to the acceleration. A closed loop control applies voltage across this differential capacitor to counteract the movement, holding the moving mass in place and maintain the linearity of the sensor over a wider range of accelerations.

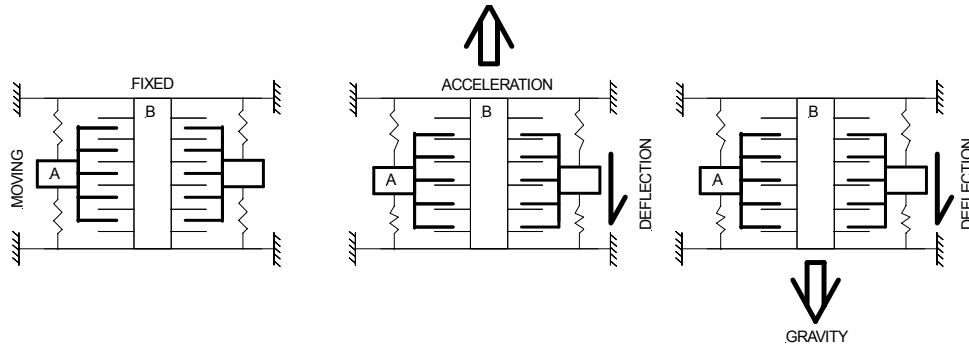


Figure 2.2: Simplified accelerometer mode of operation

Table 2.1: Specifications for ADXL310 Accelerometers with 5V Supply

Parameter	ADXL210E	Units
Range	$\pm 10$	g
Sensitivity	312	mV/g
Zero $g$ Bias Level	2.5	V
Noise Level	200	$\mu g\sqrt{\text{Hz}}$
Frequency Response	6	kHz

An important aspect of accelerometers is that they also respond to gravitational acceleration. Gravitational acceleration will draw the moving mass  $\mathbf{A}$  downward, deflecting the springs as shown in the illustration on the right side of the figure. This has two important consequences. The first is that the sensor output for the *downward* acceleration due to gravity is interpreted as an *upward* acceleration. The second and more important consequence is that the accelerometer output will have components of both gravitational and kinematic acceleration which cannot be distinguished unless the orientation of the accelerometer is known. However, if the kinematic acceleration is zero, the sensors measures just the static gravitational acceleration and can be used as an inclinometer.

### 2.1.2 Application

Functionally, the ADXL's are simple to implement. Supply voltage of 3 to 5 V is sufficient to power the chip, but since the analog output of the sensors is proportional to the supply voltage, 5 V was used to maximize sensitivity. Capacitors placed on the output pins are used to limit the sensor bandwidth and reduce noise. In this application, the output was band-limited to 50 Hz, and the power supply was 5 V.

## 2.2 Anisotropic Magneto-resistive Sensors

Solid state anisotropic magneto-resistive (AMR) sensors made by Honeywell were used for heading determination. The specifications for the HMC1022 are listed in Table 2.2. The output of these sensors is proportional to the angle that the sensitive axis makes with the surrounding magnetic field. While they are sensitive enough to measure Earth's magnetic field, they are also sensitive to magnetic disturbances, so care must be taken in their application.

Table 2.2: Specifications for HMC1022 with 5 V supply

<b>Parameter</b>	<b>Conditions</b>	<b>Typical</b>	<b>Units</b>
Field Range	Total Applied Field	$\pm 2$	<i>Gauss</i>
Sensitivity	S/R Current = 3A	16	<i>mV/Gauss</i>
Resolution	Bandwidth=10Hz	27	<i><math>\mu</math>Gauss</i>
Noise Level	Noise at 1 Hz	29	<i>nV/Hz</i>
Repeatability Error	3 sweeps across $\pm 2$ gauss	0.05	<i>%FS</i>

### 2.2.1 Mode of Operation:

Honeywell magneto-resistive sensors are made of a nickel-iron thin film deposited on a silicon wafer in the pattern of a resistive Wheatstone bridge. A magnetic field applied normal to the surface of the film will change the bridge resistance causing a corresponding change in voltage output from the sensor. This change in the nickel-iron resistance is called the magnetor-resistive effect [25].

### 2.2.2 Application:

Strong magnetic fields can alter the polarity of the film magnetization, reducing the sensitivity of the bridge. The maximum change in film resistance occurs when the preferred direction of the magnetic field is aligned along the length of the film. A feature of the Honeywell sensors is the set/reset circuit that can be used to restore the sensitivity. A momentary pulse of high current through the set/reset circuit generates a sufficiently strong magnetic field to realign the film magnetization.

## 2.3 Sensor Board

Figure 2.1 shows one of the main difficulties of prototype development with small sensors: While the accelerometer itself is small, the wiring and components required to make it function can be unwieldy. A complete system with multiple accelerometers, magneto-resistive sensors and accompanying circuits would be bulkier still, time consuming to assemble and prone to errors. Accurate mounting of the accelerometers would similarly be difficult to achieve. After selecting the accelerometers and magneto-resistive sensors, a printed circuit board was designed to alleviate these problems with hand prototyping. Shown in Figure 2.3, the resulting sensor board is compact, clean, and has accurate sensor placement.

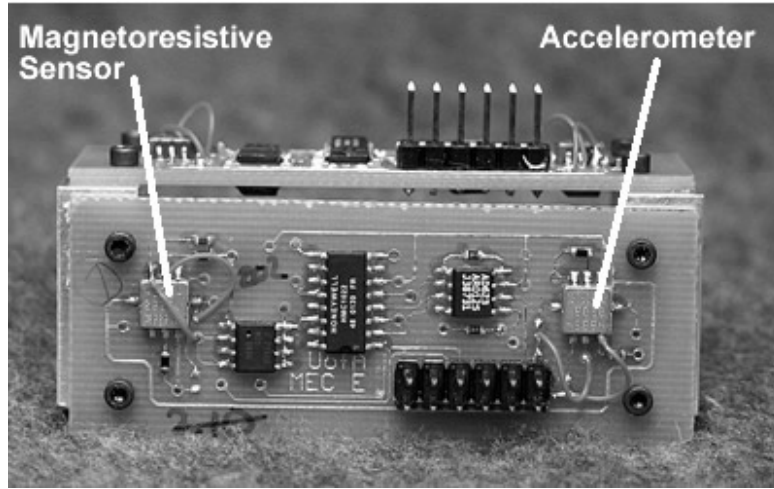


Figure 2.3: Sensor boards mounted orthogonally

Each board has a pair of Analog Devices ADXL210 biaxial accelerometers that are offset by 40 mm to allow angular acceleration measurement. Honeywell HMC1022 biaxial magnetic field sensors and the necessary instrumentation amplifiers are used to provide compassing. All sensor axes are sensitive in the plane of the board, so a pair of boards mounted orthogonally as shown in Figure 2.3 is used to obtain a spatial configuration. The specifications for the sensor board are listed in Table 2.3.

As shown in Table 2.2, the sensitivity of the HMC1022 is 16 mV/Gauss, meaning that in a 0.5 Gauss field typical of Canada, a full rotation of the sensor will generate just  $\pm 8$  mV output change. Thus single supply instrumentation amplifier IC's with a resistor-set gain of 500 were used to magnify the signal to match the input range of the data acquisition system. A MOSFET circuit was also built into the board so that digital signals from the data acquisition card could be used to trigger a reset pulse.

To fasten the sensor boards to the shoe, a small bracket was made on a rapid prototyping machine. Shown in Figure 2.4 with two sensor boards mounted orthogonally, the bracket was held down by the laces of the shoe. A cover, not shown, was also fabricated to protect the boards during testing.

Table 2.3: Specifications for sensor boards

Parameter	Value	Description
General		
Dimensions	25 × 65 mm	Maximum
Power Supply	5 V	Requires External Regulation
Current Draw	60 mA	All sensors operating
Accelerometers		
X Axes	2	Colinear
Y Axes	2	Parallel - Offset 41 mm
Input Range	$\pm 2g$ or $\pm 10g$	Pinouts identical between sensors
Output	0 – 5 V	Nominal
MR		
X Axes	1	Parallel to Accel X axis
Y Axes	1	Parallel to Accel Y axis
Input Range	$\pm 2g$ or $\pm 10g$	Pinouts identical between sensors
Output	0 – 5 V	Nominal
Set/Reset Circuit		Set Only - External digital control



Figure 2.4: Prototype sensor array attached to shoe

## 2.4 Data Acquisition

The complete data acquisition system used for all tests is shown in Figure 2.5. It consists of a laptop running data acquisition software, with an internal PCMCIA data acquisition card made by National Instruments [26]. A parallel cable runs from the data acquisition card to a terminal block housed in an aluminum enclosure. The terminal block connects

signals from the sensors to the appropriate input channel, and also provides power to the sensor boards.



Figure 2.5: Complete Data Acquisition System

Jacks on the enclosure connect the hand trigger line, GPS synchronization line and an auxiliary power line. Longer parallel cables connect the terminal block to the sensor boards mounted on the shoe.

Table 2.4 lists the important specifications of the National Instruments DAQ 6024E data acquisition card used. Software was written to record the analog signals, issue set/reset signals for the magneto-resistive sensors, and generate synchronization signals.

Tests often involved simultaneous data collection with reference equipment, necessitating a means of starting and synchronizing multiple data recorders. Digital ports on the DAQ 6024E were used with a trigger switch to provide clean, discrete pulses that could be broadcast to the multiple systems. Timing software was written so that the user could generate different signals simply by changing the duration the trigger is depressed. In this way, a single switch could be used to start and stop tests as well as indicate multiple kinds of events.

Table 2.4: Specifications for NI DAQ 6024E - As Applied

Parameter	Description
Analog Input	12 bit successive approximation ADC
Channels	16 Single-ended referenced
Input Range	$\pm 5\text{ V}$ , DC coupled
Sampling Rate	Used: $200\text{ Hz}/\text{Channel} \cdot 16\ \text{Channels} = 3.2\text{ kHz}$ Max: 200 kHz
Accuracy:	Noise 1.95 mV Offset 4.42 mV Absolute 6.51 mV
Resolution	2.44 mV
Digital I/O	8 input/output channels
Trigger Response	Rising or falling edge: 10 ns minimum
Warm-up Time	30 min recommended
Operating Temperature	0 to 40 °C

## 2.5 Positional Reference Equipment

### 2.5.1 Laboratory Tests

Laboratory tests were conducted on a treadmill, using the infrared positioning cameras shown in Figure 2.6 as a reference. Made by Qualisys, these cameras track the positions of reflective markers attached to the user's body. After a calibration procedure, as long as two cameras track a marker during the test, its three dimensional position is known.



Figure 2.6: Infrared tracking cameras

The hand trigger on the data acquisition system was used to synchronize the cameras and foot pod during tests. When the button on the trigger was released, a clean digital pulse was sent from the data acquisition card to the cameras, initiating recording. This pulse was also recorded by the data acquisition so that the camera data and foot pod data could be matched exactly. Both systems recorded at 200 Hz.

### 2.5.2 Field Tests

The field tests were conducted in a forested park near Victoria, British Columbia which was suitable because the thick forest cover attenuated GPS signals, but there would be no magnetic interference. A test track of approximately 900 m, with 13 waypoints was surveyed using an electronic total station and retroreflectors. The maximum error in position of all waypoints is less than 50 cm.

During the field tests, the user walked the course wearing the foot pod and carrying a special backpack with the data acquisition system and multiple satellite and inertial systems for reference. A Novatel OEM 4 GPS receiver using a Novatel 600 antenna was used for timing reference and event synchronization. Each time the user pressed the hand

trigger, a digital pulse was sent from the data acquisition system to the OEM 4 where it recorded with 20 ns accuracy [27]. This allowed the events to be matched to relative positions recorded by other receivers which did not have time tagging capability.

In the forest, the satellite signals were sufficiently attenuated that the OEM 4 could not calculate an accurate position. Positional reference during tests was provided by SiRFstarIIe high sensitivity receivers, which is less accurate than the Novatel, but is capable of operating in low signal environments. Position updates with a minimum accuracy of 10 m [28] were recorded at 1 Hz for the duration of the tests.

A triad of Honeywell GG1308 ring laser gyros, (used in a Novatel HG1700 based BlackDiamond™ GPS/INS system) mounted in the backpack provided a reference for the heading calculation. These gyros have a drift error of less than one degree per hour [29].

The equipment, design and logistics for the field trials were provided by Position, Location And Navigation group, Department of Geomatics Engineering, University of Calgary.

## 2.6 Critique of Experimental Design.

One difficult aspect of a broad based research project is handling a wide range of technical issues with limited experience, resources and time. Oversights, mistakes and uninformed decisions can hamper the development of a sound algorithm by affecting the quality of the data available for analysis. That said, if a mistake can be recognized, it can also be assessed to determine its detrimental effect and what action is required. Rebuilding equipment, and repeating experiments may not always be practical, so the designer must rely on critical self evaluation and creative problem solving skills to overcome these challenges. While the results section will demonstrate those parts of the experimental design that were relatively successful, this section is a brief discussion of the "oopses" and "gotchas" that entangled the research project.

### Sensor Monitoring:

The sensors board measured only the user's movement and had no means of monitoring the integrity of the data the sensors were generating. If more A/D channels had been available, a temperature sensor would have been invaluable for removing the temperature offsets observed with the sensors. Calibrated at standard conditions in the lab, the

accelerometers were subject to substantial temperature fluctuations when operating in the field. Without a means of correcting for temperature drift, the error in the algorithm was increased substantially.

Similarly, since the output of the accelerometers and AMR's is ratiometric to the supply voltage, a means of monitoring or regulating the power supply would also improve overall accuracy. Except for decoupling capacitors on the sensors, the SB1's do not have any onboard power supply or regulation. Instead power is supplied from the data acquisition board along a parallel cable that may reach metres. This was unfortunate, because it was found later that there were irregular 40 mV changes in the supply voltage from the data acquisition card which caused corresponding changes in sensor output. Prior to field trials, a power regulator was retrofit to the enclosure, dramatically reducing sensor noise and improving overall confidence in the recorded data.

### **Data Acquisition**

The National Instruments data acquisition card was the most reliable tool on the project. However, some software limitations and oversights meant that it was not used as well as it could have been. In particular, since its analog to digital converter has bipolar input, and all of the sensor signals were monopolar only half of the input range reducing the effective sensitivity. Effectively 1 bit of the 12 bit A/D was wasted.

### **Connector and Wiring Difficulties**

Possibly the most frustrating part of the experimental process was troubleshooting intermittent problems that turned out to be caused by a failed connector or cable. These failures occur because the designer does not properly appreciate the operating environment the equipment will be working in. Ignoring advice to use strain reliefs and robust connectors he chooses instead to use something that is quick and inexpensive. It works temporarily and then fails at an inconvenient time ruining an experiment. While this occurred occasionally with the prototype equipment, it also occurred with maddening regularity on expensive pieces of commercial lab equipment. Though they add cost to already modest research budgets, investing in proper connectors, wiring and switches helps ensure that data is properly recorded.

**Experimental Complexity**

In some experiments, up to four GPS receivers, the ring laser gyros, and shoe mounted sensor arrays would all be recording simultaneously. In addition, concurrent tests added inertial navigation units. This led to a staggering data rate, and a complex array of problems including powering, recording and synchronizing so many systems. The connector and wiring difficulties mentioned previously only compounded the problem. It was rare to finish a test and have a good data set from all equipment.

**Summary of Critique**

The majority of the mistakes discussed here are the author's own, and have not been brought up to use an excuse but rather to highlight the complications that inexperience and impatience bring to the experimental process. Taking the time to understand the equipment and test parameters prior will improve the quality of the data recorded, and improve the faith that the experimenter can place on the results.

## Chapter 3

# Gait Event Identification By Accelerometry

### 3.1 Introduction

The methods that will be used for measuring stride length and heading use the cyclical, segmented nature of human walking to resolve the sensor frame orientation. Implicit in the development of these techniques is the assumption that identifying the necessary gait events from the foot mounted sensors is possible. As reviewed in the first chapter, gait event detection is not trivial and outside of the laboratory, foot switches and accelerometers are commonly used to detect stride events.

While foot switches indicate when the foot strikes or leaves the ground they may not function reliably on some surfaces, and are insensitive to other parts of the gait cycle. Using the signals from the sensors that already exist in the pedestrian navigation system is more efficient than adding separate ones for gait detection. Frequently, accelerometer based stride detection methods simply use the accelerations peaks accompanying foot strike to locate stride events but do not detect separate gait events.

Shoe mounted sensors are well suited for gait study applications because the intermittent motion of the foot during walking creates regular patterns of acceleration. Thus, as well as resolving the number of steps the user has taken, important gait events such as stance phase initiation, toe off, and swing phase may also be identified from the sensor signal. This chapter will illustrate some of the techniques used to tease subtle information about a person's walk from the output of the accelerometers mounted on the foot.

### 3.2 Stride Events and Accelerometer Signals

To aid the discussion of gait identification, the illustration of the normal walking cycle is shown again in Figure 3.1. We now consider qualitatively how accelerometers mounted on the foot of the darkened leg will respond to the movement. The accelerometer output measured during a representative stride is shown in Figure 3.2 for comparison.

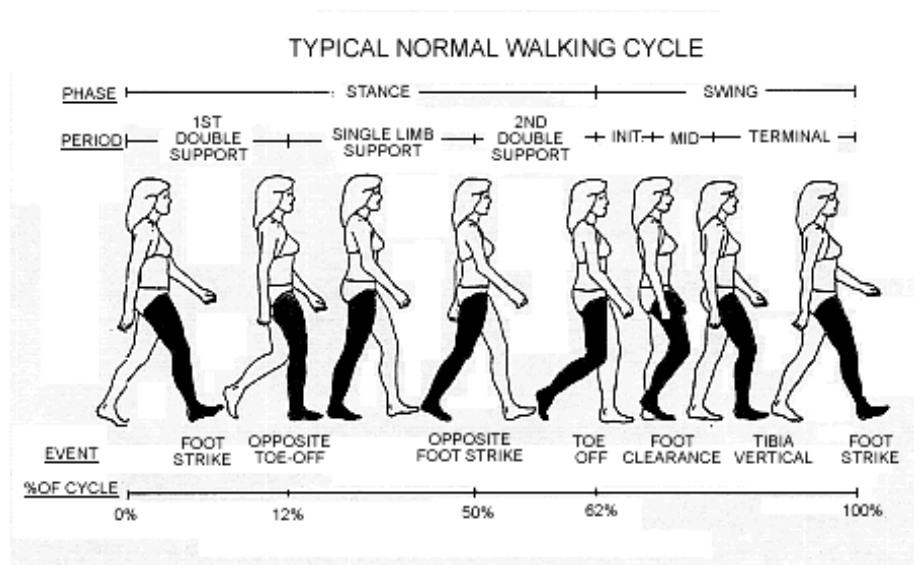


Figure 3.1: Typical Normal Walking Cycle. Adapted from [3]

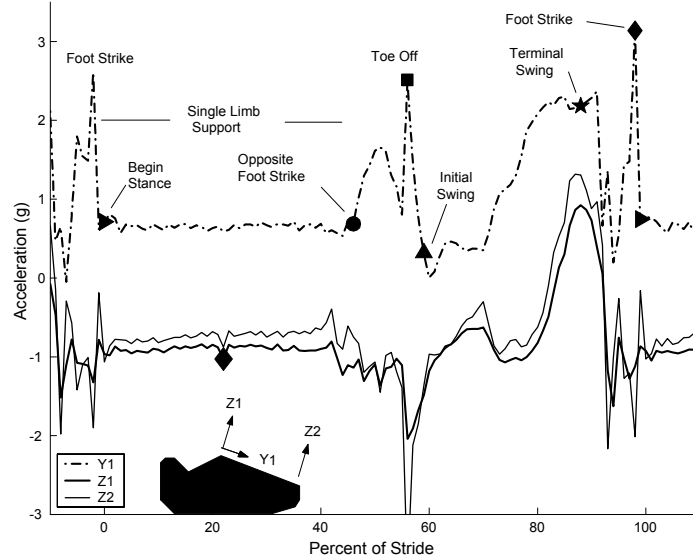


Figure 3.2: Acceleration Signals and Events

Three accelerometers are mounted on the foot in the configuration shown in the lower left of the figure. Two parallel offset accelerometers labelled  $Z_1$  and  $Z_2$  measure the *tangential* component of acceleration, and a single orthogonal accelerometer, labelled  $Y_1$ , measures the *normal* acceleration. The acceleration is plotted against percentage of stride, instead of time, so that features of the signal can be matched to the gait cycle events shown in Figure 3.1.

The gait cycle begins just after the foot strikes the ground, usually heel first, causing a large peak acceleration followed by oscillation as the impact is dampened by the shoe and by the user's body. Weight is transferred forward and the opposite foot toes off beginning a period of single limb support (marked with a triangle) where our instrumented foot is stationary and the sensor output will be steady. Recall that although the foot is not accelerating at this moment, the accelerometers will still measure Earth's gravitational acceleration. As the foot rotates forward, the acceleration sensed by each axis will change slightly then more rapidly after opposite foot strikes occurs (marked with a circle). The rotation of the foot accelerates until toe-off occurs (square symbol) initiating swing phase. The sensed acceleration rises from the initial swing phase (triangle symbol) as the foot begins to travel forward. The forward velocity of the foot increases through mid-swing and then slows prior to foot strike creating the sudden changes in acceleration observed

between the star and diamond markers.

### 3.3 Useful Signal Manipulations

Finding the gait events in the measured acceleration signals is relatively easy by eye. Automating the identification process to reliably handle the different signals that come from individual walking styles and surface conditions is more challenging. Figure 3.3 shows three signals generated by manipulating the measured acceleration to aid gait identification by magnifying the events of interest and diminishing the irrelevant ones. The acceleration *energy*, *product*, and *sum* signals and their uses are discussed in the following sections.

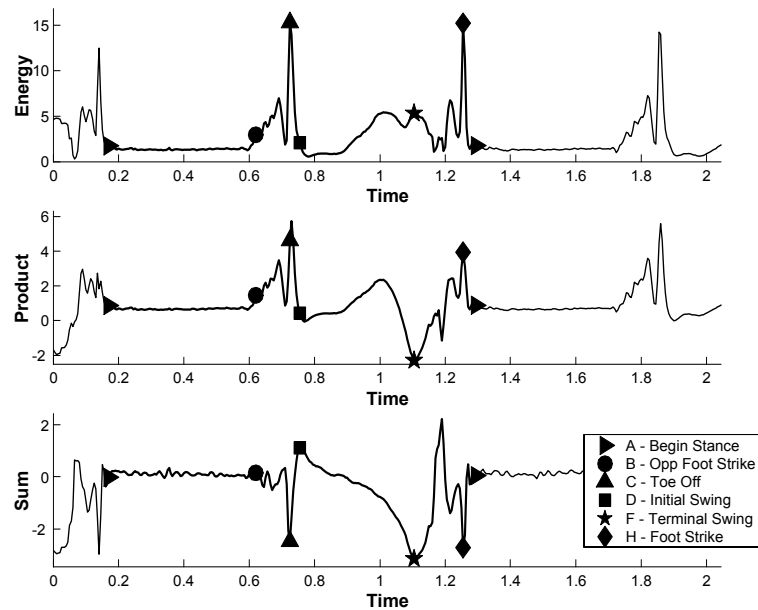


Figure 3.3: Stride detection signals derived from acceleration

#### 3.3.1 Acceleration Energy

Shown in the upper plot of Figure 3.3, the *energy* of the signal is the sum of the squared acceleration measured by orthogonal sensor axes.

$$Energy = Y_1^2 + Z_1^2$$

It is useful because it amplifies periods of high dynamics, flattens periods of low dynamics and generates a signal that is positive by definition. The progression of events in the energy signal is well defined. During the early stance phase (A-B), when the foot is stationary, the accelerometers measure gravity only so  $Y_1^2 + Z_1^2 = 1 g^2$ . Squaring the sum creates a noticeably higher and narrower peak at toe-off (C) than is observed in the original acceleration signal. A useful and detectable event occurs in the initial swing phase (D) when the acceleration energy is briefly less than at stance phase before a sustained rise to the terminal swing phase (F). The last period of the gait cycle has high amplitude oscillations ending with a peak at foot strike (H).

### 3.3.2 Acceleration Product

The second useful signal that can be constructed from the footpod data is acceleration *product*. Where the energy signal helps us separate relative magnitudes of the gait dynamics, the product of the orthogonal axes  $Y_1$  and  $Z_1$  identifies periods where the accelerations have opposite sign.

$$Product = Y_1 Z_1$$

The familiar pattern of the gait cycle is visible in the product as shown in the middle plot of Figure 3.3. Through the entire stance phase, and initial swing phase (A-D), the product signal is similar in pattern to the energy signal, but of lower magnitude. During the late swing phase however, the product signal distinguishes the terminal swing phase with a negative minimum (F). In the energy signal, this event is harder to resolve because of its proximity to a peak of similar magnitude.

### 3.3.3 Acceleration Sum

A third useful signal is the *sum* of the acceleration measured by orthogonal axes.

$$Sum = Y_1 + Z_1$$

Shown in the bottom plot of Figure 3.3, the acceleration sum accentuates the initial and terminal swing phases events. In particular it creates a sharp minimum during the initial swing (D) making it much easier to detect than is possible with the other methods. Because it is a first order equation, there is much more variance in the signal during stance phase (A and B) making it less suitable for identifying these events.

### 3.4 Detecting Events

Having manipulated the measured acceleration into signals that highlight various gait events, we must establish some test criteria for detecting them. Looking ahead to practical applications, it will be important to be able to register events as soon as possible after they happen, to maximize the responsiveness of the stride length measurement. This means that the identification algorithm should work within a minimal number of samples. Also, it should be versatile enough to work on a wide range of walking speeds and conditions to minimize user calibrations.

Tests may begin with the user already walking, so our first challenge is to determine where in the gait cycle the user is at the start of the recording. This may mean searching through a second or two of data for a recognizable event such as stance phase, and then working backwards to the start. Once the current position in the gait cycle is known, it is possible to anticipate the next event and test for expected values may be simplified. We now examine ways of detecting these events.

#### 3.4.1 Magnitude Thresholds

The simplest form of event detection is to test for places where the signal crosses some threshold value. For example, we may say that if the last five samples of the energy signal have a value close to  $1 g^2$  then it must now be stance phase. Or we may look for foot strike events simply by finding energy values greater than  $10 g^2$ . The risk in using only the value of the signal for detection is that a small unexpected change in conditions can create false or intermittent event detections. A small error in calibrating the sensor bias can shift the entire energy signal so that it never reaches  $1 g^2$ . Similarly, a threshold value set for a medium walk may not detect heel strikes of a soft or slow walker while a heavy walker could trip the threshold multiple times in a single stride.

Often deciding if an event has occurred depends on whether some variable is greater or less than a chosen threshold. It is important that the variable being compared is sensitive only to the dynamics of the signal that are due to walking.

#### 3.4.2 Variance Thresholds

The variance,  $s_n^2$  of  $n$  data samples is

$$s_{n_j}^2 = \frac{1}{n} \sum_{i=j}^{i=j+n} (x_i - \bar{x}_j)^2$$

Where  $\bar{x}_j$  is the mean of the  $n$  samples.

$$\bar{x}_j = \frac{1}{n} \sum_{i=j}^{i=j+n} x_i$$

Properly applied, the variance of the energy or product signals can be useful for detecting gait events where the signal changes suddenly, such as heel strike and stance phase initiation. Because the variance measures the relative stability of the signal, it is insensitive to bias and temperature drift in the sensors, and threshold detections using the variance will work more reliably. In the upper plot of Figure 3.4, is the energy signal from measurements over a few strides.

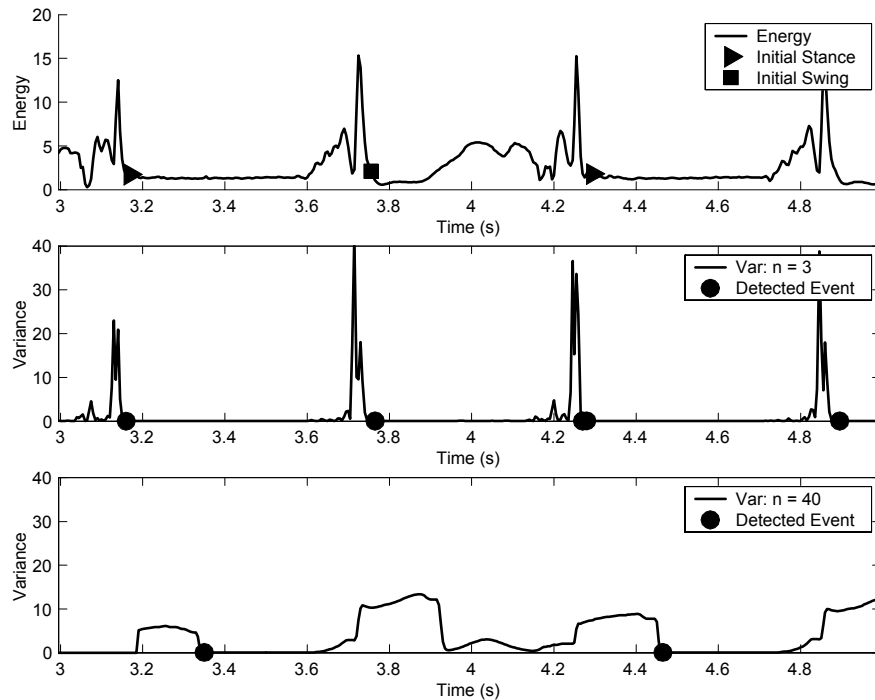


Figure 3.4: Detecting Gait Events With Variance

To demonstrate how the choice of sample size affects event detection, the variance calculated with three samples (middle plot) is compared to the variance calculated with forty samples (lower plot). The initiation of stance phase is marked with a triangle in the upper plot. To locate this event we search for periods where the variance drops suddenly from a high maximum ( $s_n^2 > 5$ ) to a low steady value ( $s_n^2 < 0.1$ ) within just a few samples.

Circular symbols in the lower plots indicate where these conditions are satisfied.

The middle plot of Figure 3.4 shows that the variance calculated from just three samples responds to rapid changes in energy with large amplitude spikes. There is little time delay between the gait event and its detection, but extra events corresponding to the initial swing phase appear. This is because the period of slow energy change at initial swing phase cannot be distinguished from the period of no energy change in stance phase by calculating variance with such a small sample size.

Using a larger number of samples, such as  $n = 40$  shown in the lowest plot, means that the calculated variance will be more sensitive to slower rates of energy change. As desired, the event markers in this plot correspond only to the initiation of stance phase, but the detections occur almost a quarter of a second later due to the number of samples required for the calculation.

If variance of a manipulated signal is to be used for gait event detection, the sample size  $n$  must be chosen appropriately so that the variance test is adequately sensitive to slow signal changes and adequately responsive to fast ones. With appropriately chosen thresholds, it was found that a sample size of five to ten was suitable for gait event detection over a range of walking speeds.

### 3.4.3 Local Extrema

An alternative method to using signal variance for detecting events in a signal is to look for peaks or troughs. In the simplest definition, a maxima is a point of greater magnitude than the points preceding or following. Thus local extrema can be rapidly detected by considering just three samples as follows:

$$\begin{aligned} x_{i-1} \text{ is a maximum if: } & x_{i-1} > x_i \cap x_{i-1} > x_{i-2} \\ x_{i-1} \text{ is a minimum if: } & x_{i-1} < x_i \cap x_{i-1} < x_{i-2} \end{aligned}$$

Figure 3.5 shows a small sample of the energy signal. Triangular markers pointing up or down indicate respectively the locations of local maxima and minima. At first glance it appears that the detection of "useful" peaks such as at  $t = 4.25$  s may be obscured by the clutter of extrema detected in the noise of the stationary period after  $t = 4.3$  s. However, this in fact demonstrates that the frequency and relative magnitude of extrema found with this simple technique may be used to locate a variety of event types.

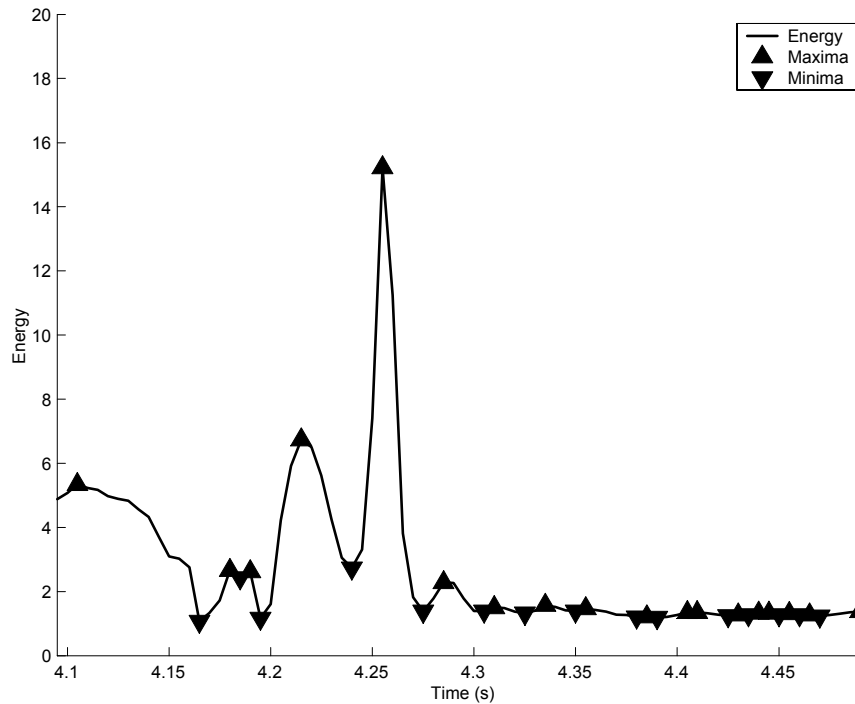


Figure 3.5: Detection of local maxima and minima in a signal

When the signal is not changing, local maxima and minima will be of approximately equal magnitude and will occur in rapid succession because of signal noise. A true maximum will be much larger in magnitude than the minima surrounding it. An extrema occurring after a period of monotonic change will be separated from the previous minima by a longer period of time than a rapid peak will.

### 3.5 Gait Event Sequence and Gait Frequency Windowing

A person walking normally follows a well determined pattern of motion, meaning that gait events will always occur in the same order. Once the stride detection routine has correctly identified a gait event, the next gait event is known. This means that the event confusion illustrated in the middle plot of Figure 3.4 is only relevant while trying to identify the first event in a recording.

To get a positive location in the gait cycle, the manipulated gait signals are tested for a particular event, such as stance phase initiation ( $A$  in Figure 3.3). If the variance

Table 3.1: Gait Event Detection Sequence

	<b>Event</b>	<b>% Stride</b>	<b>Energy</b>	<b>Product</b>	<b>Sum</b>
<b>A</b>	Initial Stance	0	Variance drops	Variance drops	Not used
<b>B</b>	Opp. Foot Strike	50	Variance rises	Variance rises	Not used
<b>C</b>	Toe Off	60	Sharp max	Sharp max	Local max
<b>D</b>	Initial Swing	65	Variance drops	Variance drops	Local min
<b>F</b>	Terminal Swing	85	Not Used	Local Min	Local min
<b>H</b>	Foot Strike	95	Sharp max	Not Used	Sharp max

and local extrema techniques just described do not uniquely identify an event, the event can be confirmed by the properties of the following event. In this way, stance phase initiation is confirmed if opposite toe-off ( $B$ ) is detected next, rather than terminal swing ( $F$ ). Again, after the position in the gait cycle is established, it is only necessary to test for the conditions of the next event in the sequence.

Starting from rest, it takes just a few strides for a person to reach their preferred walking speed, after which the frequency of footsteps will be fairly regular [3]. It is possible to use the duration of the most recent stride cycle to predict when the next foot strike is likely to occur, to reject spurious strides detections and to indicate when a stride has possibly been missed [8]. This technique can be applied within the stride to speed detection by narrowing the period in which a particular event is expected to occur.

### 3.6 Gait Event Detection

The techniques of signal manipulation, variance and extrema testing, and event sequence are all applied to aid the detection of gait events. Table 3.1 describes the gait events in the order they occur and the approximate period in which they are expected to occur. Variance and local extrema conditions of each manipulated are also listed. Where possible the confidence of the detection is increased by testing multiple signals and then using the average detected time.

Making the first stance phase identification is the most important step, as after that it is simply a matter of searching a short window of data for the conditions of the next gait event. After this first detection, the signal that has elapsed prior to stance phase may be searched in reverse for gait events until the beginning of the recording is reached, though since this is normally less than a stride's worth of data it may not significantly improve the following stride length estimation.

### 3.7 Summary

Shoe mounted accelerometers may be used to identify particular events of the human gait cycle. Since the progression of these events is consistent between strides, the measured acceleration signal can be searched for characteristic patterns to detect the occurrence of gait events such as foot strike, stance phase and toe off. The measured acceleration is manipulated to generate the acceleration *energy*, *product*, and *sum* signals which accentuate different events in the stride, making them easier to identify. Applying techniques that are sensitive to the patterns of change in the signal rather than simply its magnitude, the stride detection algorithm can be made robust with respect to errors in sensor calibration and variation in walking conditions.

## Chapter 4

# Stride Length Measurement by Accelerometry

In this chapter, the accelerometer based stride length measurement method is described in detail, beginning with an explanation of how the difference in acceleration measured by two parallel accelerometers is used to measure angular acceleration. Integration of angular acceleration to angular position, and stance phase static acceleration measurement is used to calculate the sensor angle through the stride. This sensor angle profile provides a means to extract the horizontal acceleration from accelerations measured in a sensor frame that constantly rotates as a person walks. Horizontal stride velocity is integrated from the horizontal acceleration, and the mean stride velocity is used to calculate the stride length. Important practical aspects of the method are also discussed.

### 4.1 General Plane Motion

Figure 4.1 shows a solid body which moves in the vertical ( $YZ$ ) plane and is free to rotate in the plane (ie about  $X$  axis). Biaxial accelerometers, aligned in the vertical plane are mounted at the points  $A$  and  $B$  on the body. For simplicity, point  $A$  will be defined as the origin of the body frame, and point  $B$  is located a distance  $r$  along the body  $y$  axis.

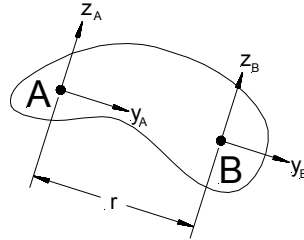


Figure 4.1: Rigid body with parallel offset planar accelerometers

The accelerometers are attached at these points such that the positive direction of the sensitive axes are aligned with the positive axes of the body frame. In this way, the  $z$  accelerometer axes are parallel, but offset by  $r$ , and the  $y$  accelerometer axes are collinear. Before measuring acceleration at these points, the motion of point  $B$  with respect to  $A$  is considered.

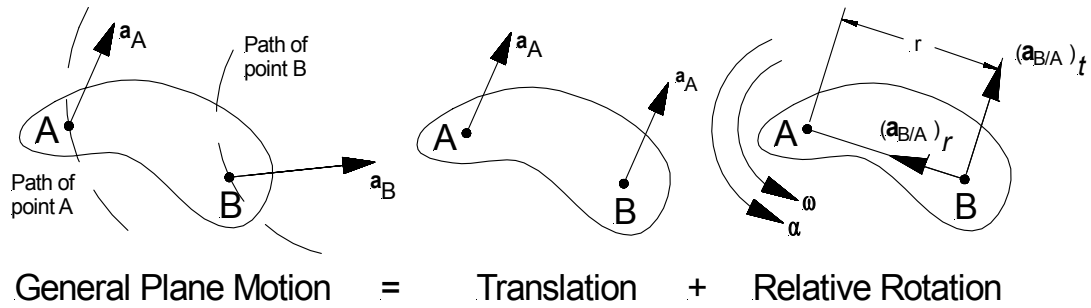


Figure 4.2: Components of General Plane Motion

The body shown in Figure 4.1 moves without restriction in the  $yz$  plane. General plane motion of the body results in differing displacements and accelerations at  $A$  and  $B$  as shown at the left of Figure 4.2. The two illustrations on the right of the figure show how the acceleration at  $B$  can be expressed as the vector sum of the acceleration of point  $A$ , and the relative acceleration of  $B$  with respect to  $A$  due to the rotation of the body.

$$\vec{a}_B = \vec{a}_A + \vec{a}_{B/A} \quad (4.1)$$

That is, the acceleration of  $B$  is the superposition of the translational acceleration of  $A$ , and the rotational acceleration of  $B$  about  $A$ . The relative rotation component  $\vec{a}_{B/A}$  is described in terms of the angular velocity  $\vec{\omega} = [\omega, 0, 0]$  and the angular acceleration

$\vec{\alpha} = [\alpha, 0, 0]$  as:

$$\vec{a}_{B/A} = \vec{\alpha} \times \vec{r} - \vec{\omega} \times (\vec{\omega} \times \vec{r}) \quad (4.2)$$

Where  $\vec{r} = [0, r, 0]$  is the displacement vector between  $A$  and  $B$ . Substituting Eq. 4.2 into Eq. 4.1 gives:

$$\vec{a}_B = a_A + \vec{\alpha} \times \vec{r} - \vec{\omega} \times (\vec{\omega} \times \vec{r}) \quad (4.3)$$

Having established a relationship between the accelerations at the two points, we describe how accelerometers are used to measure planar motion.

## 4.2 Accelerometry

Accelerometer output is the scalar projection of gravitational and kinematic acceleration along the direction of the sensitive axis.

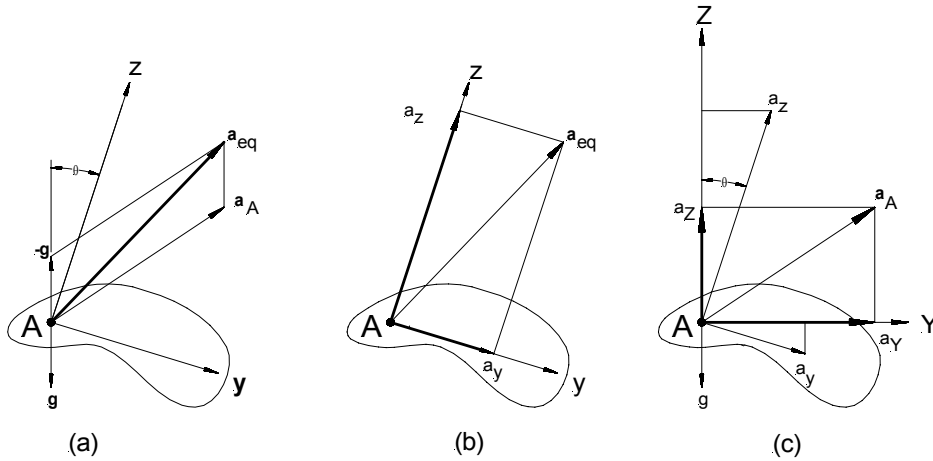


Figure 4.3: Equivalent Acceleration

Part (a) of Figure 4.3, shows how the gravitational acceleration vector  $-\vec{g}$ , and the kinematic acceleration vector  $\vec{a}_A$  are summed, yielding the *equivalent acceleration*  $\vec{a}_{eq}$ . The biaxial accelerometer at  $A$  is sensitive to equivalent acceleration, not simply the kinematic acceleration.

$$\vec{a}_{eq} = \vec{a}_A - \vec{g}$$

(Recall from the sensor description in Chapter 2 that although the acceleration of gravity  $\vec{g}$  is directed downward, it is interpreted by the sensor as an upward acceleration  $-\vec{g}$ ).

Illustration (b) of the figure shows how the equivalent acceleration is projected onto the  $y$  and  $z$  axes of the accelerometer. For example, the acceleration transduced by  $y$  axis of the sensor is the scalar projection of the equivalent acceleration in the  $y$  direction.

$$\begin{aligned} a_y &= \vec{a}_{eq} \cdot \vec{y} \\ &= (\vec{a}_A - \vec{g}) \cdot \vec{y} \end{aligned}$$

Similarly

$$a_z = (\vec{a}_A - \vec{g}) \cdot \vec{z}$$

Unless the orientation  $\theta$  of the sensor frame with respect to the global frame is known, it is impossible to distinguish the gravitational component of acceleration. Illustration (c) of the figure shows that if  $\theta$  can be determined, the global horizontal and vertical accelerations ( $a_Y, a_Z$ ) can be projected from the sensor frame acceleration measurements ( $a_y, a_z$ ). The components are summed graphically in Figure 4.4.

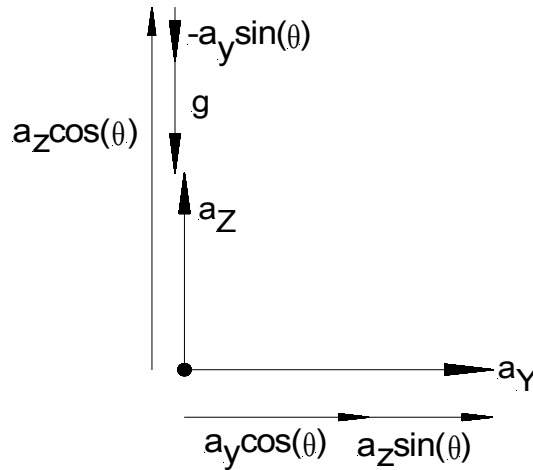


Figure 4.4: Components of horizontal and vertical acceleration

Using the more detailed addition of the vector components in Figure 4.4 as a guide, we write equations for the vertical and horizontal acceleration.

$$a_Y = a_y \cos \theta + a_z \sin \theta \quad (4.4)$$

$$a_Z = a_z \cos \theta - a_y \sin \theta - g \quad (4.5)$$

Equations 4.4 and 4.5 show that it is possible with a biaxial accelerometer to remove the gravitational component of acceleration, provided that the orientation  $\theta$  of the sensor

is known with respect to vertical. Determining the orientation  $\theta$  is not trivial, and is discussed in the following sections.

### 4.3 Orientation Angle

#### 4.3.1 Inclinometry

The simplest method of determining  $\theta$  is the special case when the kinematic acceleration is zero. If the body is stationary, only the gravitational component is sensed, and the accelerometer can be used as an inclinometer [24].

$$a_y = (\vec{a}_A - \vec{g}) \cdot \vec{y} = -\vec{g} \cdot \vec{y} = -|\vec{g}| \cos\left(\theta - \frac{\pi}{2}\right) = -|\vec{g}| \sin\theta \quad (4.6)$$

$$a_z = (\vec{a}_A - \vec{g}) \cdot \vec{z} = -\vec{g} \cdot \vec{z} = -|\vec{g}| \cos\theta \quad (4.7)$$

$$\tan\theta = \frac{a_y}{a_z} \quad (4.8)$$

Though direct, this method is practical only when the body is known to be stationary, which is not particularly useful since we want to measure acceleration when the body is moving. As explained later, measuring sensor angle by inclinometry is still important to the stride length calculation.

#### 4.3.2 Angular Acceleration and Angular Velocity Measurement

If the body is moving with general plane motion, it is no longer valid to use Eq. 4.8 to measure  $\theta$  since the kinematic component of acceleration is non-zero. Since the inclination,  $\theta$ , cannot be measured directly during general plane motion of the body, we will look for ways to get other rotational information that may allow  $\theta$  to be determined. We begin by considering the  $z$  acceleration measured at  $A$  and  $B$ .

$$a_{Az} = (\vec{a}_A - \vec{g}) \cdot \vec{z} \quad (4.9)$$

$$a_{Bz} = (\vec{a}_B - \vec{g}) \cdot \vec{z}$$

We can use 4.3 to give us

$$a_{Bz} = (\vec{a}_A + \vec{\alpha} \times \vec{r} - \vec{\omega} \times (\vec{\omega} \times \vec{r}) - \vec{g}) \cdot \vec{z} \quad (4.10)$$

Subtracting 4.9 from 4.10 yields the difference in measured acceleration,  $\Delta a_z$ .

$$\begin{aligned}\Delta a_z &= a_{Bz} - a_{Az} \\ &= (\vec{a}_A + \vec{\alpha} \times \vec{r} - \vec{\omega} \times (\vec{\omega} \times \vec{r}) - \vec{g}) \cdot \vec{z} - (\vec{a}_A - \vec{g}) \cdot \vec{z}\end{aligned}$$

Since the axes are parallel, both are projected onto  $\vec{z}$ . Using the commutative property of the scalar product we obtain

$$\begin{aligned}\Delta a_z &= ((\vec{a}_A + \vec{\alpha} \times \vec{r} - \vec{\omega} \times (\vec{\omega} \times \vec{r})) - \vec{a}_A + \vec{g}) \cdot \vec{z} \\ &= (\vec{\alpha} \times \vec{r} - \vec{\omega} \times (\vec{\omega} \times \vec{r})) \cdot \vec{z}\end{aligned}$$

Similarly

$$\Delta a_y = (\vec{\alpha} \times \vec{r} - \vec{\omega} \times (\vec{\omega} \times \vec{r})) \cdot \vec{y}$$

By taking the difference in measured acceleration between parallel accelerometers, we have eliminated the translational and gravitational components common to both sensors leaving only the rotational components. We have assumed planar motion, with rotation about the  $x$  axis so

$$\begin{aligned}\vec{\alpha} &= [\alpha, 0, 0] \\ \vec{\omega} &= [w, 0, 0] \\ \vec{r} &= [0, r, 0] \\ \vec{\alpha} \times \vec{r} &= [0, 0, r\alpha] \\ -\vec{\omega} \times (\vec{\omega} \times \vec{r}) &= [0, -r\omega^2, 0]\end{aligned}$$

We project the rotational acceleration onto the sensor axes by taking the scalar product with unit vectors parallel to the accelerometers

$$\begin{aligned}\vec{y} &= [0, 1, 0] \\ \vec{z} &= [0, 0, 1]\end{aligned}$$

$$\begin{aligned}\Delta a_z &= a_{Bz} - a_{Az} \\ &= (\vec{\alpha} \times \vec{r} - \vec{\omega} \times (\vec{\omega} \times \vec{r})) \cdot \vec{z} \\ &= [r\omega^2, r\alpha, 0] \cdot [0, 1, 0] \\ \Delta a_z &= r\alpha\end{aligned}$$

Finally

$$\alpha = \frac{\Delta a_z}{r} \quad (4.11)$$

That is, the difference in acceleration between two parallel offset accelerometers is equal to the angular acceleration multiplied by the distance between them. Similarly, by taking the difference of two collinear accelerometers, we get a relationship for the magnitude of the angular velocity.

$$\begin{aligned} \Delta a_y &= a_{By} - a_{Ay} \\ &= (\vec{\alpha} \times \vec{r} - \vec{\omega} \times (\vec{\omega} \times \vec{r})) \cdot \vec{y} \\ &= [r\omega^2, r\alpha, 0] \cdot [1, 0, 0] \\ \Delta a_y &= r\omega^2 \\ \omega^2 &= \frac{\Delta a_y}{r} \end{aligned} \quad (4.12)$$

Thus while the body is moving the angular position cannot be measured directly, but the magnitude of angular velocity and the angular acceleration can both be measured from the differences in the acceleration measured at  $A$  and  $B$ . With known or assumed initial conditions for  $\alpha$  and  $\omega$ , the inclination  $\theta$  can be determined by temporal integration.

#### 4.4 Stride Length Calculation

As described in the biomechanics section of Chapter 1, human gait is a segmented cyclical motion. The foot begins stationary, then is lifted and accelerated as it is carried forward during a stride. The stride ends with a heel strike and the foot is momentarily stationary again during the next stance phase and the cycle repeats itself. We can use this repetitive nature of human walking with the techniques developed above to measure the foot angle profile during the stride.

In this application, the rigid body just discussed is the sensor board attached to the user's foot and oriented in the sagittal (user  $yz$ ) plane. Using the methods described in Chapter 3 to detect the stance phase, we begin the stride length measurement by determining the inclination angle of the sensor board. Here the accelerometers are measuring only gravity so we use Eq 4.8 for the initial value for the foot angle.

$$\theta_0 = \arctan\left(\frac{a_y}{a_z}\right)$$

To calculate the sensor angle profile and determine the length of step taken,  $n$  acceleration samples, recorded at interval  $\Delta t$ , are recorded over the stride from the current detected stance phase (at time  $t = t_0$ ) to the next detected stance phase (at  $t = t_n = t_0 + n\Delta t$ ). The angular acceleration profile over the stride is calculated using the parallel offset accelerometer technique just described in Eq (4.11).

$$\alpha(t) = \frac{\Delta a_y(t)}{r}$$

Angular velocity of the foot through the stride can be integrated from the angular acceleration profile.

$$\omega(t) = \omega(t_0) + \int_{t_0}^{t_n} \alpha(t) dt$$

We haven't a means of measuring  $\omega(t_0)$ , but  $t_0$  occurs at the beginning of stance phase so we can assume that the initial angular velocity of the foot is zero.

$$\omega(t) = \int_{t_0}^{t_n} \alpha(t) dt$$

A second integration gives us the sensor angle profile, using the initial value measured at  $t_0$  as described above.

$$\theta(t) = \theta_0 + \int_{t_0}^{t_n} \omega(t) dt$$

Now that we have the foot angle profile  $\theta(t)$ , we can apply Eqs. (4.5) and (4.4) to extract the horizontal and vertical components of acceleration as shown in Figure 4.5.

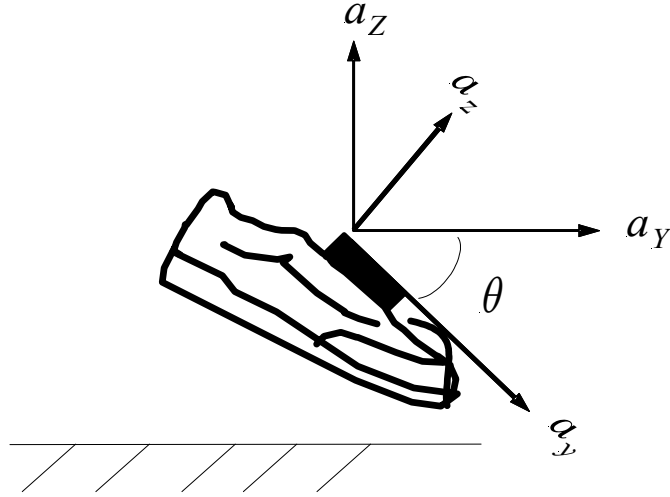


Figure 4.5: Resolving acceleration into vertical and horizontal components using foot angle.

$$a_Z(t) = a_z \cos \theta(t) - a_y \sin \theta(t) + g \quad (4.13)$$

$$a_Y(t) = a_y \cos \theta(t) + a_z \sin \theta(t) \quad (4.14)$$

Knowing that the foot is stationary during the stance phase (that is,  $v_{y_0} = 0, v_{z_0} = 0$ ), the horizontal and vertical velocity can be integrated directly from the acceleration

$$v_Y(t) = \int_{t_0}^{t_n} a_Y(t) dt$$

$$v_Z(t) = \int_{t_0}^{t_n} a_Z(t) dt$$

The horizontal and vertical travel can be calculated by another integration, or simply by the product of the average velocities and the stride time. The stride time  $\Delta t$  is the time elapsed between stance phases:

$$\Delta t = t_n - t_0$$

The mean stride velocity is

$$\bar{v} = \frac{1}{n} \sum_{t=t_0}^{t_n} v(t)$$

So the horizontal and vertical distance travelled during the stride are

$$s_Y = \frac{\Delta t}{n} \sum_1^n v_Y(t)$$

$$s_Z = \frac{\Delta t}{n} \sum_{t=t_0}^{t_n} v_Z(t)$$

With the sensors and data acquisition used in this research, uncertainty due to measurement resolution is expected to be  $\pm 2$  cm per stride under ideal conditions. Appendix A details the calculations for this error estimation.

## 4.5 Practical Considerations of Numerical Integration

The relative simplicity of this stride length measurement method makes one wonder why this technique is not more commonly applied. While it relies on mathematics and kinematics taught in early undergraduate courses, there are several challenges to overcome in implementing a practical version of it. The most common argument against measuring distance by temporal integration of acceleration data is that the solution will rapidly diverge due to drift. By measuring the sensor angle during each stance phase, the accumulation of integration error is limited to the relatively brief period of the stride. We now examine the nature of the error growth due to numerical integration.

### 4.5.1 Fourier Series Representation and Integration

Since the angular acceleration signal is the first signal to be integrated, it will serve as a practical example for the following discussion. Figure 4.6 shows the measured angular acceleration  $\alpha(t)$  (top plot) and the corresponding frequency spectrum (lower plot) of a person walking on a treadmill at 1.1 m/s. In the upper plot we see that the signal repeats itself approximately every second. The frequency spectrum shows that the signal contains multiple frequencies, mostly concentrated below 20 Hz, with the largest components below 5 Hz.

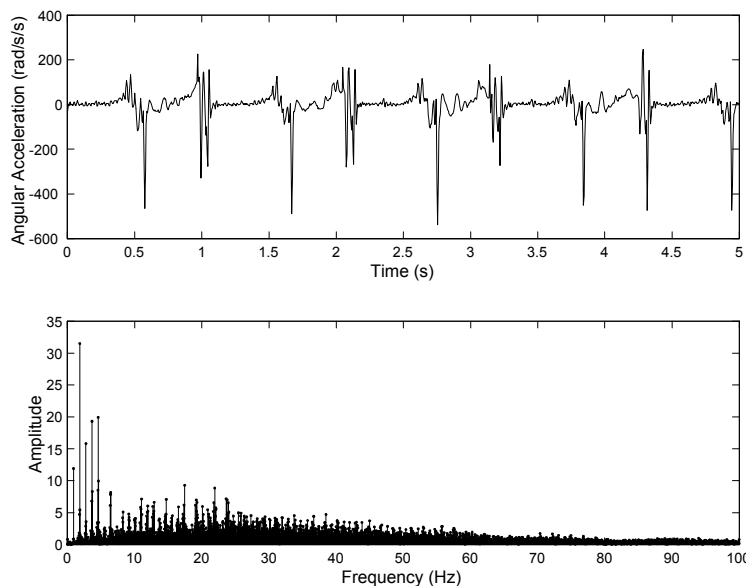


Figure 4.6: Angular acceleration and frequency spectrum

A periodic signal composed of multiple frequencies such as  $\alpha(t)$  is called *complex periodic*. A Fourier series is used to represent complex periodic signals as a function of time,  $t$ , and fundamental frequency  $f_o$ . The Fourier series model  $\alpha_F(t)$  of the measured angular acceleration  $\alpha(t)$  is:

$$\alpha_F(t) = \frac{a_0}{2} + \sum_{k=1}^{\infty} [a_k \cos(2\pi k f_o t)] + \sum_{k=1}^{\infty} [b_k \sin(2\pi k f_o t)] \quad (4.15)$$

Where  $a_0$  is the mean of the signal, and  $a_k, b_k$  are the real and imaginary components respectively of the  $k^{th}$  harmonic of the fundamental frequency  $f_o$ . Equation 4.15 shows mathematically how each frequency harmonic  $k f_o$  contributes to the makeup of  $\alpha_F(t)$ . The Fourier series representation of a discrete signal is useful because, being a function of continuous variables, it can be integrated analytically. This provides a reference with which to compare the direct numerical integration of the signal. To get an analytical representation of  $\omega(t)$ , we integrate the Fourier series representation of  $\alpha(t)$ :

$$\omega_F(t) = \int \alpha_F(t) dt = \frac{a_0}{2} t + \frac{1}{2\pi f_o} \left( \sum_{k=1}^{\infty} \left[ \frac{a_k}{k} \sin(2\pi k f_o t) \right] - \sum_{k=1}^{\infty} \left[ \frac{b_k}{k} \cos(2\pi k f_o t) \right] \right) + K_1$$

Under ideal conditions, the foot angle at the start of stance phase  $\theta_0$ , will be approximately the same every stride, which requires that the mean of  $\alpha(t)$  is zero. Immediately

we see that if the mean value  $a_0$  of  $\alpha(t)$  is non-zero due to walking irregularities or sensor error, then integration produces a linear drift component into the signal proportional to time  $t$ .

$K_1$  is an integration constant which can be determined if  $\omega_F$  is known at some instant. Assuming that the foot is stationary during stance phase, we apply the initial condition  $\omega_F(0) = 0$ , allowing us to determine:

$$K_1 = \frac{1}{2\pi f_o} \sum_{k=1}^{\infty} \frac{b_k}{k}$$

Integrating a second time to get angular position  $\theta(t)$ , we have

$$\begin{aligned} \theta(t) &= \int \int h(t) dt \\ &= a_0 t^2 - \frac{1}{(2\pi f_o)^2} \left( \sum_{k=1}^{\infty} \left[ \frac{a_k}{k^2} \cos(2\pi k f_o t) \right] + \sum_{k=1}^{\infty} \left[ \frac{b_k}{k^2} \sin(2\pi k f_o t) \right] \right) + K_1 t + K_2 \end{aligned}$$

Again applying the stance phase initial condition  $\theta(0) = \theta_0$ , we solve for the second integration constant  $K_2$ .

$$K_2 = \frac{1}{(2\pi f_o)^2} \sum_{k=1}^{\infty} \frac{a_k}{k^2} + \theta_0$$

Measurement noise and inadequate frequency resolution may cause the the summation term to be non-zero leading to a larger than expected offset.

We anticipate that the angular position signal  $\theta(t)$ , will also be a complex periodic signal, but in addition to the expected sinusoidal terms the integration of  $\alpha(t)$  has produced three non-periodic terms in  $\theta(t)$ :  $a_0 t^2$ ,  $K_1 t$ , and  $K_2$ .

The  $a_0$  term comes from the DC component of the discrete Fourier transform, so if  $\alpha(t)$  does not have a zero mean over the sample,  $\theta(t)$  will drift quadratically in time. In practical terms, this means that a quadratic propagation of error can be avoided by subtracting the mean of the signal prior to integration.

However, even a zero mean  $\alpha(t)$  signal will have linear drift in  $\theta(t)$  from the  $K_1 t$  term and will be offset due to the constant  $K_2$ . That is, the integration process itself introduces drift into the signal.

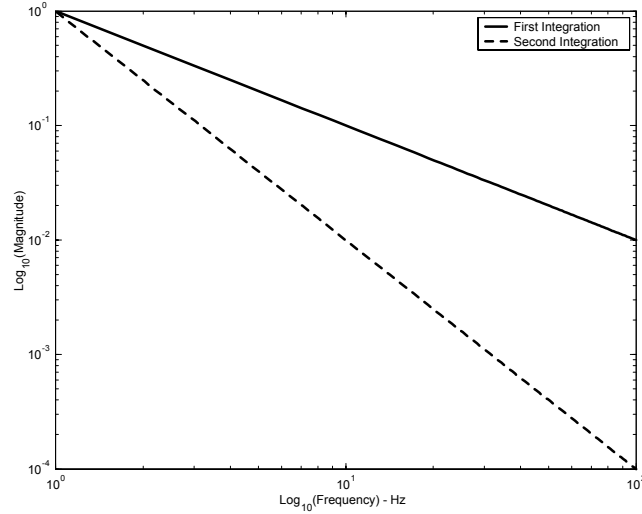


Figure 4.7: Frequency response of single and double integration

#### 4.5.2 Frequency Response of Numerical Integration

Numerical integration in the stride length calculation uses Euler's method which has the form

$$y[n] = y[n-1] + x[n] \Delta t$$

Recognizing this as an infinite impulse response filter, we rearrange the coefficients to separate the recursive and non recursive terms and determine their coefficients:

$$y[n] - y[n-1] = x[n] \Delta t$$

The frequency response of  $H(f)$  of a causal filter with  $N$  recursive coefficients  $a$ , and  $M$  non-recursive coefficients  $b$  is expressed by [30]

$$H(f) = \frac{\sum_{k=0}^M b_k e^{-j2\pi f k}}{\sum_{k=0}^N a_k e^{-j2\pi f k}}$$

So for the Euler integrating filter the frequency response is

$$H(f) = \frac{\Delta t}{1 - e^{-j2\pi f t}}$$

The frequency response of an integrator is shown in Figure 4.7. The frequency response of the second integration is the square of the first order response, and is also plotted.

---

The rapid roll-off of the integration process attenuates higher frequency components, reducing their effect on the integrated signal. Behaving as a low pass filter, the integration process should be insensitive to high frequency noise, but lower frequency disturbances will have substantial effect. This also means that an accurate Fourier series model of  $\theta(t)$  can be constructed from just a few low frequency terms of the sampled angular acceleration signal.

### 4.5.3 Integration Drift

The measured angular acceleration signal shown in the top of Figure 4.6 is shown again in the top of Figure 4.8. Using a discrete Fourier transform to calculate  $a_0$ ,  $a_k$  and  $b_k$ , a Fourier series model of this signal was constructed using only the lowest 8 Hz components of the signal. This model was integrated twice to get the angular velocity and angular position profiles shown in the lower two plots.

To integrate the measured angular acceleration numerically, the mean of  $\alpha(t)$  was subtracted, and the signal was integrated using Euler's method to produce the signal plotted in the middle of Figure 4.8.

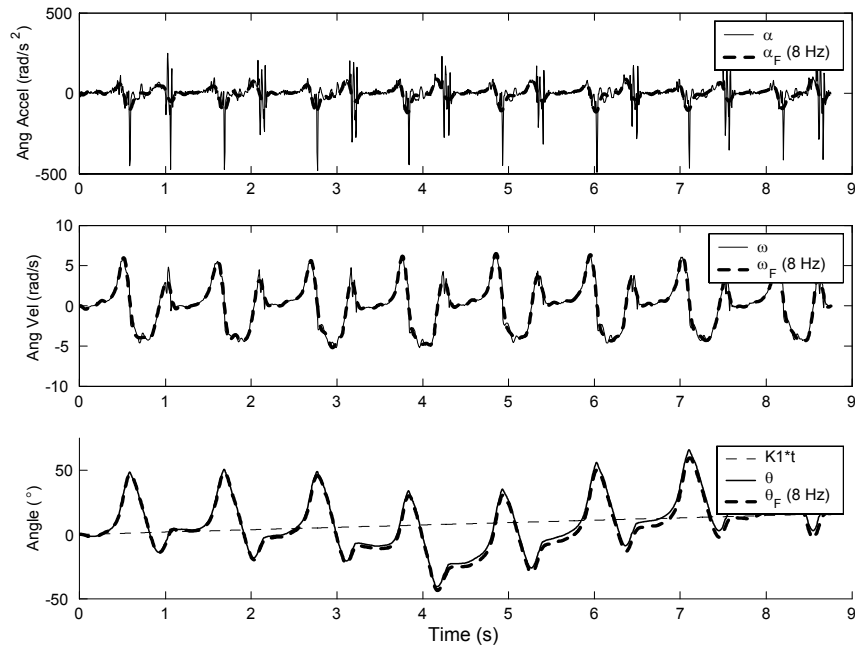


Figure 4.8: Comparison of analytical and numerical integrations of angular acceleration (top) to angular velocity (middle) and angle (bottom)

The lower plot of Figure 4.8 shows nearly exact agreement between the integrated Fourier model and the numerically integrated signal. In this case the mean of  $\omega(t)$  was not removed prior to integration, leading to the rapid linear drift observed. A dotted line representing  $K_1 t$  is plotted to show how the integrated signal behaves consistently with the predicted trend. While the error growth in  $\theta(t)$  is rapid over the five seconds shown, removing the mean of  $\omega(t)$  prior to integration, and integrating over a single stride will reduce the drift observed to acceptable levels as shown in Figure 4.9.

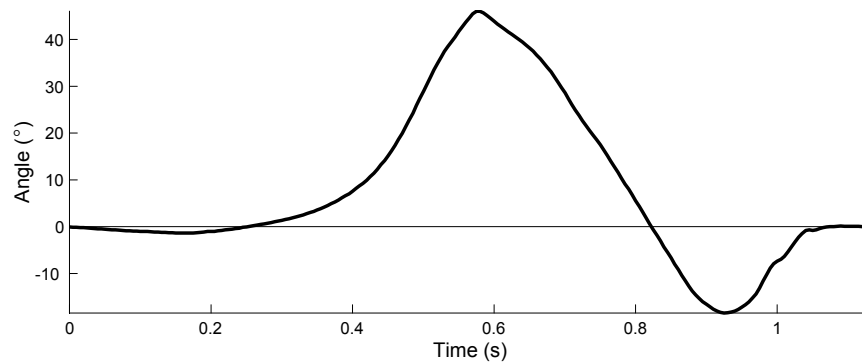


Figure 4.9: Single stride angle profile

## 4.6 Summary

Through understanding of human motion and kinematics, it is possible to measure stride length from foot mounted accelerometers, though consideration must be given to reducing drift that occur when the signals are integrated. With three accelerometers mounted on the foot, the horizontal foot velocity can be measured to calculate the stride length. Two of the accelerometers are parallel and offset, and the difference in the acceleration they measure is used to calculate the angular acceleration over the stride. Temporal integration of this angular acceleration to angular velocity and then angular position allows the sensor orientation to be known through the stride. Knowing the sensor orientation, the horizontal components of acceleration are resolved from two orthogonal accelerometers. To reduce drift in integration process, the mean of each signal over the stride is subtracted prior to integration.

## Chapter 5

# Heading Determination

In this chapter we describe a method of determining the user's direction of travel, which we define as the user's heading in the local horizontal plane. The orientation of Earth's magnetic and gravitational fields with respect to each other is constant regardless of the reference frame from which they are observed. During a stationary period of the user's stride, accelerometers and magneto-resistive sensors are used to measure these fields in the sensor frame, and knowledge of their relative orientation is used to relate the orientation of the sensor frame to the global frame. This relationship is used to calculate the user's heading each stride. Geomagnetic references are used to estimate the local magnetic field direction which is necessary for the magnetic sensors calibration.

### 5.1 Navigation: Relating Reference Frames

Our ultimate goal is to describe the user's location and displacements in a reference frame that relates the user to objects in the surrounding environment. This *global reference frame*  $\mathcal{G}$  is a fixed right handed coordinate system aligned for convenience with the familiar geographic directions East, North and Up as shown in Figure 5.1. The origin of the global reference frame is at an arbitrary, but known position.

The goal of pedestrian navigation is to track the position of the user as he moves without restriction through the global reference frame. The *user reference frame*,  $\mathcal{U}$ , is defined by the user's right hand side ( $x_U$ ), the direction he is facing ( $y_U$ ), and vertical ( $z_U$ ) as shown in Figure 5.1. Through sensor measurements, we must determine the direction the user is facing in the global reference frame. That is we must find the orientation of the user frame  $\mathcal{U}$  with respect to the global reference frame  $\mathcal{G}$ .

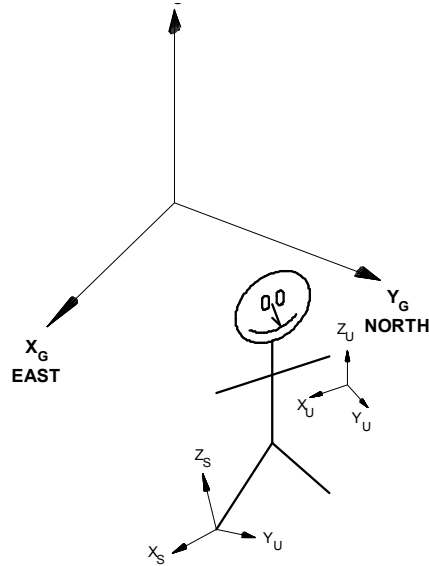


Figure 5.1: Relationship of global, user and sensor reference frames

The output from the sensors measuring the acceleration and magnetic field vectors is given with respect to a third reference frame. The *sensor frame*,  $\mathcal{S}$ , is a right handed coordinate system, subscripted  $S$ , and defined by the directions of positive output from the sensors. Figure 5.1 shows the relationship of these three reference frames. In the case shown, the sensors are mounted on the user's foot.

In sensor based navigation, we attempt to solve the problem of relating the position and orientation of the user in the global frame ( $\mathcal{U}$  to  $\mathcal{G}$ ) by solving the two intermediate orientations relating each to the sensor frame ( $\mathcal{U}$  to  $\mathcal{S}$  and  $\mathcal{S}$  to  $\mathcal{G}$ ). The user's movements cause  $\mathcal{S}$  to translate and rotate with respect to  $\mathcal{G}$ . In practice, the sensors are fixed to the user, meaning that  $\mathcal{U}$  and  $\mathcal{S}$  are coupled but not necessarily aligned and a calibration is required to establish their relative orientation.

### 5.1.1 Subscripts and Notation

The basic problem we are trying to solve is how to use a quantity measured in the sensor frame to determine a heading in the global frame. For the algorithm description which follows, we require a notation that indicates from which reference frame an observation is

being made.

The coordinate matrix  $\mathbf{v}$  that describes some vector  $\vec{v}$ , depends on the reference frame from which the vector is observed. For example, if  $\vec{v}$  is observed in  $\mathcal{G}$  it will be written as the coordinate matrix  $\mathbf{v}_G$ , while the same vector observed in the sensor frame  $\mathcal{S}$  has the coordinate matrix  $\mathbf{v}_S$ .

This method of heading determination also makes use of coordinate transformations and vector rotation operations, usually described as a single rotation of angle, about an axis defined by a vector. Mathematically, there are many ways to perform this coordinate transformation, including Euler angle rotation sequences, axis-angle formulation, and quaternions (see Anton [31] and Kuipers [32]).

However, unless it is necessary to use a specific method, we will simply describe a vector rotation operator by  $R(\textit{axis}, \textit{angle})$ . It is important that the reference frame is consistent for the vector and axis of rotation. For example, to create a new vector  $\vec{u}$  by rotating  $\vec{v}$  by angle  $\theta$  about axis  $\vec{w}$  we would write

$$\vec{u} = R(\vec{w}, \theta)\vec{v}$$

In the sensor frame  $\mathcal{S}$  this would be

$$\mathbf{u}_S = R(\mathbf{w}_S, \theta)\mathbf{v}_S$$

### 5.1.2 Gravity

In the global reference frame  $\mathcal{G}$ , Earth's gravitational field points directly down, perpendicular to the local tangent plane of the Earth's equipotential surface. The magnitude will vary locally but is approximately  $9.81 \text{ m/s}^2$ , or in gravitational units  $1 \text{ g}$ . Following the accelerometer sign convention that gravitational acceleration is observed as an upward acceleration, the unit vector in the direction of gravity  $\vec{g}$ , as observed from the global reference frame is aligned with the global vertical axis is

$$\mathbf{g}_G = [0\mathbf{i}, 0\mathbf{j}, 1\mathbf{k}]$$

The sensor frame observation of the gravity vector  $\mathbf{g}_S$  immediately yields the sensor frame representation of the vertical axis of the global frame. It is important to stress that the sensor frame must be stationary for the gravity observation to be possible with accelerometers.

### 5.1.3 Magnetic Field

Magneto-resistive sensors are used to measure Earth's magnetic field, which has a varying intensity and direction depending where the user is located on the earth. The magnitude of the magnetic field is of interest so we define a unit vector  $\vec{h}$  in the direction of the field. The component of  $\vec{h}$  that lies in the global horizontal plane will point to magnetic North. *Declination* is the angle between magnetic and geographic North in the horizontal plane. *Inclination* is the angle  $\vec{h}$  makes with the global horizontal plane. The declination and inclination may not be known in the global frame but it is sufficiently constant for the current application.

## 5.2 Algorithm

To calculate the user heading, we measure the gravitational and magnetic field vectors in the sensor frame and then apply knowledge of their orientation in the global frame to create a means of relating the sensor frame to the global reference frame. The objective of this algorithm is to construct a direction cosine matrix  $A_S^G$  such that a vector  $\vec{d}$  expressed as  $\mathbf{d}_S$  in the sensor frame can be described in the global frame.

$$\mathbf{d}_G = A_S^G \mathbf{d}_S$$

The sensor frame gravity measurement represents the vertical axis of the global reference frame. Sensor frame representations of magnetic East and North are obtained by projection of the magnetic field observation onto the plane perpendicular to gravity. The coordinate matrices describing magnetic East, magnetic North and vertical are used to construct the direction cosine matrix. A final rotation in the horizontal plane is required to correct for declination and misalignment between the sensor and user frames.

### 5.2.1 Direction Cosine Matrix Construction

Figure 5.2 shows the gravity and magnetic field vectors ( $\vec{g}$  and  $\vec{h}$ ) in the global frame

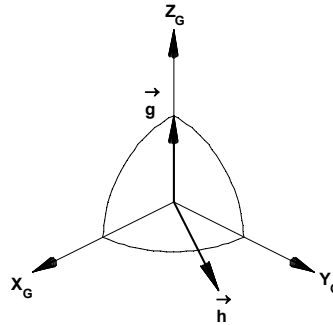


Figure 5.2: Gravitational and magnetic field vectors in the global frame

The gravity vector  $\vec{g}$  points upward along the global vertical axis  $\mathbf{z}_G$ , and the magnetic field vector  $\vec{h}$  points to magnetic north. Over relatively small geographic distances and relatively short periods of time,  $\vec{g}$  and  $\vec{h}$  are invariant. This means that within an area of a few kilometres, over a period of a few hours, the relationship between  $\vec{g}$  and  $\vec{h}$  does not change. By measuring these invariant vectors in the sensor frame, we begin the task of relating the user frame to the global frame.

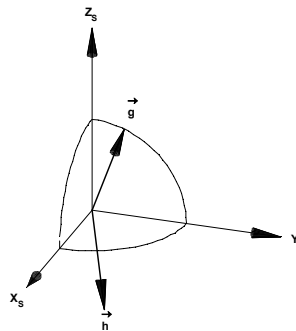


Figure 5.3: Gravitational and magnetic field vectors in the sensor frame

The same gravitational and magnetic field vectors are shown in Figure 5.3, but observed in the sensor frame. To construct the direction cosine matrix  $A_S^G$ , we must find the sensor frame representation of all three axes of the global frame. Since the sensor frame coordinate matrix  $\mathbf{g}_s$  points in the direction of the global frame vertical axis, one axis is already found.

The next axis we find is magnetic East, which lies in the global horizontal plane perpendicular to magnetic field vector. Since  $\vec{e}$  is perpendicular to both  $\vec{g}$  and  $\vec{h}$ , we find it by taking the cross product of  $\vec{h}$  and  $\vec{g}$  and normalizing it. Regardless of the inclination and declination of the magnetic field, by the right hand rule,  $\vec{h} \times \vec{g}$  will point toward magnetic East as shown in Figure 5.4. This step is expressed in the sensor frame as

$$\mathbf{e}_S = \frac{\mathbf{h}_S \times \mathbf{g}_S}{\|\mathbf{h}_S \times \mathbf{g}_S\|}$$

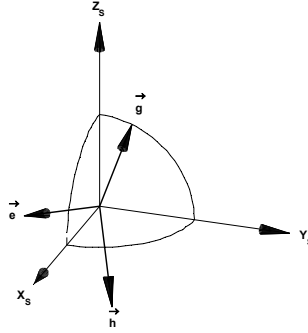


Figure 5.4: Magnetic East  $\vec{e}$  is perpendicular to both gravity  $\vec{g}$ , and magnetic field  $\vec{h}$ .

Last, we need to find magnetic North  $\vec{n}$ , which is the component of  $\vec{h}$  lying in the horizontal plane. (That is, perpendicular to  $\vec{g}$ ) The component of  $\vec{h}$  *parallel* to  $\vec{g}$  found by projecting  $\vec{h}$  onto  $\vec{g}$  by scalar projection.

$$\vec{h}_{\parallel} = \frac{\vec{h} \cdot \vec{g}}{\|\vec{h}\|^2} \vec{g}$$

Since  $\vec{h}$  and  $\vec{g}$  are unit vectors,  $\|\vec{h}\|^2 = 1$ , so

$$\vec{h}_{\parallel} = (\vec{h} \cdot \vec{g}) \vec{g}$$

The component of  $\vec{h}$  *perpendicular* to  $\vec{g}$  is then

$$\begin{aligned} \vec{h}_{\perp} &= \vec{h} - \vec{h}_{\parallel} \\ &= \vec{h} - (\vec{h} \cdot \vec{g}) \vec{g} \end{aligned}$$

Expressed in sensor frame measurements

$$\mathbf{h}_{\perp S} = (\mathbf{h}_S - \mathbf{h}_S \cdot \mathbf{g}_S) \mathbf{g}_S$$

$\vec{n}$  is the unit vector in the direction of  $\vec{h}_{\perp}$  so normalizing gives

$$\mathbf{n}_S = \frac{\mathbf{h}_{\perp S}}{\|\mathbf{h}_{\perp S}\|}$$

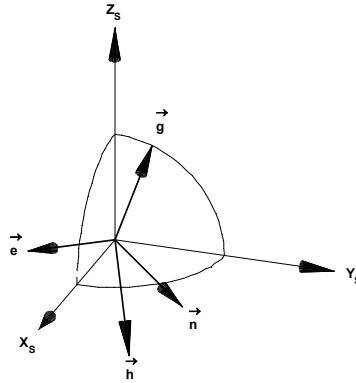


Figure 5.5: Magnetic North,  $\vec{n}$  is perpendicular to  $\vec{g}$  and  $\vec{e}$

Shown in Figure 5.5,  $\vec{n}$  is orthogonal to  $\vec{e}$  and  $\vec{g}$ . Using vector rotation,  $\vec{n}$  may be found alternatively by rotating  $\vec{e}$  about  $\vec{g}$  by  $\frac{\pi}{2}$

$$\mathbf{n}_S = R\left(\mathbf{g}_S, \frac{\pi}{2}\right) \mathbf{e}_S$$

Both methods of calculating  $\mathbf{n}_S$  require approximately equal computational effort.

Now we have three sensor frame coordinate matrices that define a right handed coordinate system: magnetic East  $\mathbf{e}_S$ , magnetic North  $\mathbf{n}_S$ , and gravity  $\mathbf{g}_S$ . Because  $\mathbf{e}_S$  and  $\mathbf{n}_S$  are defined by the magnetic rather than geographic directions, they should be rotated about  $\vec{g}$  to remove the declination angle. For calibration reasons that will be explained, we will leave the declination correction until a later step. The direction cosine matrix  $A_S^G$  relating the sensor frame to the global frame is assembled from the sensor frame coordinate matrices of magnetic East, magnetic North, and gravity as:

$$A_S^G = [\mathbf{e}_S, \mathbf{n}_S, \mathbf{g}_S]^T$$

Again, because  $A_S^G$  is defined using magnetic East and North, it does not transform coordinates from the sensor frame exactly into the global reference frame but we will correct the declination error later.

### 5.2.2 Sensor Frame Heading

The user's heading is the direction the user frame is pointing in the horizontal plane. Though  $\mathbf{h}_S$  rotates around  $\mathbf{g}_S$  in  $\mathcal{S}$ , as the user makes a turn, the relative orientation of  $\mathbf{h}_G$  and  $\mathbf{g}_G$  does not change. A vector is required that has a constant definition in  $\mathcal{S}$ , so that it will rotate in  $\mathcal{G}$  to indicate the user heading.

We create a vector  $\vec{c}$  that lies in the horizontal plane, and has an invariant orientation with respect to  $\vec{g}$  in  $\mathcal{S}$ . Thus, as  $\mathbf{h}_S$  rotates around  $\mathbf{g}_S$ ,  $\mathbf{c}_G$  will rotate in the global horizontal plane around  $\mathbf{g}_G$ . The vector  $\vec{c}$  is constructed using the vector product of the gravity vector  $\vec{g}$  and an arbitrary vector  $\vec{a}$  in  $\mathcal{S}$ . ( $\vec{a}$  is defined such that  $\mathbf{a}_S$  is constant e.g.  $\mathbf{a}_S = [1, 0, 0]$ )

$$\vec{c} = \frac{\vec{g} \times \vec{a}}{\|\vec{g} \times \vec{a}\|} \quad (5.1)$$

Again, because  $\vec{c}$  is perpendicular to  $\vec{g}$ , it must lie in the horizontal plane, and because  $\vec{a}$  is invariant in  $\mathcal{S}$ ,  $\mathbf{c}_G$  will rotate as the user's motion causes  $\mathcal{S}$  to rotate with respect to  $\mathcal{G}$ .

$$\begin{aligned} \mathbf{c}_G &= A_S^G \mathbf{c}_S \\ &= [\mathbf{e}_S, \mathbf{n}_S, \mathbf{g}_S]^T \mathbf{c}_S \end{aligned}$$

The coordinate matrix  $\mathbf{c}_G$  represents the user's heading in the global frame. Note that if  $\vec{g}$  happens to be parallel to this arbitrary vector, the cross product will be zero, and the heading algorithm will fail. This is avoided by error checking, and choosing a coordinate matrix  $\mathbf{a}_S$  that is unlikely to be parallel to  $\mathbf{g}_S$ .

### 5.2.3 Declination and Misalignment Correction

As mentioned, because of magnetic declination and the unknown horizontal alignment between  $\mathcal{S}$  and  $\mathcal{U}$ ,  $\mathbf{c}_G$  will not point in the correct direction.

The last step in the heading determination algorithm is to correct this heading error by rotating  $\mathbf{c}_G$  in the horizontal plane by an angle  $\phi$  to get the true heading  $\mathbf{d}_G$ .

$$\mathbf{d}_G = R(\mathbf{g}_G, \phi) \mathbf{c}_G$$

Assuming that the correction angle  $\phi$  is known, we now have the user's heading.

The reason this heading correction is left to the last step is that it is simpler to determine  $\phi$  directly from calibration than to explicitly sum the magnetic declination and sensor to user frame misalignment. The magnetic declination for a given latitude and longitude is available from reference tables but may vary locally at the user's position. The sensor frame misalignment is often not known explicitly, and can be difficult to measure. Techniques for determining  $\phi$  through calibration are discussed in the following section

### 5.3 Magneto Resistive Sensor Calibration

We now discuss the calibration of the anisotropic magneto-resistive sensors (AMR's) for direction sensing. The difficulty in using Earth's magnetic field is that it changes globally, locally, and in time. It is also a relatively weak field, that may be easily disturbed by metal objects or electrical activity. Because of differences in local magnetic fields, it is not possible to calibrate the sensors in a laboratory apparatus and then use them elsewhere, so a method of field calibration must be devised.

The calibration methods introduced in the following sections involve the user making a complete horizontal rotation, either by standing in place or walking in a circle. By completing a full turn, the sensors capture the complete range of the horizontal field components, but very little of the vertical field. It is difficult to rotate the sensor in the vertical plane once it is attached to the user so a simple calibration cannot be made. Though we are interested only in the horizontal components of the magnetic field, we must calibrate all three axes since the foot sensor will not be oriented with two axes perfectly horizontal.

This calibration method uses a geomagnetic reference to estimate the magnetic field, allowing an idealization of the sensor output to be predicted so that the sensor gain and bias of each axis can be set to match. If the user is facing a known heading at the start of the spin, it is also possible to measure  $\phi$ , which is necessary for the correction step of the heading calculation.

### 5.4 Ideal Sensor Output

As discussed in the previous section, the calibration of the vertical axis of the AMR's cannot be made using a horizontal spin, but if the magnetic field vector was known, the sensor output for the horizontal spin could be predicted. As explained in Appendix C, a geomagnetic model can be used to estimate the global frame magnetic field vector, for a

position of known latitude, longitude and time. This vector is normalized to give us an approximation  $\tilde{\mathbf{h}}_G$  for the local magnetic unit vector in the global frame. An idealized output signal is created where the output of the sensor is 1 when it is perfectly aligned with the magnetic field and 0 when it is perpendicular.

To predict the ideal sensor frame AMR signals, we must make two assumptions. The first is to arbitrarily assume that the sensor frame  $Y$  axis ( $\mathbf{y}_S = [0, 1, 0]$ ) happens to be horizontally aligned with the magnetic field vector  $\mathbf{h}_S$ . Later this assumption can be corrected. We also assume that the user's calibration turn is perfectly horizontal. That is, we assume that the axis of rotation in the sensor frame is  $\mathbf{g}_S$ , and that  $\mathbf{g}_S$  does not change during the spin.

The calibration method follows a similar development as the heading determination in building a direction cosine matrix relating  $\mathcal{S}$  to  $\mathcal{G}$ . First, the triad of shoe mounted accelerometers measure gravity while the user is stationary to get  $\mathbf{g}_S$ . Since we have assumed that magnetic North is aligned with  $\mathbf{y}_S$ , an initial guess for magnetic East is found using cross products as before.

$$\tilde{\mathbf{e}}_S = \frac{\mathbf{y}_S \times \mathbf{g}_S}{\|\mathbf{y}_S \times \mathbf{g}_S\|}$$

:  $S = 1.0g_S y_S d$  This guess is rotated about  $\mathbf{g}_S$  to approximate magnetic North

$$\tilde{\mathbf{n}}_S = R\left(\mathbf{g}_S, \frac{\pi}{2}\right) \mathbf{e}_S$$

The direction cosine matrix that transforms  $\tilde{\mathbf{h}}_G$  into  $\tilde{\mathbf{h}}_S$  is constructed from our measured gravity, and assumed axes.

$$\tilde{A}_S^G = [\tilde{\mathbf{e}}_S, \tilde{\mathbf{n}}_S, \mathbf{g}_S]^T$$

Since it is unlikely that the sensor  $Y$  axis actually aligns with  $\mathbf{h}_S$  in the horizontal plane, the direction cosine matrix  $\tilde{A}_S^G$  will be misaligned in the horizontal plane. However, using  $\tilde{A}_S^G$  to transform  $\tilde{\mathbf{h}}_G$  into the sensor frame, we can predict the mean value and amplitude of the compass signal as the sensor frame is rotated through  $2\pi$ , about the vertical axis. The sensor frame representation of  $\tilde{\mathbf{h}}_G$  is

$$\tilde{\mathbf{h}}_S = \tilde{A}^T \tilde{\mathbf{h}}_G$$

Which we rotate by increments about  $\mathbf{g}_S$

$$\tilde{\mathbf{h}}_S(\theta) = R(\mathbf{g}_S, \theta) \tilde{A} \tilde{\mathbf{h}}_G$$

Though out of phase with the measured signal, the three components of  $\tilde{\mathbf{h}}_S(\theta)$  generate signals with the same mean and range, allowing the sensitivity and gain to be calculated.

#### 5.4.1 Example

The latitude and longitude of Victoria, B.C, where the field trials were located, is  $48.4167N, 123.3667W$ . The altitude is 5 m. The IGRF2000 magnetic field model predicts that on February 11, 2003  $\vec{H}$  will be  $[6158, 17987, 51780]^T$  nT (see Appendix C).

$$\tilde{\mathbf{h}}_G = \frac{\vec{H}}{\|\vec{H}\|} = \frac{[6158, 17987, -51780]^T \text{ nT}}{55160 \text{ nT}} = [0.112, 0.326, -0.939]^T$$

The average accelerometer measurement of the gravity vector in  $\mathcal{S}$  during the spin is:

$$\mathbf{g}_S = [0.150, -0.691, 0.707]$$

The ideal output from the sensors is shown in Figure 5.6

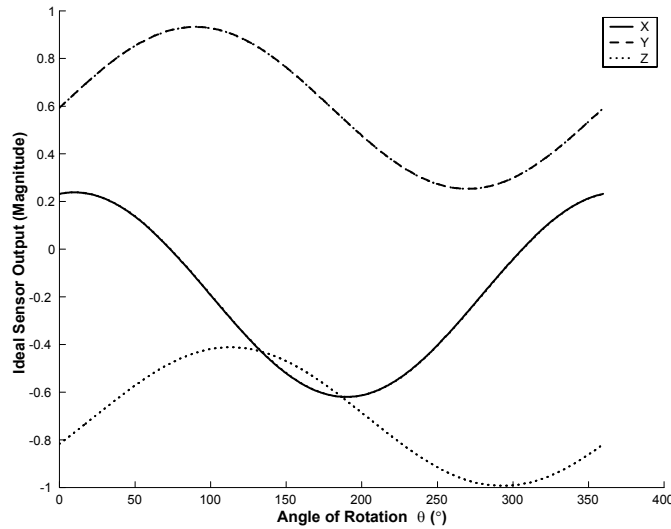


Figure 5.6: Ideal AMR output for  $2\pi$  rotation about  $\vec{g}$

Again, to create this ideal signal we have assumed that the sensor frame  $Y$  axis is aligned with magnetic North, that the axis of rotation is perfectly vertical and that the rotation happens at a constant rate.

## 5.5 Spin Calibration

A popular calibration for torso mounted pedestrian navigation has the user make a complete turn on the spot. This seemed like a logical place to start, so the first calibration method has the user start from a known heading, and turn counterclockwise completely, then back again clockwise. Throughout the spin, the heel of the instrumented shoe is planted to maintain the sensor orientation through the turn. The uncalibrated voltage signal from a triad of shoe mounted magneto-resistive sensors during a stationary turn is shown in Figure 5.7.

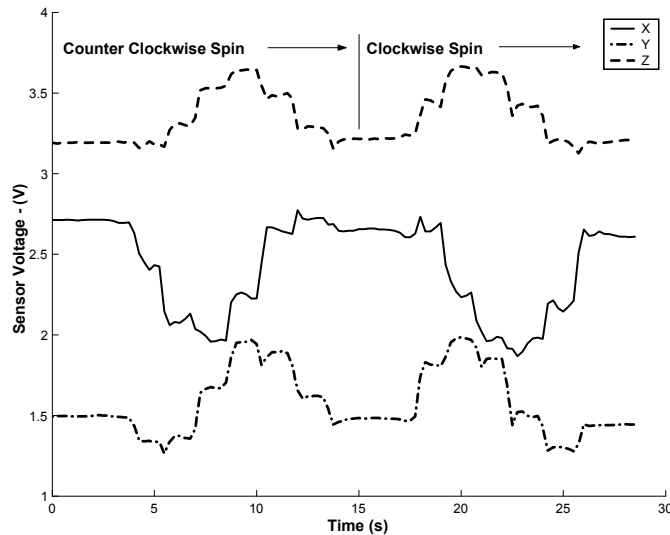


Figure 5.7: AMR sensor signals for stationary spin

A slow, controlled spin with the left heel planted requires approximately five strides with the right foot. Though the user attempts to maintain a constant rate of rotation through the spin, each time the right foot is lifted the shoe rotation is momentarily interrupted, leaving the flat spots observed in Figure 5.7. Though vaguely sinusoidal, the segmentation of the signal will make it difficult to calibrate.

Accelerometer output from the entire spin is averaged to calculate the gravity observation with which we predict the ideal sensor output. Matching the mean and amplitude of the sensor output to the ideal signal, the gain and bias of each sensor is calculated. Figure 5.8 shows the calibrated sensor output plotted with the ideal output.

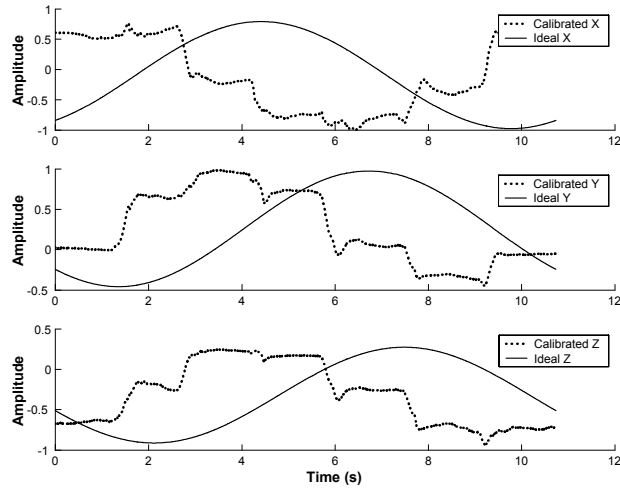


Figure 5.8: Spin calibration: Sensor output matched to ideal signal

The curves are out of phase because of the assumption we made that the sensor frame happened to be aligned with magnetic north. The phase angle between these curves is the effective declination angle  $\phi$  that relates the sensor output to magnetic north. If the initial heading is known, the effective declination can be determined by averaging between the three sensor axes. Figure 5.9 shows the ideal signals with the declination corrected.

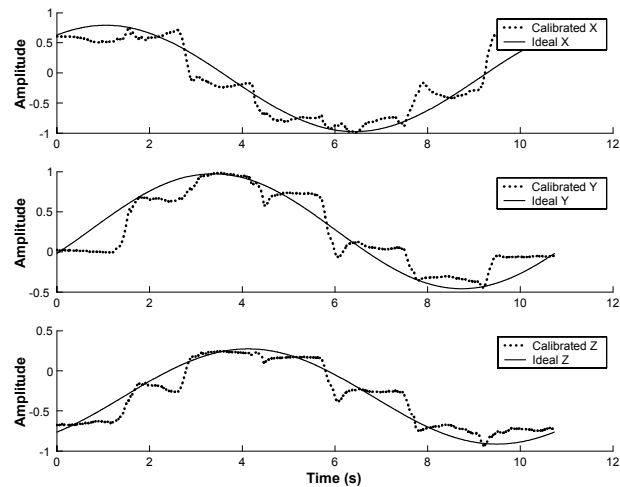


Figure 5.9: Spin calibration: Horizontal alignment corrected

The difficulty in these spot turn calibrations is that it is difficult to have a constant rotation speed during the spin. The sensor curves resemble sinusoids, but have flat parts and variations due to user motion.

## 5.6 Circle Walk Calibration

To calibrate the compasses in the pedestrian mode, the user walks around a circle of 4 m radius, creating the AMR signal shown in Figure 5.10. In this figure, the change in output due to heading cannot be easily distinguished from the change in output due to the motion of the foot while the user is walking.

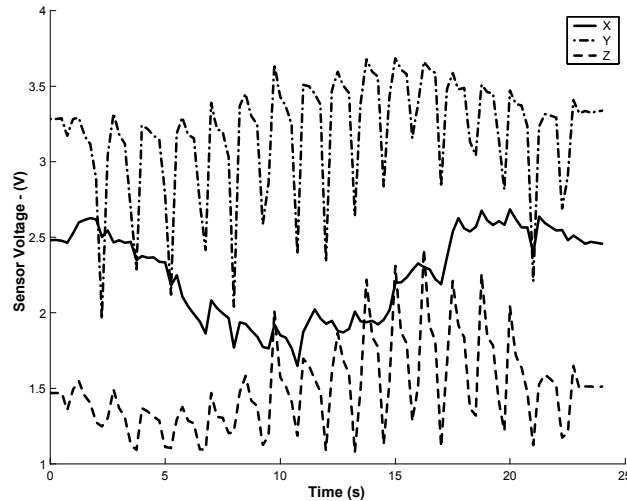


Figure 5.10: Raw AMR output for circle walk calibration

Since the AMR output during the swing phase is of no interest, we apply the gait event detection algorithm to the acceleration signal and keep only the data from the stance phase. Figure 5.11 shows the average stance phase output of the AMR sensors as the user walks around the circle. The change in output due to heading is now clear.

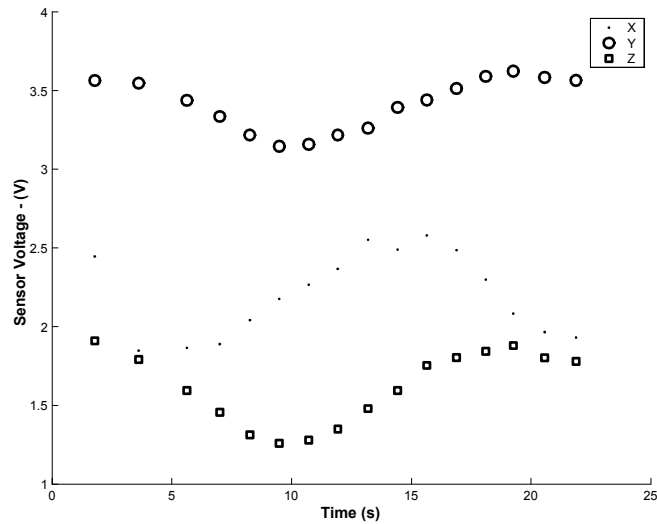


Figure 5.11: Stance phase component of AMR signal during circle walk

Because the user walks around the circle at a nearly constant rate, the output of the sensors is much closer to a proper sinusoid, and thus easier to fit. Figure 5.12 shows the calibrated signals fit the ideal signals better than was possible with the intermittent signals measured in the spin calibration.

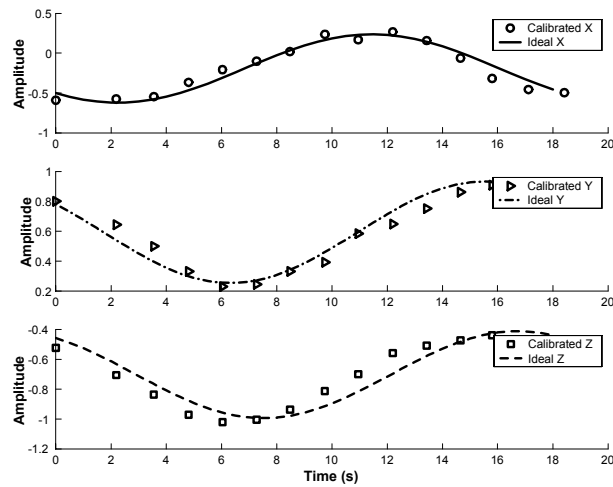


Figure 5.12: Calibrated magneto-resistive sensor signals for circle walk

## 5.7 Summary

A method of heading determination is presented that uses static acceleration and magnetic field measurements to construct a transformation matrix relating sensor frame observations to the global frame. The direction that the user is facing is constant in the sensor frame, and changes in the global frame as the user moves. The transformation matrix constructed in this algorithm is used to express the user's heading in the global frame.

The headings calculated using this method must be corrected for magnetic declination, since the magnetic field is not normally aligned to true North. Also, though the sensor frame and user frame are coupled, they are not necessarily aligned so this must also be accounted for. A calibration method is presented that allows the bias and sensitivity of magneto resistive sensors to be determined and a correction angle to be calculated without requiring explicit knowledge of the declination and sensor to user frame misalignment.

Using geomagnetic references an estimate of the local magnetic field vector can be made, allowing a prediction of what the magneto-resistive sensor output should be under ideal conditions. Matching this ideal signal to the real sensor output voltages, the sensor gain, sensitivity and alignment angle are determined. For shoe based sensors, it was found that having the user walk around a large circle was a better calibration method than spinning around in one spot.

## Chapter 6

# Treadmill Testing

Prior to field trials in an outdoor environment, the method of measuring stride length with shoe mounted accelerometers was tested in the laboratory. These indoor experiments were performed on a treadmill, where the user's gait velocity can be accurately controlled and measured. Comparison of the sensor measurements to the reference positions and angles from the camera provide a means to develop and validate gait event detection and stride length measurement techniques.

### 6.1 Experimental Design

The foot pod was attached to the user's shoe as shown in Figure 6.1. Reflective markers were attached to the shoe to track the position of the toe, heel and ankle. Two markers were also placed on the outside of the pod so that the position and angle of the accelerometers inside could be recorded.



Figure 6.1: Reflective markers on shoe and footpod

Because it was not possible to place the markers directly over the accelerometers, there may be a slight misalignment in static angle, but the pattern of angular change should be identical. The footpod markers are used as the foot angle reference because they are mounted to a solid body and the angle calculated between them will not be corrupted by the flexing of the foot.

In the tests, two subjects walked for thirty seconds at each of three normal walking speeds from 0.7 m/s to 1.3 m/s. When the user had reached the desired speed, a trigger pulse initiated simultaneous recording by the cameras and sensors. Although the basic frequency content of the human gait is below 20 Hz, a sampling rate of 200 Hz was used to ensure that gait events could be resolved precisely.

It was originally intended to confirm the method of heading determination during these tests, but the magnetic field disturbances from the treadmill motor and frame mad this impractical. This confirmation was left for the field trials.

## 6.2 Video Data

### 6.2.1 Foot Position

Figure 6.2 shows the ankle marker trajectory measured using the infrared camera system of a subject walking on a treadmill at 1.3 m/s. With the user walking toward the right side of the plot, the ankle travels in a clockwise direction as shown by the arrows. The time elapsed between each dot is 5 ms, so the spacing between dots graphically illustrates the relative speed of the foot through the gait.

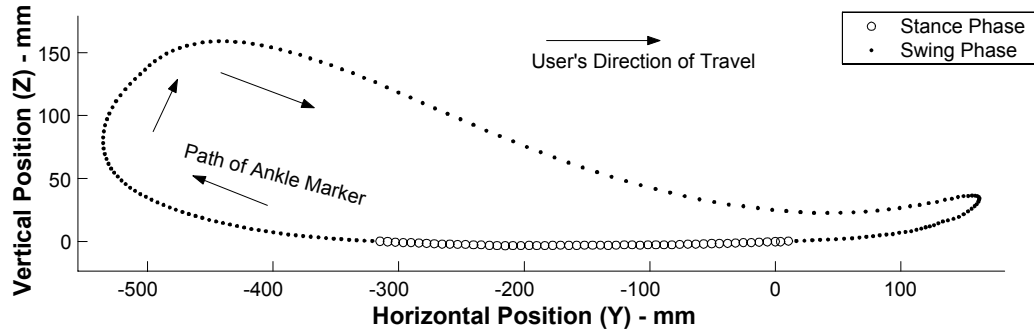


Figure 6.2: Ankle trajectory at 1.3 m/s treadmill speed

Stance phase can be identified from the ankle marker data using the variance of the vertical position and is shown with larger dots in the figure. Synchronization of the camera and sensor recordings make it possible to compare the foot pod measurements to the position reference through each stride. Numerical differentiation of this data, followed by low pass filtering yields the horizontal and vertical velocity profiles that we will use as reference for the sensors.

### 6.2.2 Foot Pod Angle

The angle between the two markers on the foot pod is plotted in Figure 6.3 for the same stride shown in Figure 6.2.

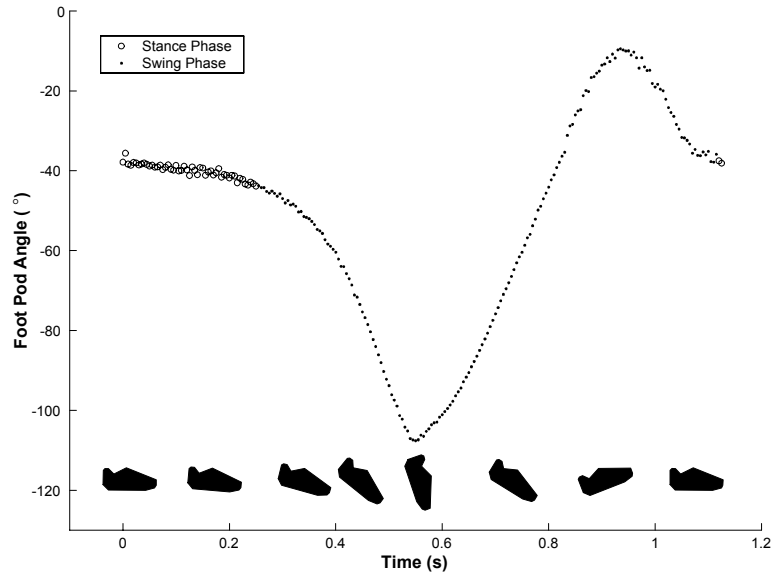


Figure 6.3: Foot pod angle profile at 1.3 m/s treadmill speed

To make the plot more intuitive, shoe symbols showing the progression of the foot are plotted along the bottom. Stance phase is again shown with larger markers and it is apparent from the plot and illustrations that during stance phase the foot is gently rotating forward. To further visualize the rotation of the foot through the gait cycle, the same shoe symbols are placed on the ankle trajectory as shown in Figure 6.4.

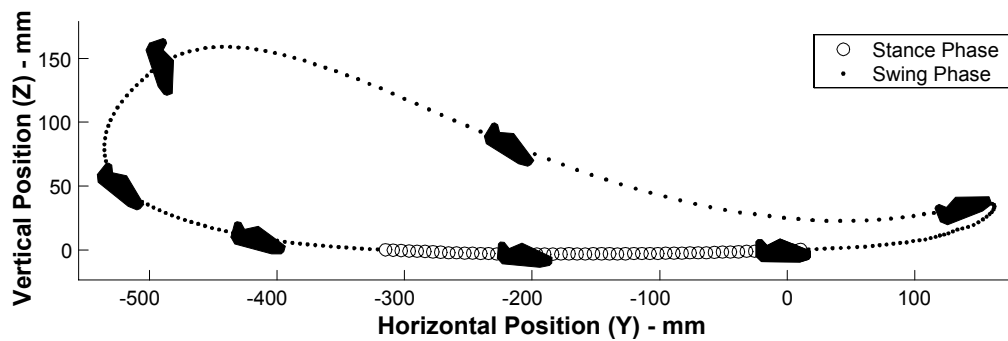


Figure 6.4: Ankle marker trajectory with foot pod angle

### 6.3 Accelerometer Data

The accelerations measured from the three sagittal plane sensor axes during this stride are shown in Figure 6.5. From this data we must identify gait events, then determine the foot angle profile and calculate the average horizontal velocity.

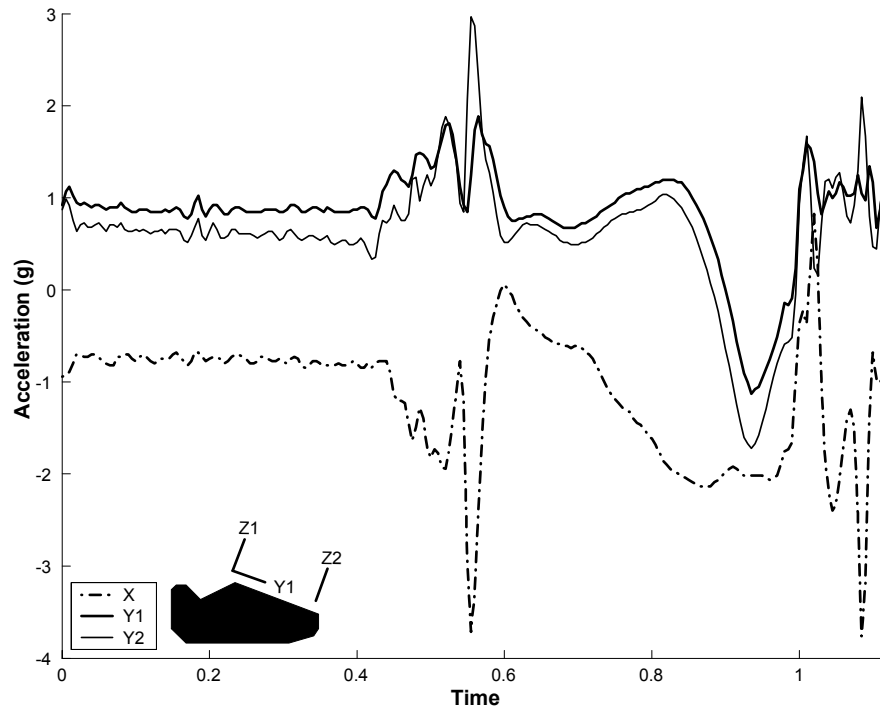


Figure 6.5: Acceleration measured

### 6.4 Gait Event Detection

The acceleration measurements shown in Figure 6.5 are manipulated as described in Chapter 3 to derive the gait event signals shown in Figure 6.6. Symbols indicate the location of events located by the stride detection algorithm. As discussed in the stride detection chapter, we observe a long stationary period ( $A$  to  $B$ ) containing the stance phase, and the more varied period of the swing phase ( $B$  to  $H$ ).

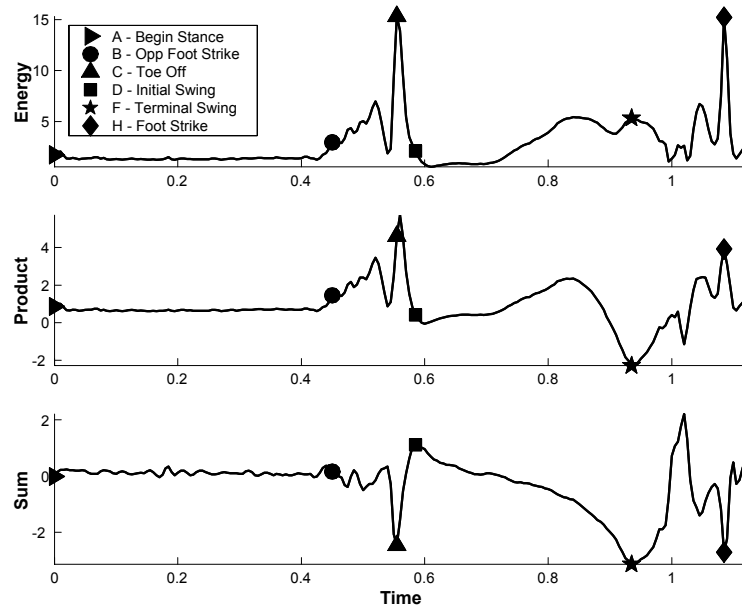


Figure 6.6: Gait Event Signals

In Figure 6.7 the gait events detected using the accelerometers are plotted on the foot pod angle profile measured with the cameras. Here we see that although the gait event signals register almost no change between events *A* and *B* there is significant angular change. The spatial location of the stride events is shown Figure 6.8, by plotting them onto the ankle marker trajectory. Again we see that substantial displacement occurs between the beginning of stance phase (*A*) and opposite foot strike (*B*).

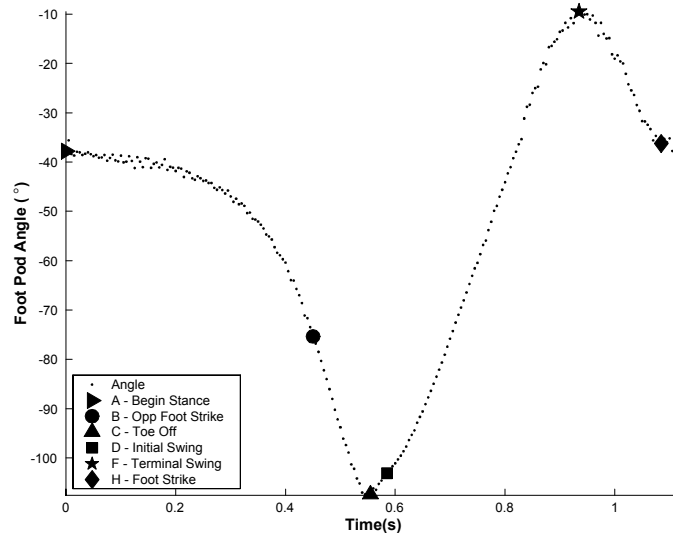


Figure 6.7: Detected gait events plotted on foot pod angle profile.

The stride length measurement and heading determination algorithms both depend on measuring gravitational acceleration during a stationary period, and during the last half of the period  $A - B$  the foot is moving too much. The low dynamics in the early stages of swing phase make it impossible for accelerometers to detect the moment when the opposite foot strikes the ground and the instrumented foot begins to rotate forward toward toe off. Opposite foot strike occurs in the gait cycle approximately half way between initial stance phase and opposite toe off so its occurrence can be approximated by using the middle point of the period  $A - B$ . Shown as even  $J$  in Figure 6.8, it is less desirable to find this event by timing, rather than using a direct signal detection, but this method works consistently over the speeds tested.

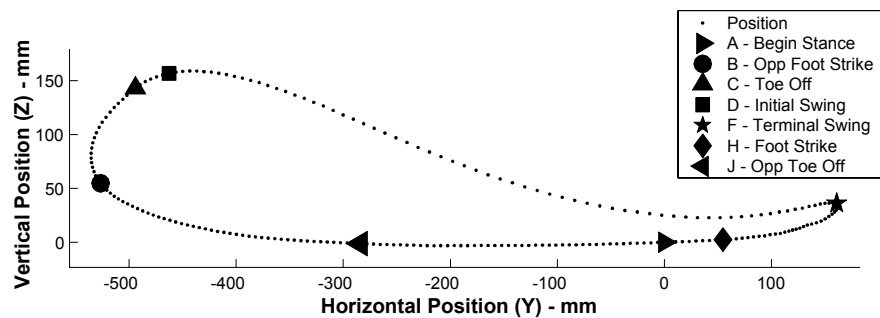


Figure 6.8: Spatial location of Gait Events

## 6.5 Static Foot Angle Measurement

In Chapter 4 we showed that the inclination of a stationary sensor frame can be measured directly from the output of a biaxial accelerometer. Figures 6.3 and 6.7 clearly show that while the foot is not translating during the stance phase, it is slowly rotating. During these tests, the foot is never truly stationary because stance phase occurs on the moving surface of the treadmill. For most of the stance phase the belt is moving at a constant velocity, so the horizontal acceleration is still zero. Figure 6.9 shows the foot angle measured during the stance phase ( $A$ - $B$ ) for three consecutive strides at 1.1 m/s.

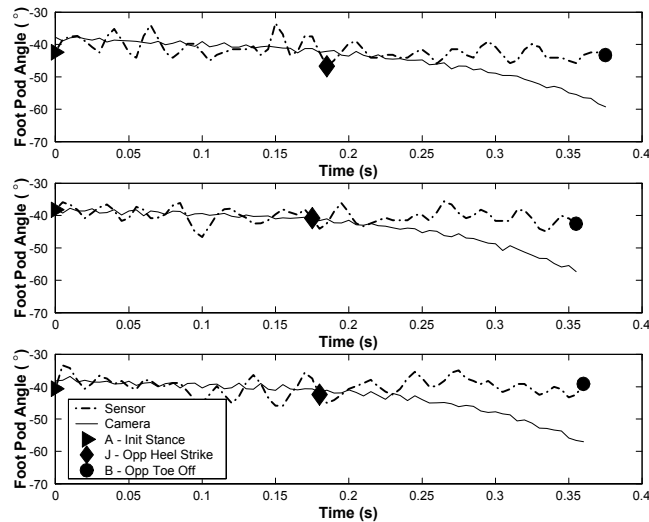


Figure 6.9: Stance phase foot angle profile for three consecutive strides

The small dots indicate the angle calculated directly from the arctangent of the biaxial sensor output. From the start of each plot (Event  $A$ ) until halfway through the period (Event  $J$ , marked with diamond symbol) the calculated angle follows the camera angle. After  $J$  the foot angle begins changing rapidly invalidating the assumption that the foot is stationary. As expected the solution from the sensors diverges. Because of the higher variance of the accelerometer based angle compared to the camera solution, the small angular misalignment between the reference markers and the sensors is not visible. Table 6.1 shows that the average error of the angle calculated at  $J$  is approximately one degree, though the maximum error observed was  $2.7^\circ$ . As the walking speed increases, the variance of the calculated foot angle between  $A$  and  $J$  increases, as does the variance of the error observed at  $J$ .

Table 6.1: Point J Foot Angle Error (m/s )

Speed	Mean Error	Std
0.7	0.7°	1.5°
1.1	-0.5°	1.2°
1.3	-1.2°	1.8°

Figure 6.10 shows the pattern of error growth for the three speeds tested. Each curve represents the average stance phase angle error for a 30 second period. Over the speed range tested it appears that calculating the foot pod angle by inclinometry is valid during the early part of stance phase.

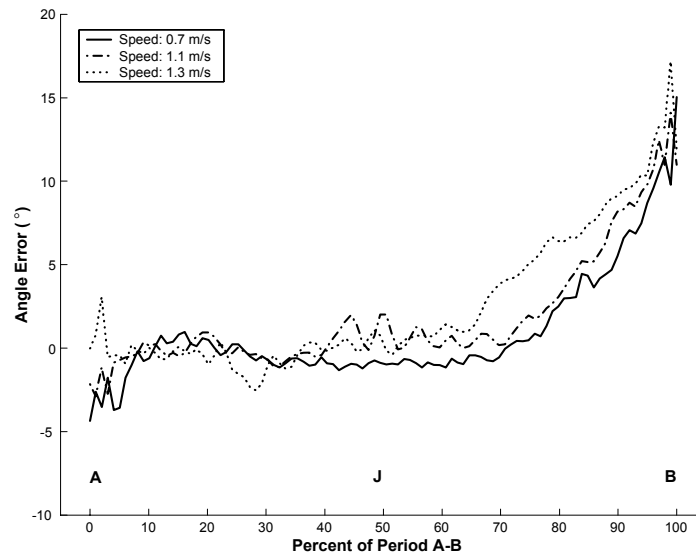


Figure 6.10: Error of static foot angle calculation

## 6.6 Dynamic Foot Angle Measurement

Having established a static foot angle during stance phase, we can use it as an initial value for the integration of the measured angular acceleration. Figure 6.11 shows the foot angle profile calculated in three consecutive strides at 1.1 m/s. Qualitatively, we observe that the sensor solution generally follows the reference foot angle profile, except in the middle of the stride at toe off, where it shows large error. Examination of the foot pod angle profile in Figure 6.7 shows that the error observed at toe off occurs when the foot angle

is at a minimum. The direction of angular rotation is reversing at this point creating a high amplitude spike in angular acceleration lasting only a few samples. The true peak amplitude may occur between samples, which will lower its effect in the integration process. High frequency spikes tend to be attenuated by the integration process, which will further reduce the effect.

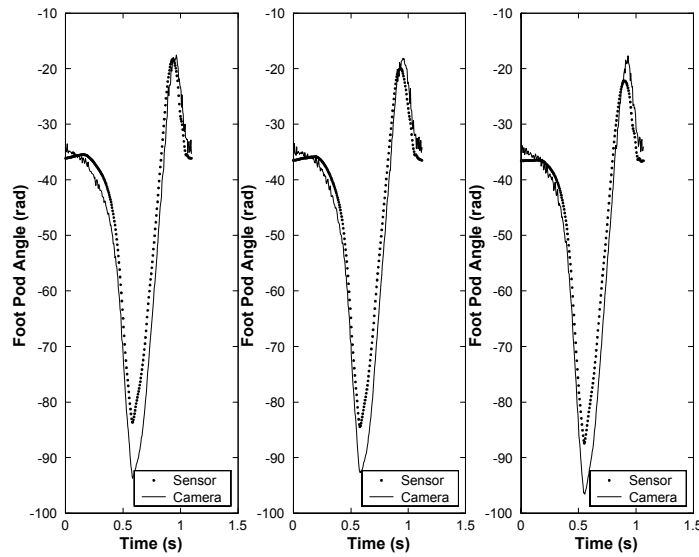


Figure 6.11: Calculated foot angle of three consecutive strides at 1.1 m/s

The error observed during toe off increases with walking speed as shown in Figure 6.12. Each plot in this figure is made by averaging the foot angle profiles calculated from the accelerometers (dotted line) over a 30 second period and is compared to those observed in the same period with the cameras. The abscissa is in percent of stride rather than time to show how the foot angle profile changes with walking speed.

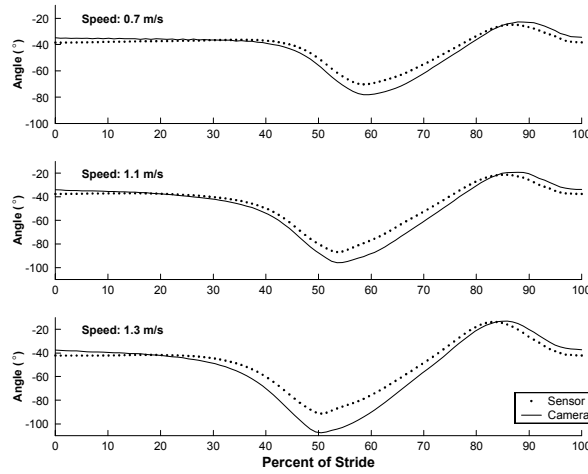


Figure 6.12: Averaged foot pod angle profiles for camera and sensors at varying speeds

By plotting as a percent of stride instead of time we can see the change in relative length of the stance phase from almost 50% at the slower speeds to approximately 30% at the fastest speed. As the speed increases, the peak foot angle occurs earlier in the stride, and shifts the peak of the error profiles shown in Figure 6.13 to the left. At 1.3 m/s a maximum angular error of  $15^\circ$  is observed. Since the foot pod angle is used to resolve horizontal velocity, this substantial error will be passed through all subsequent calculations including the final stride length calculation.

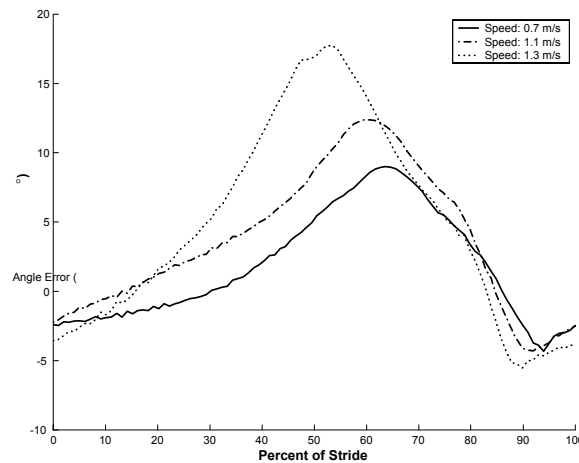


Figure 6.13: Error in dynamic foot angle profile

## 6.7 Foot Velocity Profiles

Reference profiles for the horizontal and vertical of the foot are generated by differentiating the video position data and then smoothing it with a fifth-order lowpass Butterworth filter with a cutoff of 30 Hz. The horizontal and vertical components of the measured acceleration are separated using the foot angle profile as explained in Chapter 5. We are interested in understanding the accuracy of these profiles because the stride length estimation is made by multiplying the stride duration by the mean horizontal velocity.

### 6.7.1 Horizontal Velocity

Figure 6.14 compares the calculated horizontal velocity (shown with dots) to the reference velocity from the camera (shown in solid) for the same three consecutive strides shown in Figure 6.11. Though there is some evidence of error at toe off, it is not nearly as pronounced with the velocity profile as it is with the foot angle profile. During the early part of the stance, integration drift is observed. This occurs during a period when the acceleration is low relative to the sensor noise.

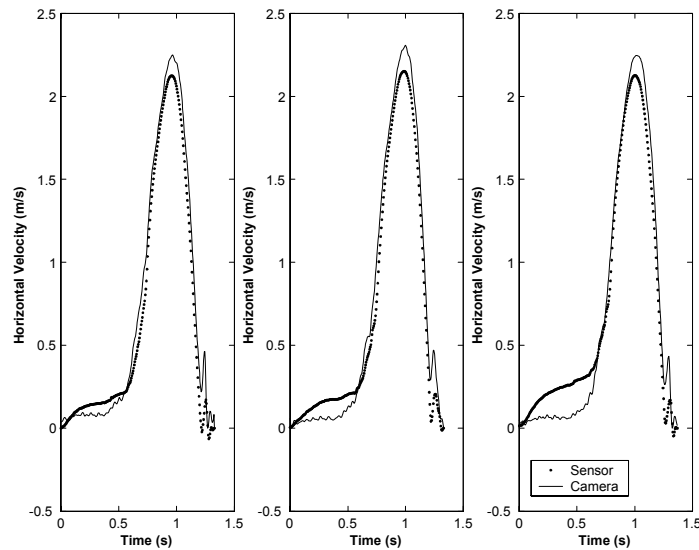


Figure 6.14: Horizontal foot velocity profiles of 3 consecutive strides - 1.1 m/s

In a similar fashion to Figure 6.12, the averaged horizontal velocity profile for each speed is shown plotted as a percentage of stride in Figure 6.15.

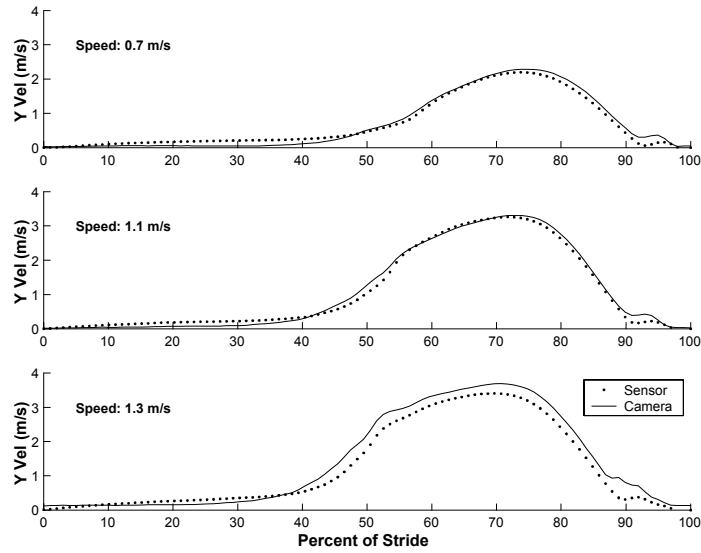


Figure 6.15: Average horizontal velocity at various treadmill speeds

Here we again see close agreement between the camera and sensor profiles. Figure 6.16 shows that the error in velocity has brief peaks corresponding to the peak angular errors in Figure 6.13. Errors of up to 0.5 m/s are observed at the peak, though the error is closer to 0.1 m/s through the remainder of the stride.

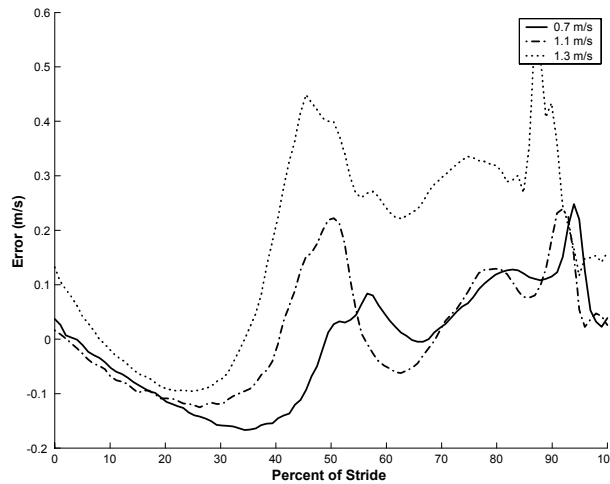


Figure 6.16: Error in horizontal velocity

The mean horizontal velocity of a stride is used to calculate its length. Table 6.2

Table 6.2: Mean Horizontal Velocities (m/s)

Speed	IR Camera	Sensor	Difference
0.7	0.69	0.70	0.01
1.1	1.10	1.09	0.01
1.3	1.39	1.23	0.16

compares the mean horizontal velocities calculated by accelerometry to the mean velocity observed with the cameras. For two of these tests the error was acceptably low - less than 1 cm/s, however at the highest walking speed the discrepancy was 16 cm/s, which would lead to a 16 cm error in a 1 s stride.

### 6.7.2 Vertical Velocity

On a level surface such as the treadmill, the vertical travel of the foot is small relative to the horizontal displacement. Though we expect to see a period of positive vertical velocity as the foot is lifted from the ground and a period of negative velocity while it is placed again on the ground, we also expect that the mean vertical velocity of the stride will be zero since the foot returns to the same height each stride. The vertical velocities observed are approximately a tenth of the horizontal ones as shown in Figure 6.17. Again, during the early part of the stride we see drift accumulating in the integrated velocity.

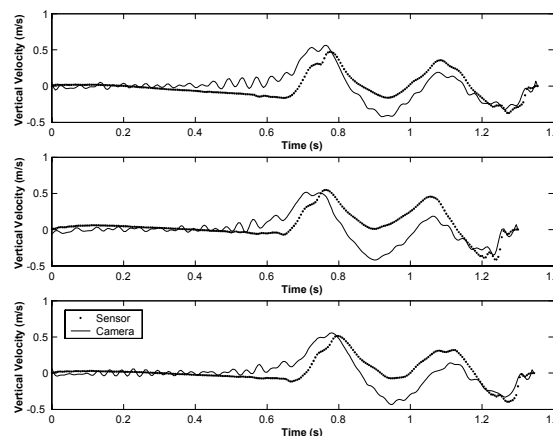


Figure 6.17: Vertical velocity profiles

Figures 6.17 and 6.18 show that over the speeds tested, the vertical velocity profiles have the greater discrepancy with respect to the reference than the horizontal velocity, though the magnitude of the error is comparable.

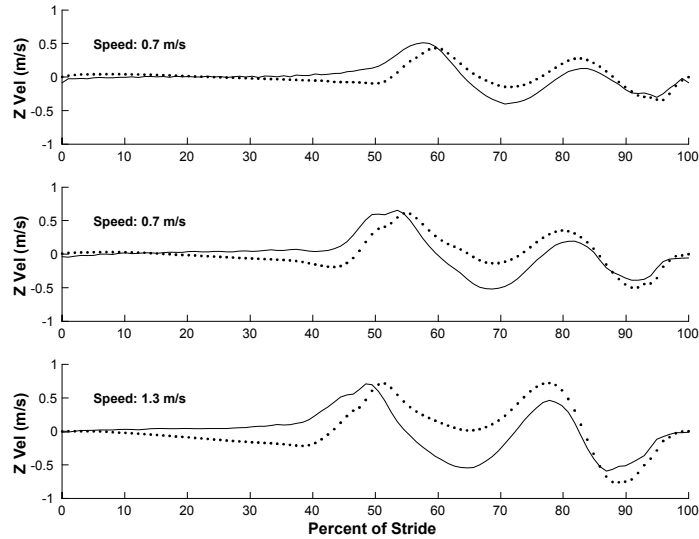


Figure 6.18: Average vertical velocity profiles for various treadmill speeds.

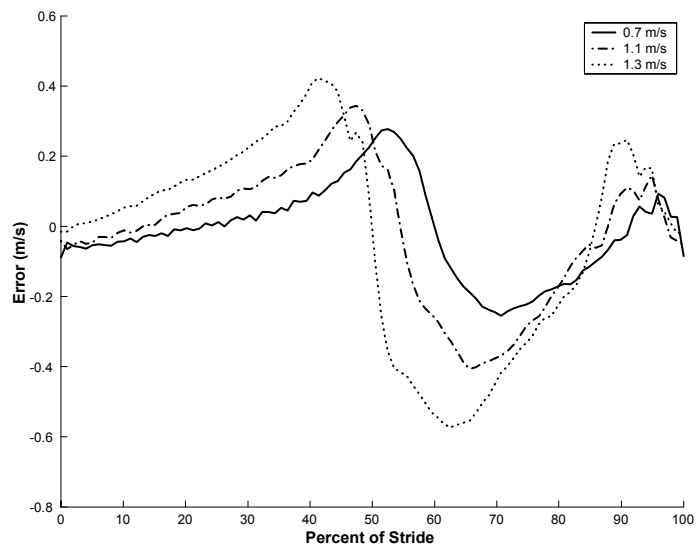


Figure 6.19: Error in vertical velocity

Table 6.3: Vertical Velocity Comparison

Mean Vertical Velocities (m/s)			
Speed	IR Camera	Sensor	Difference
0.7	-0.00	0.01	0.01
1.1	-0.00	0.02	0.02
1.3	-0.00	0.03	0.03

Table 6.4: Stride Length Comparison

Constant Speed	Mean Velocity			Distance		
	Foot Pod	Treadmill	Err	Foot Pod	Treadmill	Err
1.1 m/s	1.05 ± 0.22 m	1.11 ± 0.03 m	5%	31.80 m	32.02 ± 0.15 m	0.7%

The mean vertical stride velocity observed by the cameras and accelerometers are listed in Table 6.3. At all speeds, the mean velocity observed by the cameras is 0 m/s as expected, but the accelerometers show non zero averages of up to 3 cm/s. Relative to the sensitivity of the accelerometers, this is an acceptably small discrepancy, but it indicates that the vertical velocity profile should not be used to measure vertical travel.

## 6.8 Distance Measurements

Having established the accuracy of the mean horizontal stride velocity method through video comparison, the accuracy of the stride length measurement can be examined. Output from an event sensor on the treadmill motor was used to directly measure the belt travel, establishing a reference for the accelerometer measurements.

Table 6.4 compares the velocity and distance measured by accelerometry to the treadmill reference for a short test at a constant speed of 1.1 m/s. There is large variance in the mean stride velocity as expected from the video tests, which accounts for the 5% difference compared to the treadmill. In spite of the relatively high error observed in measuring average stride velocity, the error in the overall distance measured is just 22 cm in 32 m of travel, or 0.7%.

In the final laboratory tests, the user walks at constantly changing treadmill speeds over a 90 s period to approximate unrestricted outdoor motion. Figure 6.20 shows the velocity profile and distance traveled during this test. In the upper plot we see that the

Table 6.5: Stride Length Comparison

Speed	Mean Velocity			Distance		
	Foot Pod	Reference	Err	Foot Pod	Reference	Err
Varied	$0.98 \pm 0.20$ m	$1.05 \pm 0.18$ m	5%	87.0 m	$89.4 \pm 0.15$ m	3%

foot pod velocity tracks but underestimates the treadmill velocity. However, there is still close agreement in distance traveled in the lower plot. As tabulated in Table 6.5, the error accumulated over 90 s is about 2 m or 3%

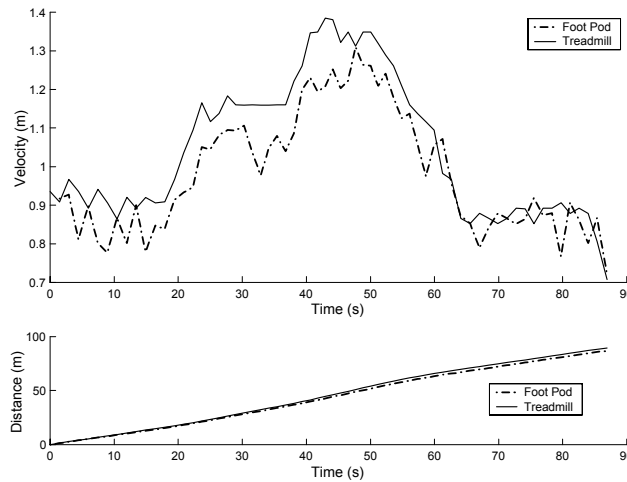


Figure 6.20: Stride velocity and distance measurement comparison

## 6.9 Summary of Treadmill Testing

Comparing the foot pod accelerometer measurements with the infrared camera reference during the treadmill tests allowed a close examination of the performance and error in stride length measurement.

It is possible to reliably identify gait events that have strong signal properties. Opposite foot strike, which occurs during stance phase is not distinguishable by the accelerometers so it is found by interpolating halfway between the detection of initial stance phase and toe off.

The foot angle calculated by inclinometry during the period between initial stance phase and opposite foot strike is accurate to  $1^\circ$  on average, with a  $2.7^\circ$  maximum error

observed. Considering the relative crudeness of this method, its accuracy is surprising.

High angular acceleration during toe off leads to substantial error in the integrated foot pod angle profile. This is propagated into the horizontal and vertical velocity profiles but does not seem to adversely affect the accuracy of the mean horizontal stride velocity. The magnitude of the error in vertical velocity is comparable to that in the horizontal velocity but because of the low vertical velocities that occur during normal walking the relative error was much higher.

Finally, over a longer test of varying speed the calculated stride length was within 3% of the reference distance. While this is not optimal accuracy, the validity of accelerometer based stride length measurement has been satisfactorily established.

## Chapter 7

# Field Testing

Having established the validity and accuracy of methods of gait event identification, stance phase orientation determination and stride length measurement, the shoe mounted pedestrian dead reckoning system was tested on a surveyed trajectory in a dense coniferous forest located in Victoria, B.C. This was an appropriate test environment for evaluation as the thick forest cover attenuates standard GPS signals, and the magnetic field is free of disturbances. In addition to the survey, two other positioning methods were used for comparison: a high sensitivity GPS receiver, and a pedestrian dead reckoning system using torso mounted ring laser gyros.

### 7.1 Experimental Design

The user wore the foot pod on the left shoe, as shown in the left hand photo of Figure 7.1. For reference the user also carried a backpack with multiple SiRF high sensitivity GPS receivers, and a triad of Honeywell GG1308 ring laser gyros used in a HG1700-based Novatel BlackDiamond<sup>TM</sup> GPS/INS system. The system, provided by the University of Calgary, was used in a multi-purpose experiment to test location and navigation under the forest canopy. All postprocessing of the GPS and ring laser gyro data was performed by Jussi Collin and Glenn MacGougan.



Figure 7.1: Field trial equipment: (left) Foot pod on left foot (right) reference equipment

A hand trigger was used to mark important events, allowing the multiple data records to be synchronized. The right hand side of Figure 7.1 shows the reference sensors and equipment.

The test track was a gravel and boardwalk loop approximately 900 metres in length and divided into 13 main sections by surveyed checkpoints as shown in Figure 7.2. Tests began at Station 0, after the user completed both the compass calibration spin and circle walk described in Chapter 5. The user walked at a comfortable pace counterclockwise around the course as shown with arrows in the figure. As indicated with arrows in the figure, the course was mainly flat except for two inclined sections.

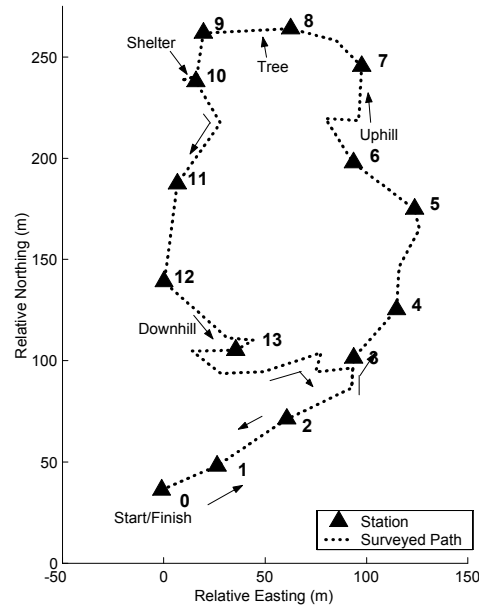


Figure 7.2: Field test course

Two features of the test track, marked on Figure 7.2, were used to highlight performance differences between pedestrian dead reckoning and satellite positioning. The first was a tree located between station 8 and 9 that the user walked tightly around. The second was a wooden shelter located just before station 10 which the user entered and remained stationary inside for approximately 30 seconds before carrying on. After returning to station 0, the user repeated the compass calibrations.

The performance of the shoe mounted pedestrian dead reckoning system will be evaluated a number of ways. Since the overall positioning accuracy is of greatest interest, it is considered first in comparison to the reference systems. Error in stride length and heading are then examined. Short term system performance is also examined.

## 7.2 Long Course Trajectories

The trajectory calculated over the entire course is now compared for the references and foot pod.

### 7.2.1 High Sensitivity GPS

Figure 7.3 shows the test trajectory measured by the SiRF high sensitivity receiver. Circles indicate the position calculated by the GPS at the moment when the user passed a control point and pressed the hand trigger. Except for a short period just after station 6 and again between stations 12 and 13, the trajectory follows the surveyed path closely. The areas where the GPS position wanders are most likely due to a brief loss of one satellite signal.

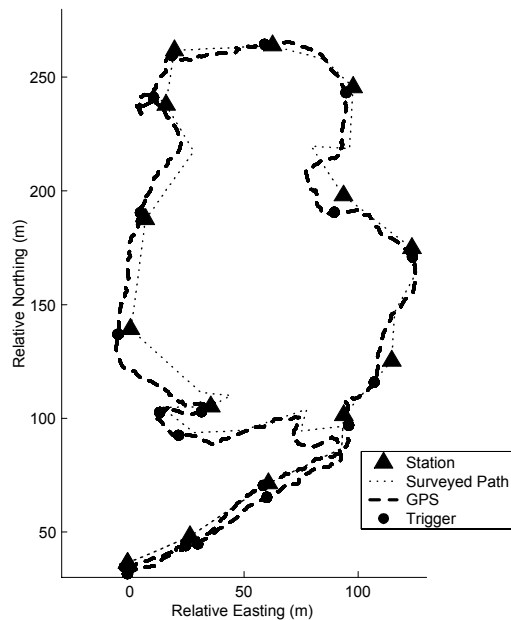


Figure 7.3: Trajectory measured by high sensitivity GPS

The error in position measured at each control point is less than the ten metre accuracy specified by the manufacturer, and the trajectory closes to within 3 m, indicating that even in thick forest, GPS positioning is feasible and accurate.

### 7.2.2 Ring Laser Gyro

To compare the performance of the shoe mounted pedestrian dead reckoning system with more conventional methods, a torso mounted pedestrian navigation system was simulated using a triad of Honeywell ring laser gyros for heading. Stride detection was done using the footpod, but a constant stride length was applied. In the test shown in Figure 7.4,

the path calculated using this method follow the surveyed path closely at first, with a steadily increasing error.

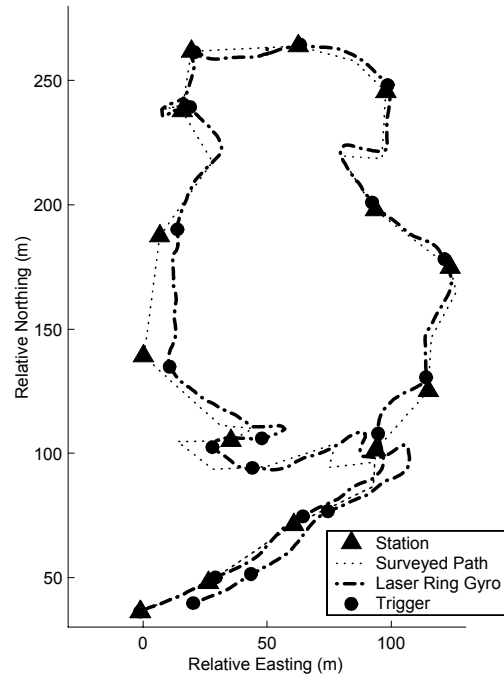


Figure 7.4: Trajectory using torso mounted ring laser gyros and constant steplength

The stride length was chosen by dividing the course length by the number of strides detected, so represents the best estimate of the user's mean stride length. Since the Honeywell gyros have an error of less than 1 degree/hour, this plot accentuates the error in the constant stride length assumption.

### 7.2.3 Foot Pod

Figure 7.5 shows the trajectory measured with the shoe mounted pedestrian dead reckoning system. While the path is recognizable in shape, there is substantial error visible in both the stride length and heading estimations. The overall distance measurement underestimates the surveyed distance by 7%. Since the surveyed distance represents the line of sight distance between stations, it is shorter than the distance actually walked and the foot pod should not be measuring less than this value. The error in position at the end of the test is over 190 m.

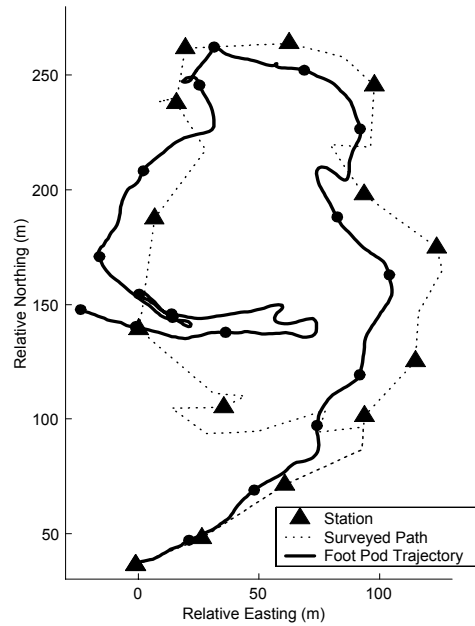


Figure 7.5: Trajectory using shoe mounted sensors

It is clear, without any calculation, that the long track performance of the foot mounted solution is inferior to the existing methods of navigation. However, we will examine the source of these error to see if any improvement can be made.

#### 7.2.4 Position Error

The position error at each control station is compared for all three navigation methods in Figure 7.6. Vertical lines indicate the time that the user pressed the hand trigger. As expected, the error for the high sensitivity GPS is consistently less than 10 m, and shows no dependence on time or stride count.

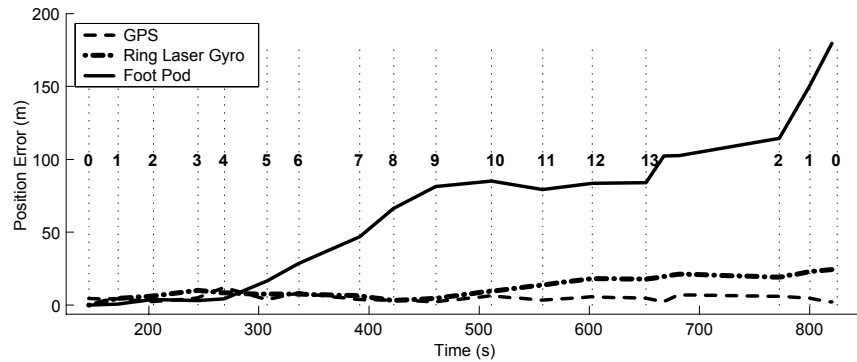


Figure 7.6: Comparison of error in position

The position error for the ring laser gyro slowly increases with the number of steps taken by the user, which is consistent with the pedestrian dead reckoning model. After 641 detected strides, the error in position is 25 m for an average error growth of 4 cm per stride which, as mentioned, will be largely due to the error in the constant stride length assumption. The error in the foot pod solution also appears to behave consistently with the linear error predicted by the pedestrian dead reckoning model but with a substantially greater average error per stride of almost 30 cm.

### 7.2.5 Stride Length Error

Figure 7.7 compares the distance traveled between control points for the entire test. The surveyed distance of 847 m is obtained by summation of the straight distances between control points and will be less than the actual distance travelled because the path sections are not straight between surveyed points. The total distance measured by the GPS is 940 m, which will be more than the distance travelled, because of the occasional solution divergences described earlier.

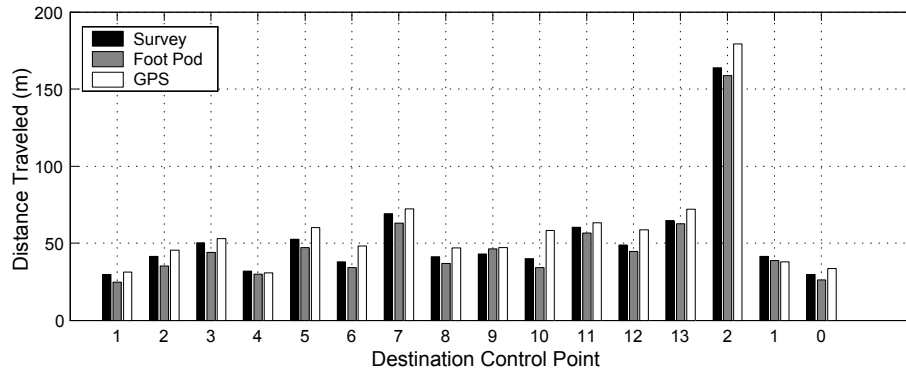


Figure 7.7: Comparison of distance measurements

The distance measured by the foot pod stride length measurement is expected to be between the limits set by the survey and GPS solutions, however as shown in Figure 7.7, it consistently measures approximately 7% less than the distances given by the survey. From the treadmill tests, it was expected that error should be closer to 3%. Since the sensors and algorithm are identical between the field trials and treadmill tests the error is likely to occur because of the difference in test conditions. The treadmill tests did not investigate the system performance on inclined surfaces, but since the underestimation is occurring consistently regardless of grade this error is more indicative of accelerometer calibration error.

### 7.2.6 Heading Error

The top plot in Figure 7.8 shows the heading calculated through the test by the foot pod and ring laser gyro. The difference between them is shown underneath and has a mean value of 17 degrees.

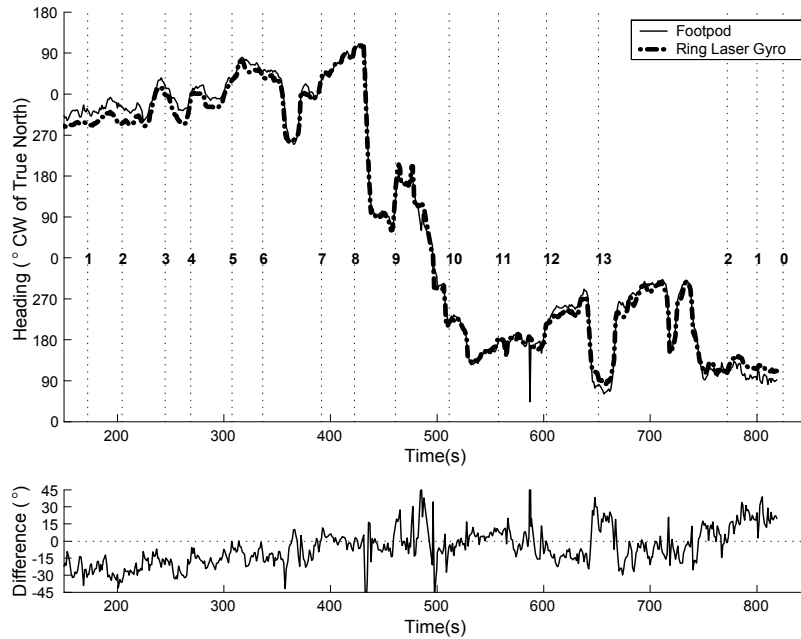


Figure 7.8: Comparison of ring laser gyro and foot pod heading

Inspection of the trajectory in 7.5 shows that the highest error occurs on the hills, particularly in the section close to Station 13. Here we see that the error jumps by almost 40 degrees. The clockwise drift of approximately  $250^\circ/\text{h}$ , and the high error observed on sloped surfaces suggest errors in the sensor calibrations, particularly the vertical compass axis.

### 7.2.7 Calibration Error

As already mentioned in the second chapter, the output from the sensors is ratiometric to the voltage supply, and ambient temperature, but these conditions were not measured on the sensor board during any of the tests. This means that the accelerometer calibrations performed in the lab at  $20^\circ\text{C}$ , will not be valid in the field at  $8^\circ\text{C}$ . As even a 3 mV change in accelerometer sensitivity results in a change of over 50 m in stride length measurement for the test, this is a substantial problem. Error in accelerometer measurements will affect both the stride length measurement and the heading estimation.

By performing the compass calibration at the start and end of the test, it was observed that over relatively short periods of time (15 min) the bias and sensitivity of the magneto-

resistive sensors was observed to change, causing the drift observed in the lower plot of Figure 7.8. From start to finish the compass bias levels were observed to change by as much as 300 mV on a nominal value of 2.5 V. The average of the start and finish values was used.

Though impossible to correct properly afterward, an estimation of the correct accelerometer calibration values can be made by examining their output during the time that the user stands still prior to beginning the test. Since the user is stationary, the accelerometers should be reading gravitational acceleration only (1 g), and the parallel offset accelerometers should measure the same acceleration because the board is not rotating. Instead the accelerometers are measuring almost 2 g acceleration at this point. Experience in calibrating the accelerometers suggests that the bias level is more likely to change than the sensitivity, so for all four accelerometers the bias was adjusted until the accelerometers output made better physical sense during this period. The maximum change required in bias was less than 50 mV, or 2%, of the nominal value of 4.5 V. Using these new estimates, the compass bias and sensitivity could be recalculated as described in Chapter 6. Though only an estimate, these adjustments improve the system performance as presented in the next section.

## 7.3 Performance with bias adjustments

### 7.3.1 Long Course Performance

Figure 7.9 shows the trajectory measured with the foot pod after the bias level adjustment described in the previous section. Though still not comparable to the ring laser gyro in accuracy, the path measurement shows significant improvement.

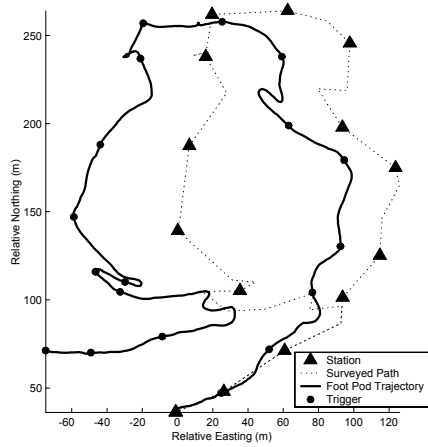


Figure 7.9: Foot pod trajectory after bias level adjustment

### 7.3.2 Position Error

The error in position after this adjustment is now less than 90 m as shown in Figure 7.10.

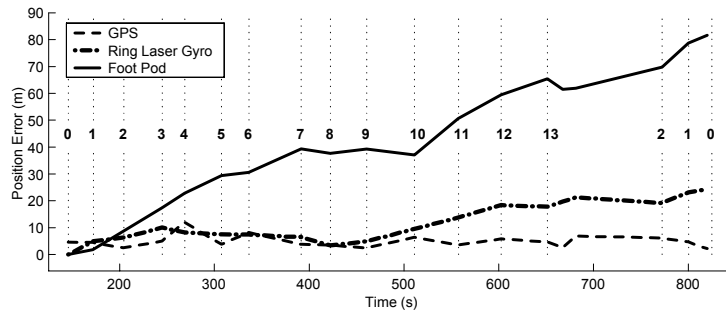


Figure 7.10: Error in position, after bias level adjustment

### 7.3.3 Stride Length Error

Figure 7.11 shows the improvement that the bias adjustment makes to the stride length measurement accuracy. The total length measured with the foot pod is 880m which is within 4% of the surveyed distance and 6% of the distance measured by GPS.

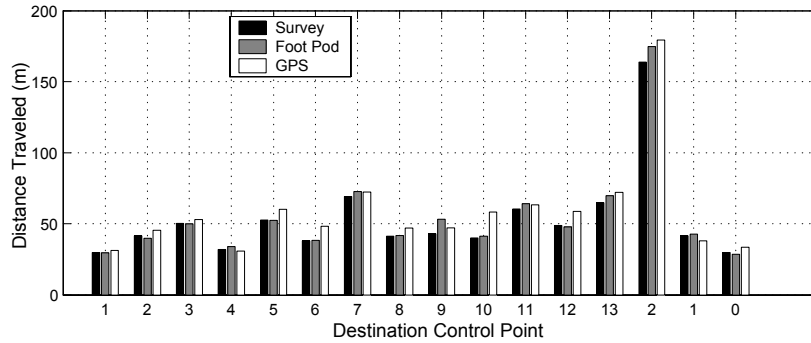


Figure 7.11: Comparison of distance measurements after bias adjustment

For the section ending at Station 9, the foot pod measured a greater distance than either the survey or the GPS, because the extra distance the user walks around the tree.

### 7.3.4 Heading Error

The heading plotted in Figure 7.12 shows that the adjusted foot pod heading has reduced error on the inclined sections compared to Figure 7.8. Over the entire test, the mean heading error is now 4 degrees, though the linear drift is still apparent.

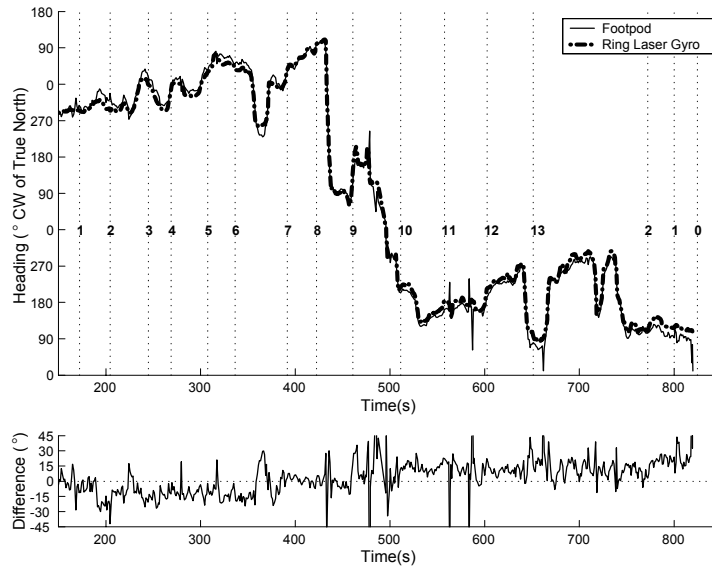


Figure 7.12: Comparison of ring laser gyro and foot pod heading after bias adjustment

## 7.4 Short Term Performance

The relatively large rate of error growth in the foot pod trajectory makes it difficult to see how the system performs over the individual sections of the course, especially later in the test. Figure 7.13 shows the trajectory calculated by the foot pod, corrected at each control station.

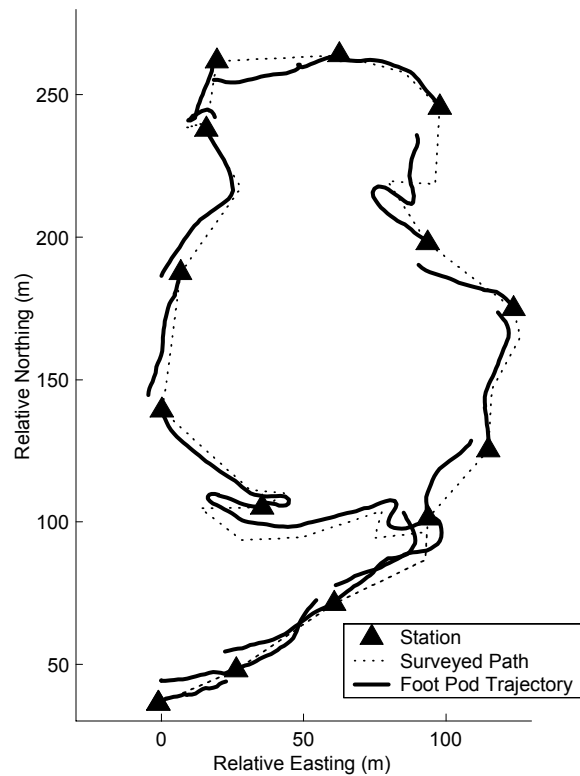


Figure 7.13: Short term performance of the foot pod

Two cases are discussed in the following sections that demonstrate some of the performance differences between satellite positioning and pedestrian navigation systems in terms of resolution of motion.

### 7.4.1 Moving Turn

On the test section between Control Points 8 and 9, the user walked an arm's length circle around a tree growing on the path. This circle has an estimated circumference of 8.5 m,

making up much of the 10 m difference between the foot pod distance estimation and the straight surveyed distance between the two points.

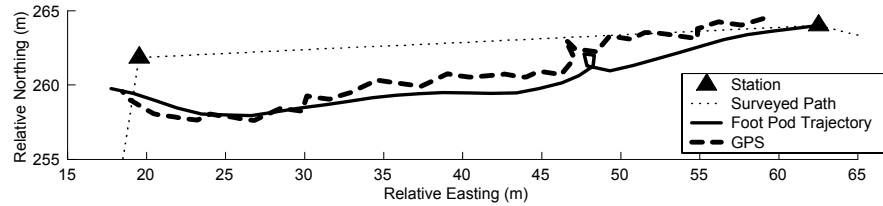


Figure 7.14: Comparison of GPS and foot pod trajectories during short radius turn

The diameter of the circle walked around the tree is smaller than resolution of the high sensitivity GPS, which shows this period as a pause in motion instead.

#### 7.4.2 Stationary Turn

As shown in Figure 7.15, the highest discrepancy in estimated distance between the GPS and the foot pod was arriving at control point 10, after staying stationary for about 30 seconds in the shelter shown in Figure 7.2. The GPS solution, which is calculated every second, diverges over 10 m because of increased signal attenuation inside the shelter, but the foot pod solution does not because no strides are detected while the user is stationary.

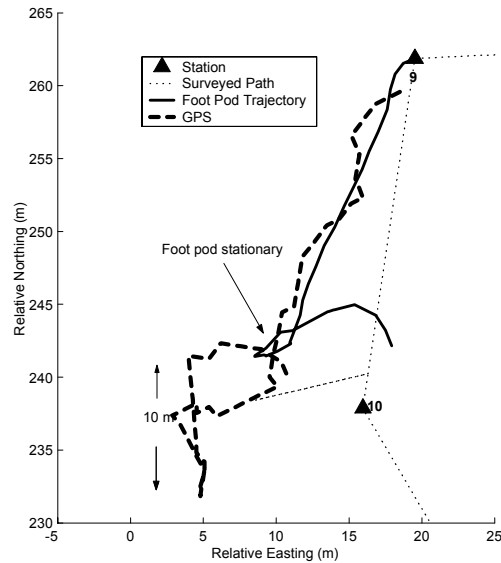


Figure 7.15: Comparison of GPS and foot pod trajectories during stationary period

These two cases highlight situations where the macroscopic accuracy of high sensitivity GPS could benefit from integration with a pedestrian dead reckoning system to improve resolution.

## 7.5 Summary of Field Trials

The treadmill tests and existing research by others had established the validity of measuring stride length with shoe mounted accelerometers. Measuring heading with shoe mounted sensors is entirely novel, and these field trials established that it is possible. Though calibration challenges hampered the overall accuracy, the shoe mounted pedestrian dead reckoning system is capable of measuring stride length and heading.

By adjusting the bias levels the accuracy of the acceleration measurements were improved and the overall position error was reduced by half. It is expected that the error could be reduced further with more accurate bias values.

Examination of the short term performance of the system, and special components of the test course showed that the foot pod system is capable of measuring details motion with finer resolution than the high sensitivity GPS.

## Chapter 8

# Conclusion and Recommendations

A novel method of pedestrian dead reckoning using shoe mounted sensors was proposed and investigated. In this preliminary study, an algorithm was developed to propagate a position by detecting stride events, measuring their length and estimating their heading with low cost accelerometers and magneto-resistive sensors. Through treadmill tests and field trials, it was found that it is possible to navigate using shoe mounted sensors though the overall accuracy does not compare well at this point with conventional methods of pedestrian navigation and satellite positioning.

A means of detecting strides was developed that could identify events of the gait cycle using accelerometer signals. Being sensitive to the motion of the foot, accelerometers allow events to be detected during the swing phase while the foot is not touching the ground. Finding stance phase is particularly important, because this is the period of time when the foot is stationary and accelerometers can be used to measure the orientation of the foot.

To validate and establish the performance of the accelerometer based stride length measurement method, treadmill tests were performed. Through these tests it was found that it is possible to measure the angle of the sensor board during stance phase, and integrate angular acceleration during swing phase to determine the sensor angle through the entire stride. Knowing the foot angle allows the horizontal and vertical components of acceleration to be resolved from the accelerometer signal. The average horizontal velocity of the foot was determined through integration and multiplied by the stride duration to generate a stride length measurement. Tests at varying speeds found that the stride length measurement was accurate to approximately 3% of the distance travelled.

The performance of the complete pedestrian dead reckoning system was evaluated

through field trials conducted in a forested environment, away from magnetic disturbances. In the field trials it was found that the novel method of heading measurement from foot mounted sensors is valid, but not terribly accurate.

## 8.1 Improving performance

Because the goal of this research was to establish the basic feasibility of shoe based pedestrian navigation, low cost sensors were applied and the system was operated strictly in dead reckoning mode. Though the accuracy observed in the field trials was substantially inferior to the references, the references used are relatively sophisticated and relatively expensive positioning systems. Having shown that it is possible to measure position with shoe mounted sensors, the system may be improved by a combination of improving measurement accuracy and increasing system sophistication.

Better measurement accuracy can be achieved without using more expensive sensors simply by improving the signal conditioning and system monitoring of the existing sensors. Adding a temperature sensor, and establishing the thermal behavior of the individual sensors will reduce measurement uncertainty in outdoor applications. Amplifying the accelerometer output and using a monopolar data acquisition system will significantly improve the measurement resolution, which in turn will improve the angular resolution of the orientation determination. Alternatively, higher accuracy can be achieved by applying higher quality, higher cost sensors.

The majority of pedestrian navigation systems are integrated to some degree with GPS, as the combination of microscopic detail from the sensors and macroscopic accuracy of the satellite system make a good match. Torso mounted systems are appropriate for GPS integration as the entire system can be contained in one enclosure. Signal masking by the leg, and the increased weight make it seem unlikely that GPS would be added directly to the foot pod but this system could otherwise be integrated.

## 8.2 Recommendations for Further Investigation

Even with improved accuracy, the pedestrian navigation system proposed is limited in its application. To make the system truly useful, it must robustly measure the widest possible range of common pedestrian motions, such as walking up stairs or diagonally. Some ideas that merit further investigation are now presented.

1. The accelerometers are used in every aspect of the algorithm from establishing orientation to measuring stride length, but the compasses are currently used strictly in the heading determination. It was noted when discussing the compass signal of Figure 5.10 that the signal measured in stance phase must be used because during swing phase, motion of the foot dominates the signal. As magneto-resistive sensors measure angle directly, it may be possible to use the signal during swing phase to improve dynamic foot angle measurement.
2. To simplify the scope of this research, one of the base assumptions made was that the user's foot has a consistent orientation with respect to the user's direction of motion. This makes no allowance for lateral, diagonal or backward movement. As discussed in the introduction, Ladetto [8] used relatively simple signal modelling to determine walking patterns from a torso mounted accelerometer. Adding the capability to detect and measure non-forward walking would improve the accuracy and robustness of the shoe based sensor system. Without adding any sensors to the system, it should be possible to measure backwards motion directly using a similar algorithm to the stride length measurement described in Chapter 4. The gait cycle for this type of motion will be different, requiring a separate event detection scheme. Additional sensors may be required to measure motion out of the sagittal plane.
3. Again to simplify the scope of this project, the motion was assumed to be entirely horizontal. It was shown through the treadmill tests that the accelerometer resolution was not sufficient to measure vertical travel of the foot. With improved system resolution vertical position measurement may be possible. No study has been done to establish whether it is possible to measure vertical motion on inclines or stairs through accelerometry. Collin [23] has shown that miniature atmospheric pressure sensors can be used to measure vertical position with sufficient resolution to determine what floor the user is on.
4. A shoe based pedestrian dead reckoning system will be most useful in places where GPS signals are attenuated or unavailable. As the GPS trajectories in the field trial show, high sensitivity GPS receivers make accurate positioning possible in the forest, making urban canyons and indoor environments the more appropriate application area for pedestrian navigation. To operate in an urban environment, a means of detecting and compensating for magnetic field disturbances is necessary. This may require rate gyros or applying similar offset accelerometry techniques to the

transverse plane.

# Bibliography

- [1] MacGougan, G., Lachapelle, G., et al, "Performance Analysis of A Stand-Alone High Sensitivity Receiver." *GPS Solutions*, Springer Verlag, V.6, No.3, pp. 179-195. (2002)
- [2] Lachapelle, G., Kuusniemi, H., Dao, D., MacGougan, G., and M.E. Cannon, "HSGPS Signal Analysis and Performance Under Various Indoor Conditions" *Proceedings of GPS 2003*, The Institute of Navigation (2003)
- [3] Rose, J., Gamble, J.G., *Human Walking*, Williams & Wilkins (1993)
- [4] Aminian, K., Najafi, B., Büla, C., Leyvraz P., and P. Robert, "Spatio-temporal Parameters of Gait Measured by an Ambulatory System Using Miniature Gyroscopes" *Journal of Biomechanics* V.35, pp. 689-699, Pergamon Press (2002)
- [5] Veltink, P., Nieuwland, D. ,J. Harlaar, and C. Baten, "Inertial Sensing in a Hand Held Dynamometer", *Proceedings of the IEEE Engineering in Medicine and Biology Society*, Amsterdam, October 31 - November 3 (1996)
- [6] Hansen, A., Childress, D., and M. Meier, "A simple method for Determination of Gait Events" *Journal of Biomechanics* V.35 pp. 135-138, Pergamon Press (2002)
- [7] Käppi, J., Collin, J., Saarinen, J., and J. Syrjärinne, "MEMS-IMU Based Pedestrian Navigator for Handheld Devices," *Proceedings of GPS 2001*, The Institute of Navigation (2001)
- [8] Ladetto, Q. "Capteurs et Algorithmes pour la Localisation Autonome en Mode Pédestre", Phd Thesis, École Polytechnique Fédérale de Lausanne (2003)
- [9] Veltink, P., Franken, H., Verboon, A. and H. Boom "Detection of Knee Instability Using Accelerometers - Experimental and Potential Use in the Control of FES-Assisted

- Paraplegic Standing" *Proceedings of the IEEE Engineering in Medicine and Biology Society*, Oct 28-31, (1993)
- [10] Morris, JRW "Accelerometry - A technique for the measurement of human body movements" *Journal of Biomechanics* V.6 pp.729-736, Pergamon Press (1973)
- [11] Willemsen, A. Th., Van Alsté, M., and H.B.K Boom "Real-Time Gait Assessment Utilizing a New Way of Accelerometry" *Journal of Biomechanics*, V.23, pp 859-863, Pergamon Press (1990)
- [12] Willemsen, A Th., Frigo,M., and HBK Boom "Lower Extremity Angle Measurement with Accelerometers - Error and Sensitivity Analysis" *IEEE Transactions on Biomedical Engineering* V. 38, No. 12, December (1991)
- [13] Mayagoitia, R., Neneb, A., and P. Veltink, "Accelerometer and Rate Gyroscope Measurement of Kinematics: an Inexpensive Alternative to Optical Motion Analysis Systems" *Journal of Biomechanics* V.35 pp. 537-542, Pergamon Press (2002)
- [14] Baten,C.T.M., Luinge, H.J., Veltink, P.H. and H.J. Hermens, "Applying Inertial Sensing in Human Movement Analysis", *Proceedings of the International Bio-mechatronics Workshop*, 19-21 April (1999)
- [15] Miyazaki, S., "Long-Term Unrestrained Measurement of Stride Length and Walking Velocity Utilizing a Piezoelectric Gyroscope" *IEEE Transactions on Biomedical Engineering* V 44, No.8 pp753-759 (1997)
- [16] Fyfe, K. "Motion Analysis System", U.S. Patent, September (1999)
- [17] Sagawa, K., Hikaru, I., and S. Yutaka, "Non Restricted Measurement of Walking Distance" *Proceedings of the IEEE International Conference on Systems, Man and Cybernetics*. V.3 p 1847-1852, (2000)
- [18] Levi, R.W., and T. Judd, "Dead Reckoning Navigation System Using Accelerometer to Measure Foot Impacts" US Patent, December, (1999)
- [19] Ladetto, Q. "On Foot Navigation: Continuous Step Calibration Using Both Complementary Recursive Prediction and Adaptive Kalman Filtering" *Proceedings of GPS 2000*, The Institute Of Navigation (2000)
- [20] Ladetto, Q., Gabaglio V., Merminod B.,Terrier, P., and Y., Schutz, "Human Walking Analysis Assisted by DGPS" GNSS (2000)

- 
- [21] Ladetto, Q., Merminod B., "Digital Magnetic Compass and Gyroscope Integration for Pedestrian Navigation" 9th International Conference on Integrated Navigation Systems, St-Petersburg, 27-29 May 9 (2002)
- [22] Collin, J., Käppi, J. "Navigating the City" *Galileo's World*, Spring (2002)
- [23] Collin, J., Mezentsev, O., Lachapelle, G. "Indoor Positioning System Using Accelerometry and High Accuracy Heading Sensors" *Proceedings of GPS/GNSS 2003* The Institute of Navigation (2003)
- [24] Analog Devices Inc. "ADXL210E Low-Cost Dual Axis Accelerometer With Duty Cycle", Datasheet (2002)
- [25] Honeywell Inc. "1 and 2 Axis Magnetic Sensors", Data Sheet (2000)
- [26] National Instruments (2000) "DAQ 6023E/6024E/6025E User Manual"
- [27] NovaTel Inc "OEM G4" Brochure.
- [28] SiRF Technology "SiRFstarIIe Evaluation Kit" Brochure 2002
- [29] Lachapelle, G., Mezentsev, O., Collin J., and G. MacGougan "Pedestrian and Vehicular Navigation Under Signal Masking Using Integrated HSGPS and Self Contained Sensor Technologies" CD-ROM Proceedings of 11th World Congress, International Association of Institutes of Navigation (Berlin, 21-24 October).(2003)
- [30] Lynn P., Fuerst, W. *Digital Signal Processing with Computer Applications* 2nd Ed. John Wiley and Sons, 1998
- [31] Anton, Howard *Elementary Linear Algebra 7th Ed*, Wiley, (1994)
- [32] Kuipers, Jack *Quaternions and Rotation Sequences*, Princeton University Press, (1999)
- [33] Holman, J.P., *Experimental Methods For Engineers*, McGraw-Hill, 1966
- [34] Campbell, Wallace H. *Introduction to Geomagnetic Fields*, Cambridge University Press 1997
- [35] National Oceanic and Atmosphere Administration - National Geophysical Data Center: <http://www.ngdc.noaa.gov>
- [36] Geological Survey of Canada: [www.geolab.nrcan.gc.ca/geomag](http://www.geolab.nrcan.gc.ca/geomag)

# Appendix A

## Sensitivity Analysis

Considering the specifications listed in Tables 3.1-3.4 of Chapter 2, we can estimate the effective sensitivity for each sensor.

We begin by considering the sensitivity of the 12 bit data acquisition system. The input is bipolar, with a range of  $-5\text{ V}$  to  $5\text{ V}$  so the smallest detectable change in input is.

$$S_{DAQ} = \frac{10\text{ V}}{2^{12} - 1} = 2.44\text{ mV}$$

Note that since all of the sensor signals range from 0 to 5 V only %50 of the input range is used, making this effectively an 11 bit system.

### A.1 Accelerometer Sensitivity and Noise Density

Using the nominal analog sensitivity and sensor range, we can determine the smallest detectable change in acceleration.

Part No	Range	Sensitivity	0 g Voltage	Signal Range	% Input Range
ADXL210	$\pm 10\text{ g}$	$100\text{ mV/g}$	$2.5\text{ V}$	$1.5\text{ V} - 3.5\text{ V}$	20

The accelerometer signal will use just 20% of the input range of the data acquisition system. The system sensitivity in units of acceleration is:

$$\text{ADXL210: } \frac{2.44\text{ mV}}{100\text{ mV/g}} = 24.4\text{ mg}$$

The specified noise density of the ADXL series accelerometers is specified as [24]

$$\text{Noise}(rms) = \left( 500 \frac{\mu\text{g}}{\sqrt{\text{Hz}}} \right) \sqrt{BW \cdot 1.5}$$

Where  $BW$  is the  $3dB$  band width in Hz, set by the capacitor on the analog output ports. Experience shows that the frequencies of interest are below 10 Hz, so the bandwidth of

the new system will be set to 50 Hz with a capacitor. The expected RMS noise density [24] is

$$Noise(rms) = \left(500 \frac{\mu g}{\sqrt{Hz}}\right) \sqrt{50 \text{ Hz} \cdot 1.5} = 4.3 \text{ mg}$$

The peak to peak noise value is expected to remain within 4 times the rms noise rating of 95% of the time. For the ADXL210 this is 17.3 mg, less than the system sensitivity.

## A.2 Sensor and Algorithm Resolutions

In Chapter 3, the sensors and data acquisition equipment used for this investigation are described in detail. Here we examine how the system sensitivity affects the resolution of the stride length measurement.

**Static Angle Uncertainty and Resolution** In Equation 4.8, we showed how stationary accelerometer output may be used to directly calculate inclination angle:

$$\theta = \arctan\left(\frac{a_y}{a_x}\right)$$

The resulting angular uncertainty  $\varepsilon_\theta$ , due to the uncertainty in each accelerometer axis  $\varepsilon_a$  is [33]:

$$\begin{aligned} \varepsilon_\theta &= \sqrt{\left(\frac{\partial\theta}{\partial a_x}\varepsilon_a\right)^2 + \left(\frac{\partial\theta}{\partial a_y}\varepsilon_a\right)^2} \\ \varepsilon_\theta &= \sqrt{\varepsilon_a^2 \frac{a_x^2}{(a_x^2 + a_y^2)^2} + \varepsilon_a^2 \frac{a_y^2}{(a_x^2 + a_y^2)^2}} \\ &= \varepsilon_a \sqrt{\frac{1}{a_x^2 + a_y^2}} \end{aligned}$$

Since we know that  $a_x = \cos\theta$  and  $a_y = \sin\theta$ , we have

$$(a_x^2 + a_y^2) = \cos^2\theta + \sin^2\theta = 1$$

So

$$\varepsilon_\theta = \varepsilon_a$$

With a system resolution 24.4 mg, the ADXL210 used on the footpod will have a maximum uncertainty due to resolution of

$$\varepsilon_\theta = \varepsilon_a = 0.024 \text{ rad} = 1.4^\circ \tag{A.1}$$

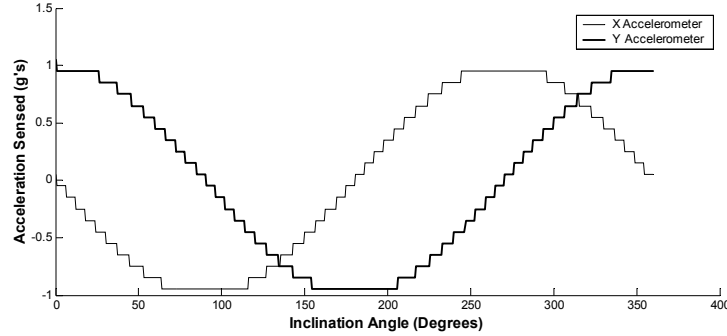


Figure A.1: Quantization of accelerometer signal

Quantization error of the accelerometer signals by analog to digital conversion leads to a fluctuating error in angle calculated in Eq (4.8). because the signal is resolved into discrete values. A second method of predicting the uncertainty in  $\theta$  is to model the quantization error by modelling the output from the biaxial accelerometers as they are rotated completely in the vertical plane. Figure A.1 shows the sinusoidal signals from the accelerometers, truncated into 24.4mg increments. Plotted in Figure 5.10, the resulting error in calculated angle has a maximum magnitude of  $1.5^\circ$ , which agrees in magnitude to the expected uncertainty calculated in Eq. (A.1).

### A.2.1 Angular Acceleration Resolution

Next we calculate the smallest detectable change in angular acceleration. From Eq (4.11) we have

$$\alpha = \frac{a_1 - a_2}{r} \quad (\text{A.2})$$

The expected uncertainty

$$\begin{aligned} \varepsilon_\alpha &= \sqrt{\left(\frac{\partial\alpha}{\partial a_1} w_a\right)^2 + \left(\frac{\partial\alpha}{\partial a_2} w_a\right)^2 + \left(\frac{\partial\alpha}{\partial r} w_r\right)^2} \\ \varepsilon_\alpha &= \sqrt{\frac{2}{r^2} \varepsilon_a^2 + \frac{1}{r^4} \varepsilon_r^2 (a_2 - a_1)^2} \end{aligned}$$

This tells us that the error in the angular acceleration that we calculate is based on the uncertainty due to the accelerometer resolution, and the uncertainty in the separation of

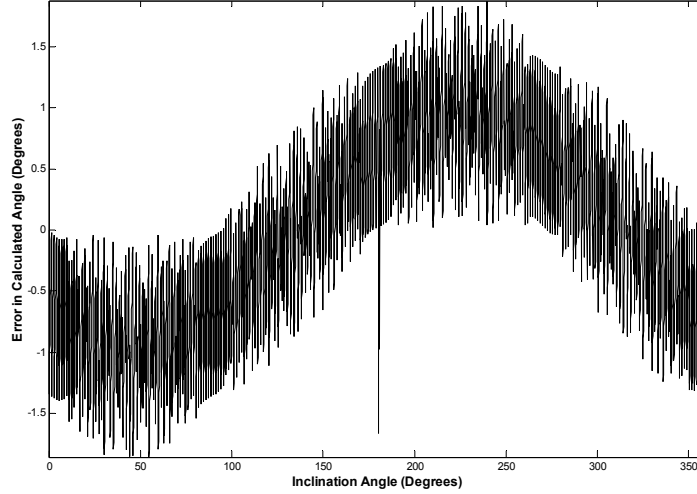


Figure A.2: Error in static angle due to quantization

the accelerometers.

$$\begin{aligned}
 r &= 41 \text{ mm} \\
 \varepsilon_a &= 0.024 \left( 9.81 \frac{\text{m}}{\text{s}^2} \right) = 0.235 \frac{\text{m}}{\text{s}^2} \\
 \varepsilon_a &= 0.008 \left( 9.81 \frac{\text{m}}{\text{s}^2} \right) \\
 \varepsilon_r &= 0.5 \text{ mm}
 \end{aligned}$$

A large value for  $(a_2 - a_1)$  would be 1 g, though the precision in accelerometer placement means this component has a relatively small contribution to the overall uncertainty.

$$\begin{aligned}
 \varepsilon_\alpha &= \sqrt{\frac{2}{(41 \text{ mm})^2} \left( 0.235 \frac{\text{m}}{\text{s}^2} \right)^2 + \frac{(0.5 \text{ mm})^2}{(41 \text{ mm})^4} \left( 10 \frac{\text{m}}{\text{s}^2} \right)^2} \\
 &= 8.6 \frac{\text{rad}}{\text{s}^2}
 \end{aligned}$$

Ignoring the second term completely affects the uncertainty in angular acceleration by about  $0.5 \frac{\text{rad}}{\text{s}^2}$ , or five percent, indicating that the majority of the uncertainty in the angular acceleration measurement comes from the accelerometer resolution.

### A.2.2 Integrated Angular Velocity and Angular Resolution

Numerical integration is performed using Euler's method. The current integrated angular velocity  $\omega(t)$  is calculated by summing the previous integrated value  $\omega(t-1)$  with the

product of the previous angular acceleration  $\alpha(t-1)$  and the time interval  $\Delta t$

$$\omega(t) = \omega(t-1) + \alpha(t-1) \Delta t$$

The error in this process comes from both error in the current calculation, and the accumulation of all the previous calculation errors.

The error in a single calculation  $\tilde{\omega}$  is examined first

$$\tilde{\omega} = \alpha(t-1) \Delta t$$

$$\begin{aligned} \varepsilon_{\tilde{\omega}} &= \sqrt{\left(\frac{\partial \omega}{\partial \Delta t} \varepsilon_{\Delta t}\right)^2 + \left(\frac{\partial \omega}{\partial \alpha} \varepsilon_{\alpha}\right)^2} \\ &= \sqrt{(\alpha(t-1) \varepsilon_{\Delta t})^2 + (\Delta t \varepsilon_{\alpha})^2} \end{aligned}$$

The clock error  $\varepsilon_{\Delta t}$  on the National Instruments data acquisition card is  $5 \mu\text{s}$ , making the first error term insignificant. The error in one integration step is then

$$\begin{aligned} \varepsilon_{\tilde{\omega}} &= \Delta t \varepsilon_{\alpha} \\ &= 0.005 \text{ s} \left(8.6 \frac{\text{rad}}{\text{s}^2}\right) = 0.043 \frac{\text{rad}}{\text{s}} \end{aligned}$$

But this error will accumulate over the integrated stride. A long stride would last 1.5 s, or 300 samples.

$$\begin{aligned} \varepsilon_{\omega} &= \sqrt{N (\varepsilon_{\tilde{\omega}})^2} = \sqrt{N} \varepsilon_{\tilde{\omega}} \\ &= \sqrt{300} \left(0.043 \frac{\text{rad}}{\text{s}}\right) \\ &= 0.74 \frac{\text{rad}}{\text{s}} \end{aligned}$$

Angular position is calculated the same way

$$\theta(t) = \theta(t-1) + \omega(t-1) \Delta t$$

So the error in a single calculation will be

$$\begin{aligned} \varepsilon_{\tilde{\theta}} &= \Delta t \varepsilon_{\omega} \\ &= 0.005 \text{ s} \left(0.74 \frac{\text{rad}}{\text{s}}\right) \\ &= 0.0037 \text{ rad} \end{aligned}$$

The angular error accumulated over the integrated stride will be:

$$\begin{aligned}
 \varepsilon_{\theta} &= \sqrt{N} \varepsilon_{\tilde{\theta}} \\
 &= \sqrt{300} (0.0037 \text{ rad}) \\
 &= 0.064 \text{ rad} \\
 \varepsilon_{\theta} &= 3.6^{\circ}
 \end{aligned}$$

### A.2.3 Integrated Linear Velocity and Position Resolution

The horizontal component of acceleration is resolved from the measurements and the integrated foot angle profile.

$$a_Y = a_t \cos \theta + a_r \sin \theta$$

The error in the horizontal component of acceleration is then

$$\begin{aligned}
 \varepsilon_{a_Y} &= \sqrt{\left(\frac{\partial a_Y}{\partial a_t} \varepsilon_{a_t}\right)^2 + \left(\frac{\partial a_Y}{\partial a_r} \varepsilon_{a_r}\right)^2 + \left(\frac{\partial a_Y}{\partial \theta} \varepsilon_{\theta}\right)^2} \\
 &= \sqrt{(\cos \theta \varepsilon_{a_t})^2 + (\sin \theta \varepsilon_{a_r})^2 + ((a_t \cos \theta - a_r \sin \theta) \varepsilon_{\theta})^2}
 \end{aligned}$$

Again, we assume that the error in acceleration measurement is the same for both axes

$$\varepsilon_{a_Y} = \sqrt{\varepsilon_a^2 + (a_t \cos \theta - a_r \sin \theta)^2 \varepsilon_{\theta}^2}$$

This error function is plotted below in Figure A.3, for a single stride at 1.1 m/s

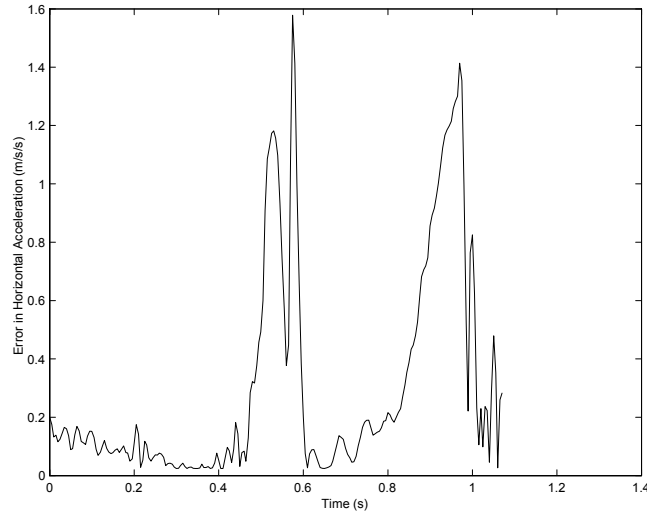


Figure A.3: Error in Horizontal Acceleration

In this specific case the mean value of the estimated error in horizontal acceleration is  $0.30 \pm 0.38 \text{ m/s}^2$ . We will use the maximum value of  $1.5 \text{ m/s}^2$  as an error estimate.

The accumulated integration error will be:

$$\begin{aligned}\varepsilon_v &= \sqrt{300} (0.005 \text{ s}) (1.5 \text{ m/s}^2) \\ &= 0.13 \text{ m/s}\end{aligned}$$

$$\begin{aligned}\varepsilon_v &= \sqrt{300} (0.005 \text{ s}) (0.13 \text{ m/s}) \\ &= 0.02 \text{ m}\end{aligned}$$

That is, under ideal conditions we expect an error of 2 cm per stride.

## Appendix B

# Accelerometer Calibration

The Analog Devices ADXL series accelerometers represent acceleration as a voltage. To account for manufacturing tolerances, supply voltage and temperature drift, and final orientation the accelerometers are calibrated after the sensor board is assembled, prior to use. Gravitational acceleration is used to determine the sensitivity and bias of each accelerometer axis.

### B.1 Block Calibration

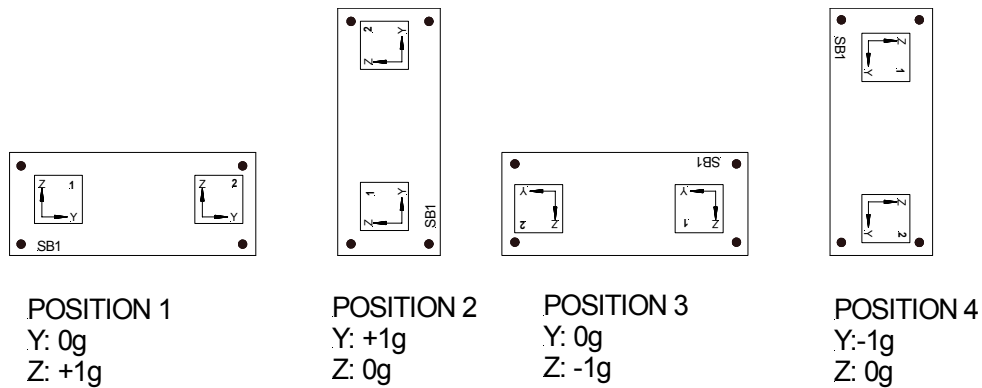


Figure B.1: Block Calibration Positions

A simple and consistent method of accelerometer calibration uses the acceleration of gravity. In this method, the sensor board, mounted to a block, is placed in four static positions as illustrated in Figure B.1. The faces of the calibration block are machined with a fine perpendicularity tolerance, and the surface it rests on is carefully levelled with a spirit level. Each accelerometer will be placed in a position where it measures  $+1g$  and  $-1g$ , as well as two positions with  $0g$ .

*Sensitivity* is the change in output for a change in input. For the axes labelled  $Y$  in the figure, the sensitivity is calculated as.

$$S_Y = \frac{V_1 - V_3}{+1g - (-1g)} = \frac{\Delta V_{1-3}}{2} V/g \tag{B.1}$$

The bias, or zero  $g$  output of the accelerometer can be evaluated by in either of two ways. First, since the two vertical positions represent symmetric inputs about the bias level, the bias must be the mean value.

$$B_Y = \frac{V_1 + V_3}{2} V \tag{B.2}$$

We have also recorded two positions where the accelerometers should read  $0g$ , so the bias level can be calculated from these readings instead

$$B_Y = \frac{V_2 + V_4}{2} V \tag{B.3}$$

**B.1.1 Error sources**

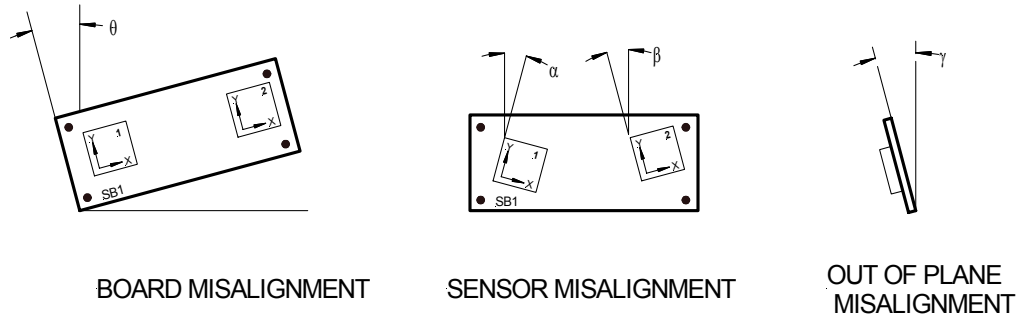


Figure B.2: Accelerometer Misalignment

The block calibration assumes that in each position, the axes are pointing perfectly aligned with the vertical and horizontal axes. This is impossible to achieve, so we must understand how misalignments like the ones shown (exaggerated) in Figure B.2 affect the accuracy of the calibration procedure.

In the case of board misalignment, our concern is that the calibration procedure will not yield accurate values. This can occur when the sensor board is not aligned with the calibration block, or when the surface the block rests on is not level.

For an accelerometer pointed nearly vertical, the acceleration measured  $a$ , is proportional to the cosine of the misalignment angle  $\theta$ .

$$a = g \cos \theta$$

Which means that for non zero values of  $\theta$ , the accelerometer experiences an acceleration less than  $g$ . Experience with the small angle approximation leads us to anticipate that misalignment will not seriously disturb the calibration since  $\cos \theta \approx 1$  if  $\theta$  is sufficiently small. This expectation is reinforced by the deadband region observed in Figure A.1, where the accelerometer is observed to be insensitive to small angular change near vertical. It is simply a matter of deciding how accurate a calibration is desired. If  $0.001g$  is a permissible deviation, the allowable angular misalignment can be calculated

$$\begin{aligned} 0.999g &= g \cos \theta \\ \theta &= \pm 2.6^\circ \end{aligned}$$

This means that as long as the total misalignment accumulated by board, sensor and out of plane misalignment is less than  $\pm 2.5^\circ$ , the sensor will be subject to at least  $0.999g$ , which seems sufficiently accurate. With a modicum of care in the setup of the calibration, it should be easy to achieve an accurate value for the sensitivity.

When the accelerometer is supposed to be aligned horizontally, as in the case of the Bias calibration, the acceleration is proportional to the sine of inclination angle. Instead of zero  $g$  we have

$$a = g \sin \theta$$

Again, if we allow up to  $0.001g$  deviation from the desired acceleration, we find the required angular tolerance is much less forgiving.

$$\begin{aligned} 0.001g &= g \sin \theta \\ \theta &= \pm 0.06^\circ \end{aligned}$$

Meeting the horizontal angular tolerance will be substantially more difficult than the vertical one, suggesting that Equation B.3 will be the more accurate method of determining the bias.

As stated in [24], the chassis misalignment of the accelerometers within the sensor packaging is  $\pm 1^\circ$ , which is approximately the angular resolution of the data acquisition system. This means that it is unlikely that the sensor misalignment can be detected through calibration.

## Appendix C

# Geomagnetic Fields

### C.1 Introduction

Studying the behaviour of a compass needle in 1600, William Gilbert wrote that the Earth behaves as one giant magnet. Geomagnetic research in the intervening time has shown that the field measured at the Earth's surface field results from a combination of several magnetic fields. The largest component, called the Main Field, does generally resemble the field generated by a dipole magnet, with poles deep in the earth and offset from the geographic poles by about 11 degrees. The Main Field is a slowly changing field generated by the flow of molten metal in the earth's outer core. Other fields that superimpose over the Main Field are the fields arising from electrical currents flowing within the earth's crust and in the ionosphere. These fields may have magnitudes up to 10% of the main field, but are more difficult to predict.

The Main Field component is modeled by the International Geomagnetic Reference Field (IGRF) and World Magnetic Model (WMM) from data collected at hundreds of monitoring stations around the world. The Earth's magnetic field varies both in space and time, so these models must account for both position and date to predict the magnetic field. The field changes in slow, predictable manner over the long term, so the models are periodically updated.

### C.2 Magnetic Field Parameters

The magnetic field at any point on the Earth is a vector quantity with a magnitude and a direction. The vector representing the Earth's field is commonly described in two ways. One way is to use three orthogonal component field directions with positive values for geographic Northward ( $X$ ), Eastward ( $Y$ ), and vertical into the earth ( $Z$ ) as shown in Figure C.1. The second method is to state the horizontal magnitude ( $H$ ), the eastward declination angle ( $D$ ) from geographic northward and the downward vertical component ( $Z$ ).

These parameters are related by simple geometry

$$\begin{aligned} H &= \sqrt{X^2 + Y^2} \\ X &= H \cos(D) \\ Y &= H \sin(D) \end{aligned}$$

The inclination ( $I$ ), sometimes called dip, is the angle that the total field makes with the horizontal plane.

$$\frac{Z}{H} = \tan I$$

The total field intensity  $F$ , can be constructed using either method

$$F = \sqrt{X^2 + Y^2 + Z^2} = \sqrt{H^2 + Z^2}$$

The magnitude of  $F$  will range between 25,000-65,000 nT (0.25-0.65 Gauss).

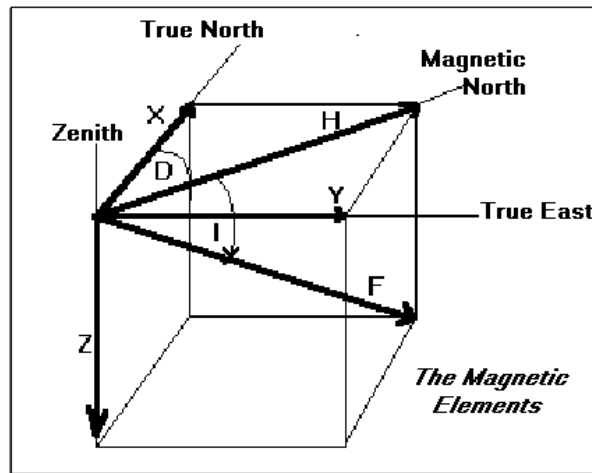


Figure C.1: Magnetic field elements, adapted from [35]

Note that the sign convention for the magnetic parameters is slightly different than we use in our definition of the global frame. In the global reference frame  $\mathcal{G}$ , the magnetic field vector  $\vec{H}$  will have the components  $[Y, X, -Z]$

### C.3 Magnetic Field References

There are a number of resources available to predict the magnetic field vector for a particular place and time. Coarse maps are available that can be quickly reference to get

approximate values for the declination, horizontal and vertical intensity. Figure C.2 below shows an example map of declination.

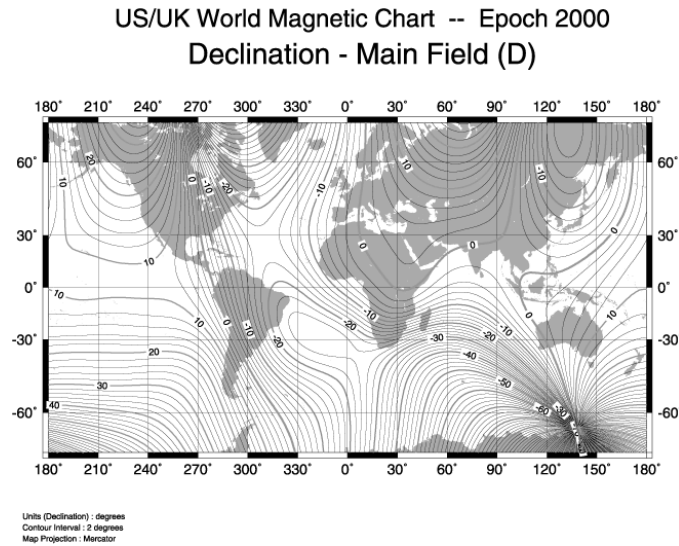


Figure C.2: World map of Earth's main field - declination, adapted from [35]

For more accurate values, software and online utilities are available that calculate all seven magnetic field parameters for a given latitude, longitude, altitude and time. In general, these models such as the IGRF and WMM (WMM) are accurate to within 30 minutes of arc for D and I and about 200 nanoTesla for the intensity elements, though local anomalies do occur. The most accurate field measurements, are from a geomagnetic observation station, if there is one in close proximity. The Geologic Survey of Canada has a number of observation stations. Magnetic field observations for Victoria B.C. are shown in Figure C.3.

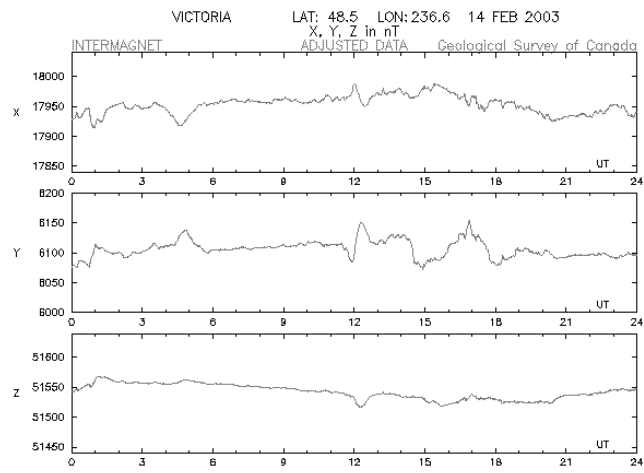


Figure C.3: Magnetic field observations at Victoria, B.C. February 14, 2003 [36]